Advancements in automated design methods for NICFD turbomachinery

Vitale, Salvo

Important note
To cite this publication, please use the final published version (if applicable).
Please check the document version above.

Advancements in automated design methods for NICFD turbomachinery

Proefschrift

ter verkrijging van de graad van doctor
aan de Technische Universiteit Delft,
op gezag van de Rector Magnificus Prof.dr.ir. T.H.J.J. van der Hagen
voorzitter van het College voor Promoties,
in het openbaar te verdedigen op
vrijdag 30 november 2018 om 10:00 uur

door

Salvatore VITALE
Master of Science in Energy Engineering, Politecnico di Milano
geboren te Patti, Italië

Dit proefschrift is goedgekeurd door de promotoren.

Samenstelling promotiecommissie bestaat uit:

Rector Magnificus	voorzitter
Prof.dr.ir. P. Colonna	Technische Universiteit Delft, promotor
Dr.ir. M. Pini	Technische Universiteit Delft, copromotor

Onafhankelijke leden:

Prof. dr. K. Vuik	Technische Universiteit Delft
Prof. dr. J.J. Alonso	Stanford University, Verenigde Staten
Prof. dr. N. R. Gauger	Technical University of Kaiserslautern, Duitsland
Dr. T. Verstraete	Von Karman Institute, België
Dr. G. Robert	Siemens Power and Gas, Duitsland

Cover designed by Matija Balen

---

[1]Author e-mail address: `salvatore.vitale@me.com`

Table of Contents

Samenvatting

De overgang naar betaalbaardere, betrouwbaardere en duurzamere paradigma voor energievoorziening is een van de voornaamste uitdagingen die de mensheid moet overwinnen om de planeet te beschermen tegen de schadelijke effecten die worden veroorzaakt door klimaatverandering. The CO_2-concentratie in de atmosfeer is dramatisch toegenomen sinds de periode van voor de industrialisatie. Als de toename in de uitstoot van broeikasgassen ongehinderd doorzet, zal dit dramatische consequenties met zich meebrengen voor de Aarde, het bestaan van vele soorten in gevaar brengend, inclusief het menselijk ras.

Om een catastrofe door klimaatverandering te vermijden, moet het aandeel van primaire energie uit duurzame energiebronnen toenemen van rond de 15% in 2015 naar 65% in 2050. Deze energietransitie kan niet alleen gestoeld zijn op een paar succesvolle technologien (i.e. zonnepanelen en windenergie), maar zal moeten rekenen op een grotere variteit aan technische oplossingen die geschikt zijn voor een breder spectrum van duurzame energiebronnen en diversiteit van omstandigheden. Bijvoorbeeld, duurzame thermische energiebronnen voor stroomopwekking (i.e. geothermisch reservoir, biomassabrandstof en geconcentreerde zonnestraling), kunnen voor een groot deel in de wereldwijde elektriciteitsvraag voorzien in de toekomst. Echter, de exploitatie van een significant deel van deze bronnen is sterk afhankelijk van het commercile succes van technologien zoals het organische rankinecyclus (ORC) energiesysteem.

Een van de sleutelfacetten om ORC-systemen economisch concurrerend te maken, met name voor kleinere formaten ($\approx 1 - 50$ kW), is het verwezenlijken van zeer efficinte componenten voor turbomachines. Het vloeistof-dynamisch ontwerp van ORC-turbomachines verschilt aanzienlijk van het ontwerp van traditionele machines (i.e. stoom- en gasturbines) en dit is vooral toe te schrijven aan de verschillende thermo-fysische eigenschappen en gas-dynamisch gedrag van de organische werkvloeistoffen. Dit betekent dat ontwerpmethodes die bedacht zijn voor de standaard stoom- en gasturbines niet gebruikt kunnen worden voor turbomachines die actief zijn in het *Non-ideal compressible fluid dynamics* (NICFD) regime. Bovendien zijn er nooit experimentele onderzoeken gedaan om empirische kennis te vergaren dat het ontwerp van zeer efficiënte ORC turbomachines kan ondersteunen.

Als gevolg hiervan is het volledige ontwerpproces van ORC-turbomachines enkel en alleen afhankelijk van het gebruik van geavanceerde CFD-software. De huidige trend is om CFD-hulpmiddelen met numerieke optimalisatietechnieken te koppelen om zo automatisch de optimale stroomdoorgangsgeometrie te verkrijgen. In het bijzonder methodes gebaseerd op de adjoint hebben duidelijk aangetoond dat zij de enige optimalisatietechniek zijn die in staat is om ontwerpproblemen met meerstaps-turbomachines op te

v

lossen. Derhalve is het onderzoek dat gedocumenteerd is in dit proefschrift gericht op het uitbreiden van de adjoint-methode ten einde een volledig-turbulente vloeistof-dynamische vormoptimalisatie van 3D meerstaps-ORC-turbomachines.

Dit document bevat een uitgebreide introductie, drie hoofdstukken die elk een bouwsteen beschrijven voor de vervulling van het hoofddoel van dit PhD-onderzoek en een laatste afsluitend hoofdstuk waarin alle onderzoeksresultaten van dit werk samengevat worden en toekomstige stappen voor het onderzoeksveld worden voorgesteld. Het eerste deel van dit proefschrift beschrijft de benodigde uitbreiding van de RANS-vergelijkingen, de convectieve numerieke schemas en de visceuze numerieke schemas voor het gebruik van complexe thermo-fysische wetten, om daarmee de turbulente stromingen van componenten die actief zijn in het NICFD-thermodynamische-regime te simuleren. Het tweede deel documenteert de afleiding van de adjoint solver om de vormoptimalisatie-ontwerpproblemen in 2D in een enkele rij van ORC-turbomachines op te lossen. Tenslotte, het laatste deel rapporteert de uitbreiding van de adjoint-methode naar het ontwerp van 3D-meerstaps-turbomachines.

Summary

The transition towards a more affordable, reliable, and sustainable energy provision paradigm is one of the main 21st century challenges that humanity must overcome to protect the planet from the harmful effect caused by climate change. The concentration of CO_2 in the atmosphere has been dramatically increasing since the pre-industrial era. If the increase of green-house gasses emissions continues unabated, this will bring dramatic consequences for planet Earth, compromising eventually the existence of many species, including the human race.

To avoid a climate change catastrophe, the share of primary energy coming from renewable energy resources must increase from around 15% in 2015 to 65% in 2050. This energy transition can not rely solely on few successful technologies (i.e., solar photovoltaic, and wind energy), but it must count on a larger variety of technical solutions that are suitable for a wider range of renewable sources and diversity of circumstances. For instance, renewable thermal energy sources for power generation (i.e., geothermal reservoir, biomass fuel, and concentrated solar radiation), can provide a large portion of the world electricity demand in the future. However, the exploitation of a good portion of these sources strongly depends on the market success of technologies such as the Organic Rankine Cycle (ORC) power system.

One of the key aspects to make ORC systems economically competitive, especially at the smaller sizes ($\approx 1 - 50$ kW), is the realization of highly efficient turbomachinery components. The fluid-dynamic design of ORC turbomachinery significantly differs from the design of traditional machines (i.e., steam and gas turbines), and this is mainly due to the different thermo-physical properties and gas dynamic behavior of the organic working fluids. This means that design methods devised for standard steam and gas turbomachinery can not be used for turbomachinery operating in the Non-ideal compressible fluid dynamics (NICFD) region. Furthermore, no experimental campaigns have ever been carried out to create a body of empirical knowledge to support the design highly efficient ORC turbomachinery.

As a consequence, the entire design process of ORC turbomachinery relies only on the use of advanced CFD software. The current trend is to couple CFD tools with numerical optimization techniques in order to automatically obtain optimal flow passage geometries. In particular, adjoint-based methods have clearly demonstrated to be the only optimization technique capable of tackling the multi-stage turbomachinery design problem, in which thousands of design variable must be concurrently optimized. Therefore, the research documented in this PhD dissertation aimed at extending the adjoint method in order to perform the fully-turbulent fluid-dynamic shape optimization of 3D multi-stage

ORC turbomachinery.

This document contains an extensive introduction, three main chapters, each documenting a building block towards the accomplishment of the main goal of this PhD project, and a final concluding chapter that summarizes all the research outcomes of this work and proposes future steps for research in this field. The first part of the thesis describes the extension of the RANS equations, the convective numerical schemes, and the viscous numerical schemes to the use of complex thermo-physical laws, so to simulate turbulent flows of components working in the NICFD thermodynamic region. The second part documents the derivation of the adjoint solver in order to resolve shape-optimization design problems for 2D single row of ORC turbomachinery. Finally, the last part reports the extension of the adjoint method to 3D multi-stage turbomachinery design.

1
Introduction

The transition towards a more affordable, reliable, and sustainable energy provision paradigm is one of the main 21st century challenges that humanity must overcome to protect the planet from the harmful effect caused by climate change.[1] The fifth assessment report of the Intergovernmental Panel on Climate Change asserts that anthropogenic emission of greenhouse gases (GHG) has a clear impact on global warming.[2] About 70% of these emissions come from the energy sector, whereby carbon dioxide production resulting from the combustion of fossil fuels is preponderant.[3]

The concentration of carbon dioxide (CO_2) in the atmosphere has been dramatically increasing from the value of 280 parts per million (ppm) of the pre-industrial era (mid-1800's) to 403 ppm of 2016.[3] If this increase of CO_2 emissions continues unabated, the average global temperature will rise of about 4°C by 2100 and of 5.5°C in the long term.[4] The temperature increase will bring about dramatic consequences for planet Earth, compromising eventually the existence of many species, including the human race.[2]

In 2009 during the Copenhagen Summit, the governments participating to the 15th Conference of the Parties (COP) agreed to take action in order to reduce GHG emissions so that temperature increase might be kept below 2°C. Since then, the so-called 450[1] scenario, first introduced by the International Energy Agency (IEA) in the World Energy Outlook (WEO) in 2008,[5] has been used by governments and policy makers to set an energy transition pathway which is consistent with a 50% chance of staying within this 2 degree limit.[6]

In the years that followed the Copenhagen Summit, the 450 scenario was subjected to severe criticisms.[7] Although it has been a useful parameter for governments and policy makers to push the reduction of GHG emission worldwide, a single mean value of the global temperature rise does not take into account the differences in local temperature increases and the diversity of repercussions in the various regions of the world. For example, in the African continent the local temperature increase may reach values between $3 - 3.5$°C with an estimation of crop yield reduction of about 50%;[8] the coral reef will barely survive in this scenario;[8] many Caribbean islands and low-laying coastal area will disappear because of the higher sea level.[2]

After long negotiations during the Paris 21st COP in December 2015, for these and many more reasons, governments reached what is today known as the *Paris Agreement*.[9] The Paris Agreement establishes more ambitious goals than the ones of 2009, namely that of *holding the increase in global average temperature to well below 2 °C above preindustrial levels and pursuing efforts to limit the temperature increase to 1.5 °C above preindustrial levels.* In 2017, the IEA formalized this new scenario of the "well below 2 °C" as a 66% probability (instead of the 50% odds of the former 450 Scenario) of maintaining this temperature rise limit throughout the 21st century, without any temporary overshoot. Starting with the WEO-2017,[10] this new scenario will be used as a new energy transition pathway for policy makers and governments in the years to come.

According to this new framework, the share of primary energy coming from renewable energy (RE) resources must increase from around 15% in 2015 to 65% in 2050.[11]

---

[1] 450 ppm as maximum concentration CO_2 allowed in the atmosphere.

Unfortunately, at the current deployment rate, RE technologies are falling short of this ambitious goal. Solar Photovoltaic (PV) panels and onshore wind turbines are the only two technologies that are on track to reach the prescribed targets by 2025.[12] The energy transition towards a more sustainable low-carbon society can not rely solely on these two technologies, whose applicability strongly depends on local conditions, but it must count on a larger variety of technical solutions that are suitable for a wider range of renewable sources and diversity of circumstances. The IEA envisages that many RE sources will be concurrently exploited to guarantee the energy demand of the world by 2050[11] (see Fig. 1.1).
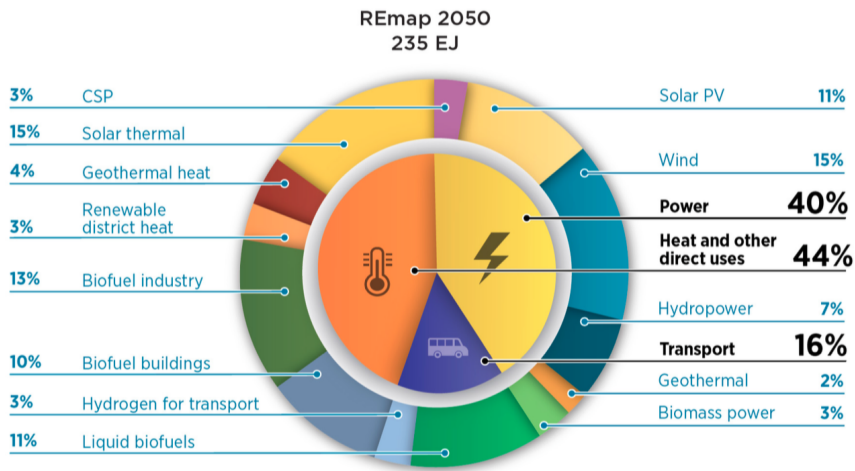
Figure 1.1: Renewable energy use envisaged by the IEA for 2050.[11]

1.1 Towards a more sustainable and integrated distributed scenario

It can be argued that the deployment of RE technologies is strictly connected to the development of the distributed generation (DG) paradigm.[13] In a DG scenario, the energy is produced by a large number of scattered small-scale power plants (from few kW_E to around $\approx 100\,MW_E$). DG differs from the traditional paradigm, called centralized generation (CG), whereby the energy demand is fulfilled by few large power plants. Centralized generation is largely based on the combustion of fossil-fuels. The high cost of extracting fossil fuels from fewer and unevenly distributed locations was the main economical driver for this approach. On the contrary, RE sources, thanks to their diversity, are more uniformly spread all over the earth. As a result, the increasing exploitation of RE sources has been pushing towards the development of a different power generation and distribution

solution.

Renewable distributed power systems are conceivably less affected by the "not in my back yard" phenomenon; hence, they can be located in proximity of the end users. The adjacency to the final energy consumers provides several advantages. For example, power plants can co-generate heat and power. Integrating thermal and electrical supply improves the overall efficiency of the system.[14] Another advantage is that DG systems allow to enormously reduce transmission losses. According to IEA the yearly energy waste due to transmission losses is about the 8% of the world total electricity consumptions, thus equivalent to the electricity used by Germany, France, Italy and Spain in one year.[15]

Importantly, the possibility of operating off-grid makes distributed renewable power plants a promising solution for the electrification of remote and rural areas of the world, where it is often too costly for the local utility companies to extend the grid. According to the last available data of 2016,[10] 1.1 billion people still lack access to electricity, and 2.8 billion people are affected by heating issues and safety problems when cooking. The lack of safe cooking and heating-facilities generates millions of premature deaths every year due to intoxication by indoor air pollution.[10] These conditions have hampered economic progress and are a major contribution to poverty in these areas. Without electricity, children cannot study during nighttime, people cannot run competitive businesses, and hospitals cannot guarantee their services.

1.2   Organic Rankine Cycle power systems

Renewable thermal energy (RTE) sources for power generation (i.e., geothermal reservoir, biomass fuel, and concentrated solar radiation), as shown in Fig. 1.1, can provide a large portion of the world electricity demand in the future. These sources are currently underused. For instance, geothermal reservoirs, the most exploited among these three sources, is only utilized for roughly the $6 - 7\%$ of its estimated global potential.[16] Nevertheless, the rate of conversion of these sources is improving, especially thanks to the market success of DG technologies such as the Organic Rankine Cycle power system.

ORC systems are one of the most promising technology for the exploitation of external thermal sources.[17] Following the working principles of the Rankine Cycle, the energy extracted from the thermal source is transformed into more valuable output: electricity (and thermal energy in case of co-generation). Differently from the traditional Rankine Cycle concept that is at the base of operation of large steam power plants, ORC systems use an organic compound as working fluid in place of water. The possibility of selecting the working medium among the different families of organic compounds (e.g., siloxanes, hdyrocarbons, fluorocarbons, carbon dioxide, etc.) allows to tailor the system to almost any external thermal source in the temperature range from approximately 30°C up to 700°C, and in the power range from few kW_E up to hundreds of MW_E.[18]

In the current literature, often a distinction is made between ORC and super critical carbon dioxide (sCO_2) power systems. Nonetheless, CO_2 is an organic molecule, and, as such, sCO_2 power plants can be included within the category of ORC systems;[2] therefore,

---

[2] A sCO_2 power plant operates according to the Rankine cycle principle if the fluid condenses before pres-

this is assumed in this dissertation. Furthermore, waste-heat is also considered as belonging to the category of renewable thermal energy sources convertable into electricity or mechanical work by means of ORC power plants.

Geothermal power plants. In the last years, many liquid-dominated geothermal reservoirs have been exploited by means of power plants thanks to the advent of ORC technology.[20] ORC systems have provided cost-effective solutions for the conversion of low-temperature (120-150°C) liquid-dominated reservoirs with comparatively low-capacity.[18] Prior to the development of ORC technology, only large-capacity steam-dominated wells were utilized for power generation. As a consequence, most of the high-temperature geothermal wells are already harnessed for energy conversion, while the potential of low-temperature reservoirs has remained very large.[21] Almost the entire geothermal power capacity installed in 2015 came from the installations of ORC power plants.[16] A ORC geothermal power plant is shown in Fig. 1.2.

Figure 1.2: Geothermal ORC power plant of 22 MW installed by Ormat in the Churchill County of Nevada.[22]

Biomass power plants. The capacity of a biomass-fired plant is typically limited to few megawatts because of: i) the high cost of gathering the fuel, ii) the suitability of smaller

---

surisation. This is very often the case.[19]

plants for combine heat and power solutions. In this range of power, ORC systems are technically and economically superior to the more conventional steam plants.[18] Consequently, more than 300 high-temperature ORC power plants fueled with various types of solid biomass have been installed in Europe, North America and Asia in the last 15 years.[17] These plants often feature a CHP arrangement, whereby the thermal energy released by the ORC unit is utilized for low-temperature industrial processes (e.g., wood drying) or for district heating. A biomass-fired ORC power plant is depicted in Fig. 1.3.

Figure 1.3: Biomass-fired ORC power plant constructed by Turboden.[23]

Waste-heat recovery power plants. A substantial reduction of GHG emissions can be achieved by improving the efficiency of energy-intensive industrial manufacturing pro-

cesses (e.g., those of cement plants, steel mills, glassmakers, and refineries). These processes typically release large amounts of energy in the form of waste heat[24] at various temperatures ($120 - 1000$ °C). In this temperature range, waste thermal energy can be effectively converted into electricity or cogenerated using ORC systems.[25] This improves the overall efficiency of the process, as more valuable outputs are obtained with the same consumption of primary energy. Furthermore, since waste heat recovery does not deplete any natural resource, it should be considered completely equivalent to the conversion of a renewable thermal energy source from a regulatory point of view. Figure 1.4 illustrates a WHR ORC power plant, and some of the industrial processes to which this technology can be applied.

Concentrated solar power plants. Photovoltaic (PV) power plants have recently dominated the solar energy scenario, from small to large scale, because the Chinese mass production of PV panels has allowed to reduce the specific costs to half of that of other solar technologies (i.e., concentrated solar power [CSP] using steam-cycle or ORC power plants for conversion). Nevertheless, CSP remains attractive in situations in which the dispatchability of electricity is of primary importance, because they can be coupled with thermal storage systems. Other advantages of ORC power plants are that i) they are suitable for cogeneration and integrated desalination[26] for maximum energy efficiency, and ii) they can concurrently convert two or more renewable energy sources[27,28] (e.g, solar and biomass, and solar and WHR), thus ensuring continuous power generation. A CSP ORC system is represented in Fig. 1.5.

New applications. Today, ORC technology is commercially viable for the exploitation of the mentioned renewable thermal energy sources in the medium-to-large power capacity range (from $500\,\mathrm{kW_E}$ up to tens of $\mathrm{MW_E}$) as testified by the successful companies that manufacture these systems.[22,23,29] The main applications in order of installed capacity are: geothermal, biomass, WHR, and CSP.

By contrast, small-capacity ORC power systems ($\approx 1 - 50$ kW) are still at prototyping level because of their relatively lower technological maturity,[17] due to a number of techno-economic challenges. Nonetheless, the benefit of exploiting distributed small-capacity sources remains indisputable. Hence, many novel research endeavors are focused on the development of mini-ORC solutions.[18] For example, considerable research and development efforts have been dedicated in recent times to mini-ORC systems for heat recovery from automotive engines,[30] and, more specifically, from long-haul truck diesel engines. Some studies have shown that the so-called combined cycle powertrain might enable to surpass the historic limit of 50% fuel efficiency.[31] In addition, the automotive sector has the market dimension needed to ignite the economy of production (large numbers of standardized units). If this industrial application is successful, several new large markets for mini-ORC power systems will likely open up. For instance, small biomass-fired CHP ORC systems can be used in developing countries where low-cost solid biomass fuel is locally available, and, likewise, CSP applications in countries of the solar belt.

Figure 1.4: WHR ORC power plant constructed by Turboden,[23] and industrial process plants (e.g., cement plants, steel mills, glassmakers, and refineries) to which the WHR ORC technology can be applied.

One of the reason why small ORC systems are not commercially available yet is due to the low return on investment (ROI) that would be achievable with current technology. The main issues are two: i) high specific cost of investment due to the relatively low power capacity; ii) relatively low conversion efficiency. While cost reduction can be achieved with economy of production because no inherently expensive materials of manufacturing technologies are needed, increasing the efficiency is quite a complex task to accomplish.

The thermodynamic efficiency of a power cycle grows with the increasing of the difference between the average temperatures at which the thermal energy is transferred to

Figure 1.5: CSP ORC power system manufactured by Turboden. [23]

the power system from the hot source (in this case the RTE) and the average temperature at which the thermal energy is ejected from the system to the environment. [32] While decreasing the temperature of energy discharge is intrinsically limited by the ambient conditions, increasing the thermal energy input temperature depends mainly on the thermodynamic properties of the working fluid and its thermal stability. [18,33]

Satisfactory thermodynamic efficiency can be obtained by employing working fluids with a high molecular complexity, thus high critical temperature and low critical pressure, which are also highly thermally stable (e.g., siloxanes). [34,35] On the other hand, the employment of these fluids results into ORC configurations in which the turbine must operate under an extremely large expansion flow ratio (in the range from 30 to 60). [36] While in medium to large ORC systems a cost-effective and efficient multi-stage turbine can be designed even if the expansion ratio is large, [23] in case of small ORC power plants two solutions are possible in order to keep the cost within acceptable limits. Volumetric expanders can be efficient and cost-effective, but they are inherently limited to low expansion ratio, thus cannot be used with molecularly complex fluids. High-speed mini turbines can in principle operate with large expansion ratio, but the design envelope is extremely challenging because of the need to achieve high expansion efficiency in single-stage arrangements operating under severe supersonic flow conditions. [37]

If the fluid dynamic performance of the turbine is poor, the conversion efficiency of the system is also constrained to be low. [36] Figure 1.6 shows the trend of the net system efficiency as function of turbine efficiency for a regenerative cycle configuration. Therefore, achieving high fluid-dynamic performance of the turbine is one of the key factors that can determine the economical success of small ORC turbogenerators. The
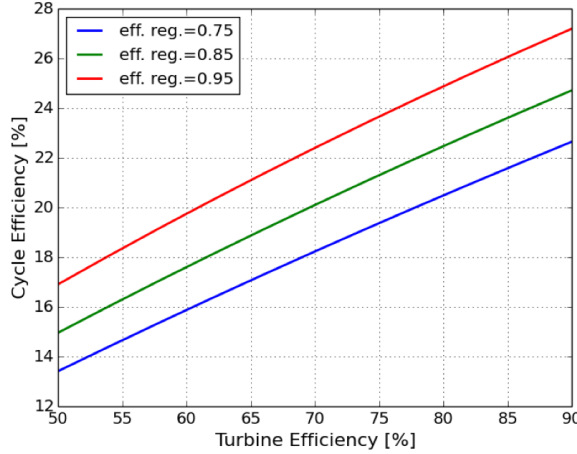
Figure 1.6: Trend of the net system efficiency as function of turbine efficiency for a re-generative cycle configuration.

improvement of the performance and cost-effectiveness of the heat exchangers and of the pump are also important. However, the performance of heat exchangers is determined to a large extent from the addition of heat transfer surface, which increases the specific cost, while the improvement of the fluid dynamic performance of the pump has an order of magnitude smaller effect on the system efficiency if compared to that of the turbine. The improvement of the fluid dynamic performance of the turbine does not necessarily increase the manufacturing cost and it has only an impact on R&D costs.[18] This also means that an improvement on the fluid-dynamic performance of the turbine has always a positive effect on the ROI of the technology regardless the power capacity of the system. For this reason, despite being more crucial for small size systems, the topic of the fluid-dynamic design of ORC turbomachinery is treated in this dissertation without specific reference to the size of the component, and without referring to any particular type of turbomachinery configuration (i.e., axial or radial).

1.3 The challenges of fluid-dynamic design of ORC turbomachinery

The fluid-dynamic design of ORC turbomachinery differs from the design of traditional machines (i.e., steam and gas turbines), and this is mainly due to the different thermo-physical properties and gas dynamic behavior of the organic fluid being expanded or compressed.[38]

With respect to conventional fluids, such as water and air, organic fluids, which are

more suitable for small to medium capacity turbines, have larger molecular weight. In general, the larger is the molecular weight the lower is the turbine specific work. This allows to design compact turbines with few stages or just one stage. However, the high expansion ratio across the turbine together with the comparatively low speed of sound of the organic fluids lead to turbines working in the supersonic flow regime,[39,40] in which the occurrence of shock waves and chocked flows negatively affect the fluid-dynamic performance.[41]

The complexity of the design of ORC turbomachinery is further enhanced by the non ideal behavior of the organic fluids at the needed operating conditions. The expansion and compression of these fluids, across the turbomachinery components of the system, occurs in part in the so-called non-ideal compressible fluid-dynamic (NICFD) regime in proximity of the saturated vapor curve, or close to the critical point. For example, the compressor of large capacity sCO_2 systems typically operates close to the critical point of the fluid.[42,43] In such conditions, the relation among thermodynamic properties significantly departs from the ideal gas law (e.g., relation between temperature, pressure, and density over an isentropic expansion/compression) affecting the volume variation. In addition, and importantly, also the speed of sound varies along the expansion/compression in a significantly different way, if compared to that of an ideal gas.[44] Hence, accurate and complex models of thermodynamic and transport property models of the fluids must be used in the design of turbomachinery operating in these conditions. Figure 1.7, for example, shows the results of the design of a shock-less 2D nozzle obtained with an accurate thermodynamic model and with the ideal gas model for the same operating conditions. The difference between the two geometries clearly underlines the importance of correctly estimating thermodynamic properties.

In addition, very few fundamental experiments have been conducted to characterize the gasdynamics of NICFD flows,[46] and no experimental campaigns have been carried out to assess the validity and possibly extend the body of empirical knowledge that was acquired for the design of conventional turbomachinery and that is routinely used to design the highly efficient turbomachines for gas and steam power plants.

1.4 CFD Aided Design of ORC turbomachinery

In the last years, considerable progress has been achieved in the fluid dynamic design of ORC turbomachinery thanks to the development of specialized CFD tools and ad hoc methods.[47,48] Methods capable of correctly simulating NICFD flows, and thus of performing high fidelity fluid dynamic simulations of ORC turbomachinery have partially filled the gap of missing knowledge due to the lack of experimental information, and have helped designers to improve their understanding of complex NICFD phenomena.[38] However, the design problem is quite complex, and only relying on flow simulation and analysis does not allow to achieve the level of efficiency that is typical of conventional turbomachinery.[49] The current trend is to adopt fluid dynamic design methods in which CFD is coupled with numerical optimization techniques[50,51] in order to obtain optimal flow passage geometries. These design techniques are also known as fluid dynamic shape
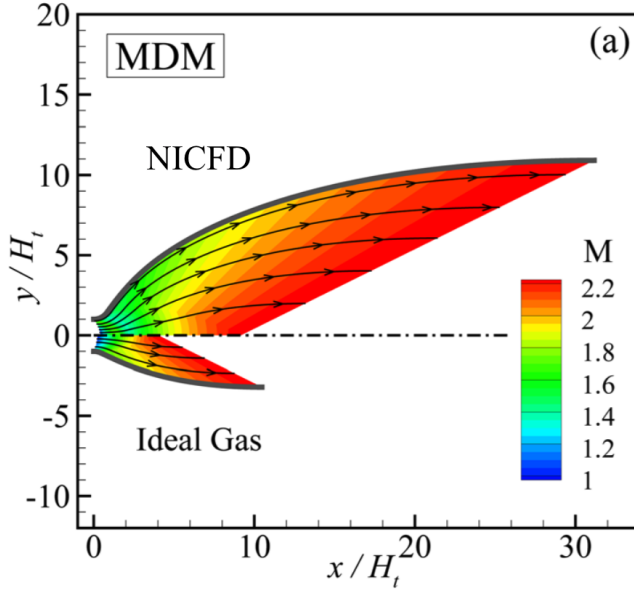
Figure 1.7: Impact of different thermodynamic models on the design of a shock-less nozzle for organic flows. [45]

optimization (FSO) methods.

With FSO methods, the optimal design solution is found by minimizing or maximizing a certain objective function (e.g., minimizing fluid dynamic losses computed with CFD simulations) using either gradient-free or gradient based optimization algorithms. Gradient-free algorithms (e.g., genetic algorithms) search for an optimal shape using only the information on the objective function value, and they are often coupled with surrogate models to reduce the computational cost. Yet, the number of function evaluations (CFD runs) necessary to converge to an optimum solution are comparatively large, and, consequently, only few design variables can be concurrently optimized. [52,53]

By contrast, gradient-based algorithms can reach an optimal solution in far fewer iterations. These techniques require not only the computation of the objective function, but also the estimation of its gradient with respect to the design variables. Nevertheless, if the gradient is estimated with adjoint methods, its computational cost remains of the same order of magnitude of that of the objective function, regardless of the number of design variables. [54]

Despite the potential disadvantage of converging to local optimal solutions, gradient-based algorithms coupled with adjoint methods remains the only viable technique to solve FSO problem in turbomachinery because of the large number of design variables typically involved in the process. [53]

1.5   Research motivation

The adjoint method is based on the theory of *optimal control of systems governed by partial differential equations*.[55] In 1984 Pironneau introduced it into the field of fluid-mechanics,[56] and, later in 1988, Jameson applied it for the first time to transonic FSO problems.[57]

The adjoint equations can be derived either in the continuous or discrete form. With the continuous approach, the adjoint equations are first derived from the flow governing equations and only then discretized. On the contrary, with the discrete approach, the adjoint system is obtained by applying control theory directly to the discretized flow equations. A discrete adjoint code typically requires more memory and has a higher run time than a code based on the continuous adjoint formulation. Nonetheless, a discrete adjoint provides the exact gradients of the discretized functionals, namely, the adjoint derivatives are identical to those obtained from the flow solver.[58,59]

While the adjoint method has been extensively applied to external FSO problems,[60–65] its application to the FSO of turbomachinery has been lagging far behind due to the higher complexity of deriving the adjoint equations for internal flow problems.[53] Only in the last 10 to 15 years some research effort has been made to extend the adjoint method to the FSO of turbomachinery.[66–78] However, most of the works are restricted to 1) the optimization of isolated blades (either statoric or rotoric) neglecting the importance of the interaction of the blade rows in a multi-stage configuration,[79] 2) the use of the constant eddy viscosity approximation[80] to avoid the derivation of the turbulent transport equations.

The derivation of the adjoint equations becomes even more challenging in the context of NICFD, for which complex fluid thermodynamic and transport models must be adopted, resulting in the need of specialized numerical methods.[47,48] Despite that, recent work on the subject has demonstrated the potential of adjoint-based method for the FSO of NICFD flows occurring in ORC turbine cascades.[50,81] However, this approach was limited to the inviscid flows around 2D isolated blades, restricting its applicability to rather simple academic problems.

The research documented in this PhD dissertation aimed at extending the adjoint method in order to perform the fully-turbulent FSO of 3D multi-stage ORC turbomachinery. As such, the developed method not only includes the exact derivation of the turbulence equations and of the mixing-plane boundary conditions,[82] but it is also generalized to deal with arbitrary thermophysical fluid models.

1.6   Computational playground

The adjoint solver was obtained by linearizing the discretized flow equations by means of Automatic Differentiation (AD). In particular, a holistic linearization approach was adopted, whereby AD is applied in a black-box manner to the entire source code.[83] This is accomplished with the help of modern meta-programming features in combination with a reformulation of the state constraint into a fixed-point problem.[84] The result is a fast

and accurate discrete adjoint solver that includes all the flow solver features, such as arbitrarily complex fluid thermodynamic models and turbulence models and interaction among multiple blades.

The new RANS adjoint solver was developed by leveraging on the open-source software infrastructure of SU2,[85] a platform conceived for solving multi-physics PDE and PDE-constrained optimization problems using general unstructured meshes. Before applying the AD tool to derive the adjoint equations, the SU2 RANS solver was extended to model NICFD flows and to simulate flows in turbomachinery. The implementation of these new models were validated against experimental data available for both conventional and ORC turbines.

The capabilities of the new design tool were then tested on many 2D and 3D test cases. The results demonstrate the importance and benefit of accurately modeling non-ideal thermodynamic and viscous effects when adjoint-based FSO methods are applied to the design of ORC turbomachinery.

1.7   Thesis outline

This document contains three main chapters, each representing a building block towards the accomplishment of the main goal of this PhD project, and a final concluding chapter that summarizes all the research outcomes of this work and proposes future steps for research in this field. The content of the main three chapters was partly presented in international conferences and/or appeared in peer-reviewed international scientific journals.

1.7.1   Main chapters

Chapter 2 presents the extension of the RANS framework of the SU2 software to simulate turbulent flows of components working in the NICFD thermodynamic region. Specifically, the RANS equations, the convective numerical schemes, and the viscous numerical schemes were generalized for the use of complex thermo-physical laws. The accuracy of the newly implemented numerical models were verified on a series of test cases: both numerical and analytical. The work described in this chapter demonstrates that the newly developed framework is capable of accurately simulate NICFD turbulent flows.

Chapter 3 documents the implementation and application of a fully-turbulent discrete adjoint for NICFD applications. Building on top of the work described in chapter 2, the RANS framework of SU2 was first enriched with appropriate inflow and outflow boundary conditions to accurately simulate the flow in two-dimensional turbomachinery test-cases. An adjoint solver was then derived by means of advanced AD techniques in order to resolve shape-optimization design problems for ORC turbomachinery. The capability of the new design tool was successfully tested on two paradigmatic cases: a supersonic and a transonic two-dimensional ORC turbine cascade. In brief, the work described in chapter 3 represents the proof of concept that the method adopted provides a computational efficient and accurate design tool, whose capabilities can be potentially extended to

industrial 3D multi-row applications.

Chapter 4 reports, in conclusion, the extension of the adjoint method, introduced in chapter 3, to 3D multi-stage turbomachienry. To this end, a conservative and non-reflecting mixing-plane method was first implemented within the RANS framework of SU2. Following the same approach presented in chapter 3, the RANS solver was then linearized to obtain its adjoint counterpart. The accuracy of the RANS solver was tested by comparing numerical simulations with experimental results available for standard turbomachinery applications and against some unique NICFD experimental results available for a mini-ORC turbine. The accuracy of the gradient information provided by the adjoint was thoroughly verified against the sensitivity computed with finite-differences. The newly developed design framework was then applied on a 3D multi-stage turbomachinery test-case.

References

[1] Nations, U., 2015. United nations sustainable development goals. `http://www.un.org/sustainabledevelopment/sustainable-development-goals/`.

[2] IPCC, 2014. *Climate Change 2014: Synthesis Report. Contribution of Working Groups I, II and III to the Fifth Assessment Report of the Intergovernmental Panel on Climate Change*. Intergovernmental Panel on Climate Change (IPCC), Geneva, Switzerland.

[3] IEA, 2017. *CO2 Emissions from Fuel Combustion 2017*. OECD Publishing.

[4] IEA, 2017. Iea scenarios and projections. `https://www.iea.org/publications/scenariosandprojections/`.

[5] IEA, 2008. *World Energy Outlook 2008*. OECD Publishing.

[6] IEA, 2016. *World Energy Outlook 2016*. OECD Publishing.

[7] Tschakert, P., 2015. "1.5 °C or 2 °C: a conduit's view from the science-policy interface at cop20 in lima, peru". *Climate Change Responses,* **2**(1).

[8] International, O. C., 2017. *The Skys Limit: Why the Paris Climate Goals Require a Managed Decline of Fossil Fuel Production*. http://priceofoil.org/.

[9] UNFCCC, 2015. *Adoption of the Paris Agreement*. United Nations.

[10] IEA, 2017. *World Energy Outlook 2017*. OECD Publishing.

[11] IEA, I., 2017. *Perspective for Energy Transition: Investment needs for a Low-Carbon Energy System*. IEA, IRENA.

[12] IEA, 2017. *Energy Technology Perspective 2017*. OECD Publishing.

[13] Ramakumar, R., and Chiradeja, P., 2004. "Distributed generation and renewable energy systems". In Energy Conversion Engineering Conference, 2002. IECEC'02. 2002 37th Intersociety, IEEE, pp. 716–724.

[14] Onovwiona, H., and Ugursal, V. I., 2006. "Residential cogeneration systems: review of the current technology". *Renewable and sustainable energy reviews,* **10**(5), pp. 389–431.

[15] IEA, 2017. Electric power transmission and distribution losses. `https://data.worldbank.org/indicator/EG.ELC.LOSS.ZS`.

[16] GEA, 2016. *2016 Annual U.S. and Global Geothermal Power Production Report*.

[17] Macchi, E., and Astolfi, M., 2016. *Organic Rankine Cycle (ORC) Power Systems: Technologies and Applications*. Woodhead Publishing.

[18] Colonna, P., Casati, E., Trapp, C., Mathijssen, T., Larjola, J., Turunen-Saaresti, T., and Uusitalo, A., 2015. "Organic rankine cycle power systems: from the concept to current technology, applications, and an outlook to the future". *Journal of Engineering for Gas Turbines and Power,* **137**(10), p. 100801.

[19] Feher, E. G., 1968. "The supercritical thermodynamic power cycle". *Energy conversion,* **8**(2), pp. 85–90.

[20] Bronicki, L. Y., 2008. "Advanced power cycles for enhancing geothermal sustainability 1,000 mw deployed worldwide". In Power and Energy Society General Meeting-Conversion and Delivery of Electrical Energy in the 21st Century, 2008 IEEE, IEEE, pp. 1–6.

[21] DiPippo, R., 2012. *Geothermal power plants: principles, applications, case studies and environmental impact*. Butterworth-Heinemann.

[22] ORMAT. Ormat Technologies, Inc.. `http://ormat.com/en/home/a/main/`.

[23] TURBODEN. Turboden S.p.A. `https://turboden.com/`.

[24] Campana, F., Bianchi, M., Branchini, L., De Pascale, A., Peretto, A., Baresi, M., Fermi, A., Rossetti, N., and Vescovo, R., 2013. "Orc waste heat recovery in european energy intensive industries: Energy and ghg savings". *Energy Conversion and Management,* **76**, pp. 244–252.

[25] Karellas, S., Leontaritis, A.-D., Panousis, G., Bellos, E., and Kakaras, E., 2013. "Energetic and exergetic analysis of waste heat recovery systems in the cement industry". *Energy,* **58**, pp. 147–156.

[26] Wang, L., Roskilly, A. P., and Wang, R., 2014. "Solar powered cascading cogeneration cycle with orc and adsorption technology for electricity and refrigeration". *Heat Transfer Engineering,* **35**(11-12), pp. 1028–1034.

[27] Jradi, M., and Riffat, S., 2014. "Modelling and testing of a hybrid solar-biomass orc-based micro-chp system". *International Journal of Energy Research,* **38**(8), pp. 1039–1052.

[28] Astolfi, M., Xodo, L., Romano, M. C., and Macchi, E., 2011. "Technical and economical analysis of a solar–geothermal hybrid plant based on an organic rankine cycle". *Geothermics,* **40**(1), pp. 58–68.

[29] EXERGY. Exergy S.p.A.. `http://exergy-orc.com/`.

[30] Sprouse, C., and Depcik, C., 2013. "Review of organic rankine cycles for internal combustion engine exhaust waste heat recovery". *Applied thermal engineering,* **51**(1), pp. 711–722.

[31] Lang, W., Colonna, P., and Almbauer, R., 2013. "Assessment of waste heat recovery from a heavy-duty truck engine by means of an orc turbogenerator". *Journal of Engineering for Gas Turbines and Power,* **135**(4), p. 042313.

[32] Cengel, Y. A., and Boles, M. A., 2002. "Thermodynamics: an engineering approach". *Sea,* **1000**, p. 8862.

[33] Pasetti, M., Invernizzi, C. M., and Iora, P., 2014. "Thermal stability of working fluids for organic rankine cycles: An improved survey method and experimental results for cyclopentane, isopentane and n-butane". *Applied Thermal Engineering,* **73**(1), pp. 764–774.

[34] Colonna, P., Nannan, N., and Guardone, A., 2008. "Multiparameter equations of state for siloxanes:[(ch3) 3-si-o1/2] 2-[o-si-(ch3) 2] i= 1,, 3, and [o-si-(ch3) 2] 6". *Fluid Phase Equilibria,* **263**(2), pp. 115–130.

[35] Colonna, P., Guardone, A., and Nannan, N., 2007. "Siloxanes: a new class of candidate bethe-zeldovich-thompson fluids". *Physics of Fluids,* **19**(8), p. 086102.

[36] Bahamonde, S., Pini, M., De Servi, C., Rubino, A., and Colonna, P., 2017. "Method for the preliminary fluid dynamic design of high-temperature mini-organic rankine cycle turbines". *Journal of Engineering for Gas Turbines and Power,* **139**, pp. 082606–1.

[37] Harinck, J., Turunen-Saaresti, T., Colonna, P., Rebay, S., and van Buijtenen, J., 2010. "Computational study of a high-expansion ratio radial organic rankine cycle turbine stator". *Journal of Engineering for Gas Turbines and Power,* **132**(5), p. 054501.

[38] Colonna, P., Harinck, J., Rebay, S., and Guardone, A., 2008. "Real-gas effects in organic rankine cycle turbine nozzles". *Journal of Propulsion and Power,* **24**(2), pp. 282–294.

[39] Pini, M., Persico, G., Casati, E., and Dossena, V., 2013. "Preliminary design of a centrifugal turbine for organic rankine cycle applications". *Journal of Engineering for Gas turbines and power,* **135**(4), p. 042312.

[40] Casati, E., Vitale, S., Pini, M., Persico, G., and Colonna, P., 2014. "Centrifugal turbines for mini-organic rankine cycle power systems". *Journal of Engineering for Gas Turbines and Power,* **136**(12), p. 122607.

[41] Denton, J. D., and Cumpsty, N., 1993. "Loss mechanisms in turbomachines.". *Journal of Turbomachinery. Transactions of the ASME,* **115**(4), pp. 621–656.

[42] Pecnik, R., Rinaldi, E., and Colonna, P., 2012. "Computational fluid dynamics of a radial compressor operating with supercritical co2". *Journal of Engineering for Gas Turbines and Power,* **134**(12), p. 122301.

[43] Rinaldi, E., Pecnik, R., and Colonna, P., 2015. "Computational fluid dynamic simulation of a supercritical co2 compressor performance map". *Journal of Engineering for Gas Turbines and Power,* **137**(7), 07, pp. 072602–072602–7.

[44] Cramer, M., 1991. "On the mach number variation in steady flows of dense hydrocarbons". *ASME J. Fluids Eng.,* **113**(4), pp. 675–680.

[45] Guardone, A., Spinelli, A., and Dossena, V., 2013. "Influence of molecular complexity on nozzle design for an organic vapor wind tunnel". *Journal of Engineering for Gas Turbines and power,* **135**(4), p. 042307.

[46] Spinelli, A., Cammi, G., Zocca, M., Gallarini, S., Cozzi, F., Gaetani, P., Dossena, V., and Guardone, A., 2017. "Experimental observation of non-ideal expanding flows of siloxane mdm vapor for orc applications". *Energy Procedia,* **129**, pp. 1125–1132.

[47] Colonna, P., and Rebay, S., 2004. "Numerical simulation of dense gas flows on unstructured grids with an implicit high resolution upwind euler solver". *International journal for numerical methods in fluids,* **46**(7), pp. 735–765.

[48] Rinaldi, E., Pecnik, R., and Colonna, P., 2014. "Exact jacobians for implicit navier-stokes simulations of equilibrium real gas flows". *Journal of Computational Physics,* **270**, pp. 459–477.

[49] Pini, M., De Servi, C., Burigana, M., Bahamonde, S., Rubino, A., Vitale, S., and Colonna, P., 2017. "Fluid-dynamic design and characterization of a mini-orc turbine for laboratory experiments". *Energy Procedia,* **129**, pp. 1141–1148.

[50] Pini, M., Persico, G., Pasquale, D., and Rebay, S., 2015. "Adjoint method for shape optimization in real-gas flow applications". *Journal of Engineering for Gas Turbines and Power,* **137**(3), p. 032604.

[51] Persico, G., 2017. "Evolutionary optimization of centrifugal nozzles for organic vapours". In Journal of Physics: Conference Series, Vol. 821, IOP Publishing, p. 012015.

[52] Quagliarella, D., 1998. "Genetic algorithms and evolution strategy in engineering and computer science: recent advances and industrial applications". *John Wiley & Son Ltd.*

[53] Li, Z., and Zheng, X., 2017. "Review of design optimization methods for turbomachinery aerodynamics". *Progress in Aerospace Sciences,* **93**, pp. 1–23.

[54] Peter, J., and Dwight, R., 2009. "Numerical sensitivity analysis for aerodynamic optimization: A survey of approaches". *Computer & Fluids,* **39**(3), pp. 373–391.

[55] Lions, J. L., 1971. *Optimal control of systems governed by partial differential equations (Grundlehren der Mathematischen Wissenschaften)*, Vol. 170. Springer Berlin.

[56] Pironneau, O., 2012. *Optimal shape design for elliptic systems.* Springer Science & Business Media.

[57] Jameson, A., 1988. "Aerodynamic design via control theory". *Journal of scientific computing,* **3**(3), pp. 233–260.

[58] Nadarajah, S., and Jameson, A., 2000. "A comparison of the continuous and discrete adjoint approach to automatic aerodynamic optimization". In 38th Aerospace Sciences Meeting and Exhibit, p. 667.

[59] Nadarajah, S., and Jameson, A., 2001. "Studies of the continuous and discrete adjoint approaches to viscous automatic aerodynamic shape optimization". In 15th AIAA Computational Fluid Dynamics Conference, p. 2530.

[60] Jameson, A., and Reuther, J., 1994. "Control theory based airfoil design using the euler equations". *5th AIAA/USAF/NASA Symposium on Multidisciplinary Analysis and Optimization.*

[61] Jameson, A., 1995. "Optimum aerodynamic design using cfd and control theory". In 12th Computational Fluid Dynamics Conference, p. 1729.

[62] Giles, M. B., and Pierce, N. A., 2000. "An introduction to the adjoint approach to design". *Flow, turbulence and combustion,* **65**(3-4), pp. 393–415.

[63] Kim, S., Alonso, J. J., and Jameson, A., 2004. "Multi-element high-lift configuration design optimization using viscous continuous adjoint method". *Journal of Aircraft,* **41**(5), pp. 1082–1097.

[64] Nadarajah, S. K., and Jameson, A., 2007. "Optimum shape design for unsteady flows with time-accurate continuous and discrete adjoint method". *AIAA journal,* **45**(7), pp. 1478–1491.

[65] Nadarajah, S., and Jameson, A., 2007. "Optimum shape design for unsteady three-dimensional viscous flows using a nonlinear frequency-domain method". *Journal of Aircraft,* **44**(5), pp. 1513–1527.

[66] Papadimitriou, D., and Giannakoglou, K., 2006. "A continuous adjoint method for the minimization of losses in cascade viscous flows". In 44th AIAA Aerospace Sciences Meeting and Exhibit, p. 49.

[67] Papadimitriou, D., and Giannakoglou, K., 2007. "Total pressure loss minimization in turbomachinery cascades using a new continuous adjoint formulation". *Proceedings of the Institution of Mechanical Engineers, Part A: Journal of Power and Energy,* **221**(6), pp. 865–872.

[68] Corral, R., and Gisbert, F., 2008. "Profiled end wall design using an adjoint navier–stokes solver". *Journal of Turbomachinery,* **130**(2), p. 021011.

[69] Luo, J., Xiong, J., Liu, F., and McBean, I., 2011. "Three-dimensional aerodynamic design optimization of a turbine blade by using an adjoint method". *Journal of Turbomachinery,* **133**(1), p. 011026.

[70] Luo, J., Zhou, C., and Liu, F., 2014. "Multipoint design optimization of a transonic compressor blade by using an adjoint method". *Journal of Turbomachinery,* **136**(5), p. 051005.

[71] Mueller, L., and Verstraete, T., 2017. "Cad integrated multipoint adjoint-based optimization of a turbocharger radial turbine". *International Journal of Turbomachinery, Propulsion and Power,* **2**(3), p. 14.

[72] Mousavi, A., and Nadarajah, S., 2010. "Heat transfer optimization of gas turbine blades using an adjoint approach". In 13th AIAA/ISSMO Multidisciplinary Analysis Optimization Conference, p. 9048.

[73] Mousavi, A., and Nadarajah, S., 2011. "Adjoint-based multidisciplinary design optimization of cooled gas turbine blades". In 49th AIAA Aerospace Sciences Meeting including the New Horizons Forum and Aerospace Exposition, p. 1131.

[74] Verstraete, T., Müller, L., and Müller, J.-D., 2017. "Cad-based adjoint optimization of the stresses in a radial turbine". In ASME Turbo Expo 2017: Turbomachinery Technical Conference and Exposition, American Society of Mechanical Engineers, pp. V02CT47A025–V02CT47A025.

[75] Wang, D., and He, L., 2010. "Adjoint aerodynamic design optimization for blades in multistage turbomachinespart i: Methodology and verification". *Journal of Turbomachinery,* **132**(2), p. 021011.

[76] Wang, D., He, L., Li, Y., and Wells, R., 2010. "Adjoint aerodynamic design optimization for blades in multistage turbomachinespart ii: Validation and application". *Journal of Turbomachinery,* **132**(2), p. 021012.

[77] Walther, B., and Nadarajah, S., 2015. "Adjoint-based constrained aerodynamic shape optimization for multistage turbomachines". *Journal of Propulsion and Power,* **31**(5).

[78] Walther, B., and Nadarajah, S., 2015. "Optimum shape design for multirow turbomachinery configurations using a discrete adjoint approach and an efficient radial basis function deformation scheme for complex multiblock grids". *Journal of Turbomachinery,* **137**(8), p. 081006.

[79] Denton, J. D., 1990. "The calculation of three dimensional viscous flow through multistage turbomachines". In ASME 1990 International Gas Turbine and Aeroengine Congress and Exposition, American Society of Mechanical Engineers, pp. V001T01A009–V001T01A009.

[80] Marta, A. C., and Shankaran, S., 2013. "On the handling of turbulence equations in rans adjoint solvers". *Computers & Fluids,* **74**, pp. 102–113.

[81] Pini, M., Persico, G., and Dossena, V., 2014. "Robust adjoint-based shape optimization of supersonic turbomachinery cascades". In ASME Turbo Expo 2014: Turbine Technical Conference and Exposition, American Society of Mechanical Engineers, pp. V02BT39A043–V02BT39A043.

[82] Saxer, A. P., and Giles, M. B., 1993. "Quasi-three-dimensional nonreflecting boundary conditions for euler equations calculations". *Journal of Propulsion and Power,* **9**(2), pp. 263–271.

[83] Sagebaum, M., Albring, T., and Gauger, N. R., 2017. Codipack ¢ code differentiation package — scientific computing.

[84] Albring, T. A., Sagebaum, M., and Gauger, N. R., 2016. "Efficient aerodynamic design using the discrete adjoint method in su2". *17th AIAA/ISSMO Multidisciplinary Analysis and Optimization Conference*.

[85] Economon, T. D., Palacios, F., Copeland, S. R., Lukaczyk, T. W., and Alonso, J. J., 2015. "Su2: an open-source suite for multiphysics simulation and design". *AIAA Journal*.

2

Extension of a RANS solver to the simulation of fluid flows modelled with complex thermophysical laws

Abstract *This chapter presents the extension of the open source SU2 software suite to perform turbulent Non-Ideal Compressible Fluid-Dynamics (NICFD) simulations. A new built-in thermodynamic library was developed and tightly coupled with the existing structure of the code, properly reorganized for accommodating arbitrary thermophysical models. The library implements simple models and interfaces to an external software for a more accurate estimation of thermophysical properties of NICFD pure fluids and mixtures. Moreover, the Reynolds-averaged Navier-Stokes (RANS) equations are spatially discretized by resorting to suitably defined convective and viscous numerical schemes for general fluids. The capabilities of the code are finally verified on inviscid and turbulent flow problems against solutions obtained with a different NICFD solver and known analytical ones. The results prove that SU2 is comparatively accurate and computationally efficient with respect to existing codes. Ultimately, SU2 can be considered a trustworthy tool for NICFD-based simulations and the future pillar of advanced automated fluid-dynamic design techniques involving complex fluid laws.*

2.1   Introduction

Non-Ideal Compressible Fluid-Dynamics (NICFD) is the discipline devoted to the study of the thermo-physical characteristics of fluid flows departing from gas ideality, namely flows not obeying to the perfect gas law.[1] Supercritical flows, dense vapors, and two-phase flows belong to this category. At high reduced pressure and temperature, close to the saturation curve the speed of sound is largely sensitive to density variations along isentropes. Consequently, the fluid flow departs from the ideality assumption and under particular conditions may even exhibit non-classical gas-dynamic phenomena, which are governed by the value of the fundamental derivative of gas-dynamics Γ.[2] A non-monotonic Mach number trend along expansion is typical for $0 < \Gamma < 1$, while negative $\Gamma < 0$ values admit the occurrence of inverse gas-dynamics phenomena such as rarefaction shock waves, splitting waves or even composite waves. Inverse gas-dynamics behavior has been theoretically predicted for heavy complex molecules[3] in the vapor region, and a recent study discovered that two-phase rarefaction shock waves are physically realizable close to the critical point of simple compounds.[4]

Applications of NICFD flows to industrial problems are already numerous and spread over heterogeneous fields. The Organic Rankine Cycle (ORC) turbogenerators, which are energy conversion systems renowned for the efficient exploitation of renewable power sources,[5–9] are one example. Refrigeration industry is looking at novel solutions using supercritical CO_2 streams in compressors (sCO_2), and a number of research projects are actively ongoing in this field for defining implications in terms of turbomachinery design issues.[10,11] NICFD flows frequently occur in pharmaceutical processing,[12] transportation of fuels at high-speed,[13] and in transonic and supersonic wind tunnels.[14] Furthermore, the increasingly stringent environmental regulation in the aerospace sector is pushing the attention towards green technologies for next generation aircrafts, such as unconventional compact on-board energy systems for optimal thermal management.[15] The successful deployment of these sustainable technologies is primarily dictated by the per-

formance maximization of their components (e.g. turbomachinery, heat exchangers, ejectors) which can be only driven by CFD, as non-ideal flows usually exhibit gas-dynamic phenomena largely unpredictable with simplified methods. [2] To the authors knowledge, there is currently no computational infrastructure providing analysis and design capability for non-ideal fluid flows. Robust and accurate simulations of non-ideal fluid flows is still a challenge, and the quasi-absence of experimental data in the thermodynamic regions of interest renders uncertain the reliability of the physical models embedded in CFD tools. i.e. the thermo-physical and turbulence models. [16]

The SU2 software suite [17] has recently gained large interest as open-source platform for solving multi-physics PDE problems and PDE-constrained optimization problems on general unstructured meshes. The code resolves steady and unsteady Reynolds-Averaged Navier-Stokes (RANS) equations for incompressible and compressible, laminar and fully turbulent, flows. As unique feature, SU2 accommodates built-in design functionalities through a continuous and a discrete adjoint solver. Given its design capabilities, the SU2 suite was, therefore, chosen as a reference CFD tool within this PhD project with the final goal to provide the NICFD community with a tool which is capable not only to compute fast and accurate CFD analysis, but also to perform design of components for NICFD applications.

The work described in this chapter documents the first step towards this ambitious goal, namely the extension of the RANS solver of SU2 to the simulation of turbulent NICFD flows. This was accomplished by enriching the CFD suite with a new thermo-physical library. The latter was implemented following the same programming paradigm of SU2: a high level of abstraction and modularity with the aim of easing the implementation of new models in future releases. The code was properly re-organized for accommodating the new library, which currently contains three built-in equation of state (EoS): the polytropic ideal gas (PIG), the polytropic Van der Waals (PVdW), and the polytropic Peng-Robinson (PR) models. In addition, the library interfaces to an external software for an even more accurate estimation of thermo-physical properties of pure fluids and mixtures. [18]

Concerning numerical methods, the inviscid fluxes and Jacobian contribution were generalized following the Vinokur-Montagnè approximate Riemann solver (ARS), [19,20] while the Averaged-Gradient (AVG) formulation was used for the viscous counterpart. [21] The new solver is capable of solving the fully compressible turbulent Navier-Stokes equations with arbitrarily complex equations of state using the Spalart-Allamaras (SA) and the Menter Shear-Stress-Tensor kω-SST turbulence models. [22] In the end, the code is built to be a versatile platform for simulating the flow physics of dense vapors of pure fluids, mixtures and two-phase flows at equilibrium conditions with explicit and implicit time-marching schemes.

These new features are tested on a model problem, such as the prediction of a rarefaction shock-wave over a wedge, and on the supersonic flow within a converging-diverging nozzle that closely resembles the flow within ORC blade passages. The rarefaction shock-wave numerical solution obtained with SU2 was verified against the available analytical solution, while the flow solution around the nozzle was qualitatively and quantitatively

verified by comparison with the results obtained with ANSYS-CFX.[23] The latter is a commercial CFD software widely adopted for the analysis of NICFD applications. The collection of test cases not only provides evidence of the capability of the tool, but they can be also considered as benchmarks for developers and users of NICFD tools.

The paper is organized as follows: Section 2.2 recalls the governing equations for an arbitrarily complex fluid at equilibrium condition. Section 2.3 briefly outlines the thermophysical models currently available in SU2. Section 2.4 describes the chosen numerical methods, with particular emphasis on convective, viscous and boundary conditions schemes. Section 2.5 concludes the paper by illustrating an ensemble of test cases for verification purposes.

2.2   Generalized Flow Equations

The present work focuses only on the compressible formulation of the RANS equations,[24] as high Mach number flows are of predominant interest for NICFD applications. The compressible RANS equations are commonly discretized using the conservative formulation

$$\partial_t \mathbf{U} + \nabla \cdot \mathbf{F}^c - \nabla \cdot \mathbf{F}^v = \mathbf{Q} \quad \text{in } \Omega, \ t > 0. \tag{2.1}$$

Equation (2.1) describes how mass, momentum and energy evolve in a control domain. $\mathbf{U}$ symbolizes the vector of conservative variables, i.e., $\mathbf{U} = (\rho, \rho v_1, \rho v_2, \rho v_3, \rho E)^\mathsf{T}$, where ρ is the fluid density, E is the total energy per unit mass, and $\mathbf{v} = (v_1, v_2, v_3) \in \mathbb{R}^3$ is the flow velocity in a Cartesian coordinate system. $\mathbf{F}^c$ and $\mathbf{F}^v$ are the convective and viscous fluxes, and $\mathbf{Q}$ is a generic source term. In this particular model, convective and viscous physical fluxes are written as

$$\mathbf{F}_i^c = \begin{pmatrix} \rho v_i \\ \rho v_i v_1 + p\delta_{i1} \\ \rho v_i v_2 + p\delta_{i2} \\ \rho v_i v_3 + p\delta_{i3} \\ \rho v_i H \end{pmatrix}, \quad \mathbf{F}_i^v = \begin{pmatrix} \cdot \\ \tau_{i1} \\ \tau_{i2} \\ \tau_{i3} \\ v_j \tau_{ij} + k_{\text{tot}} \partial_i T \end{pmatrix}, \quad i = 1, \dots, 3. \tag{2.2}$$

p is the static pressure, T is the temperature, H is the total enthalpy, δ_{ij} is the Kronecker delta function, and the viscous stresses can be compactly written as

$$\tau_{ij} = \mu_{tot}\left(\partial_j v_i + \partial_i v_j - \frac{2}{3}\delta_{ij}\nabla \cdot \mathbf{v} \right). \tag{2.3}$$

According to the Boussinesq hypothesis,[22] μ_{tot} and k_{tot} are respectively the total viscosity and the total thermal conductivity, resulting from the summation of their molecular and turbulent contributions,

$$\mu_{\text{tot}} = \mu_{\text{mol}} + \mu_{\text{tur}}, \quad k_{\text{tot}} = k_{\text{mol}} + k_{\text{tur}}. \tag{2.4}$$

The molecular quantities are evaluated by means of a transport property models. μ_{tur} is given by the selected turbulence model, whereas k_{tur} is simply computed as a linear combination of the turbulent Prandtl number (Pr_{tur}), the specific heat capacity at constant pressure (C_p), and μ_{tur},

$$k_{\text{tur}} = \frac{C_p \mu_{\text{tur}}}{Pr_{\text{tur}}}. \tag{2.5}$$

To date, no experiments have been performed to characterized NICFD turbulent flows; thus, throughout this work, it is assumed that $Pr_{\text{tur}} = 0.7$, as for air.

Finally, To close Eq. (2.1), the system must be supplemented with a thermo-physical model to compute the quantities $p, T, C_p, \mu_{\text{mol}}$ and k_{mol}.

2.3 Thermo-physical library

In case of pure fluids or mixture of given composition, the thermodynamic state is completely defined by two independent quantities. In compressible solvers these two quantities are often the density and the internal energy, e, since they can be directly calculated from the conservative variables:

$$\rho = U_1, \quad e = \frac{U_5}{U_1} - \frac{(U_2 + U_3 + U_4)^2}{2U_1^2} = E - \frac{\|v\|^2}{2}. \tag{2.6}$$

Thus, any generic thermo-physical quantity x can be computed as

$$x = x(\rho, e) = x(\mathbf{U}), \tag{2.7}$$

by specifying any suitable model. More precisely, the code structure of SU2 was re-adapted to compute these quantities using any desired thermo-physical model. Thanks to the work described in this chapter, the thermo-physical library of SU2 currently supports three hard-coded equations of state, i.e. the polytropic ideal gas (PIG), the polytropic Van der Waals (PVdW), and the polytropic Peng-Robinson (PR) models. A detailed description of these models is available in Appendix 2.8. The transport properties can be either specified as fixed values or computed with the Sutherland's law.[21] For the cases in which more complex EoSs and transport properties are needed, SU2 was interfaced to an external and general purpose thermo-physical library[18] that contains all the most accurate models available.

2.4 Numerical Algorithms

This section documents the numerical methods adopted for solving the compressible PDEs with arbitrary fluid models. Particular emphasis is given to the explanation of the the spatial discretization schemes, with focus on the generalized Roe's ARS to evaluate convective fluxes and the AVG formulation for viscous fluxes.

2.4.1 Spatial and Time integration

SU2 has a standard edge-based structure on a dual grid with control volumes constructed using a median-dual vertex-based scheme, as shown in Fig. 2.1. In this framework, the semi-discretized integral form of the RANS equations can be expressed as

$$\int_{\Omega_i} \frac{\partial \mathbf{U}}{\partial t} \, d\Omega + \sum_{j \in \mathcal{N}(i)} (\tilde{\mathbf{F}}^c_{ij} + \tilde{\mathbf{F}}^v_{ij}) \Delta S_{ij} - \mathbf{Q}|\Omega_i| = \int_{\Omega_i} \frac{\partial \mathbf{U}}{\partial t} \, d\Omega + \mathbf{R}_i(\mathbf{U}) = 0, \qquad (2.8)$$

where $\tilde{\mathbf{F}}^c_{ij}$ and $\tilde{\mathbf{F}}^v_{ij}$ are the projected numerical approximations of the convective and viscous fluxes, ΔS_{ij} is the area of the face associated with the edge ij, Ω_i is the control volume associated with the node i, and $\mathcal{N}(i)$ are the neighboring $j - th$ nodes to the node i. The spatial residual vector for the node i, $\mathbf{R}_i$, is obtained by integrating the source term over the control volume and summing up all the projected numerical convective and viscous fluxes associated with all the ij edges. Once the residual vector has been computed,
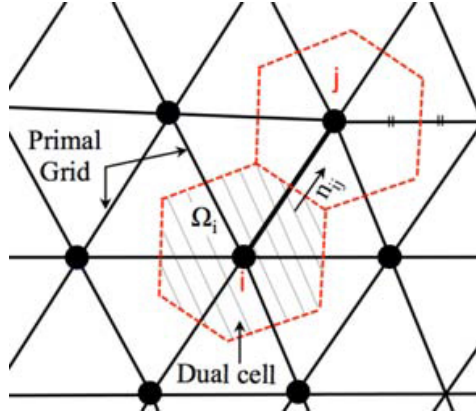
Figure 2.1: Schematic of the primal mesh and the control volume on a dual mesh.

the time integration is performed with an implicit Euler scheme resulting in the following linear system:

$$\left(\frac{|\Omega_i|}{\Delta t^n} \delta_{ij} + \frac{\partial \mathbf{R}_i(\mathbf{U}^n)}{\partial \mathbf{U}^n} \right) \Delta \mathbf{U}^n = -\mathbf{R_i}(\mathbf{U}^n), \qquad (2.9)$$

where $\Delta \mathbf{U}^n := \mathbf{U}^{n+1} - \mathbf{U}^n$ and Δt^n is the (pseudo) time-step which can differ in each cell by using the local time-stepping technique. [25] Equation (2.9) can be solved using different linear solvers implemented in the code framework [17]; in addition, non-linear multi-grid acceleration [26] can be used to speed up the convergence rate of the solver.

2.4.1.1 Convective flux and Jacobian

Several ARSs were recently generalized for arbitrary thermodynamic model. [27] However, it was not found any particular evidence of the superiority of one formulation compared to

the others. Hence, only the generalized Roe's scheme [28] was implemented in this work.

According to Roe's scheme, the convective numerical fluxes can be expressed as

$$\tilde{\mathbf{F}}^c_{ij} = \tilde{\mathbf{F}}^c_{ij}(\mathbf{U}_i, \mathbf{U}_j) = \left(\frac{\mathbf{F}^c_i + \mathbf{F}^c_j}{2}\right) \cdot \mathbf{n}_{ij} - \frac{1}{2}\mathbf{P}|\mathbf{\Lambda}|\mathbf{P}^{-1}(\mathbf{U}_i - \mathbf{U}_j). \tag{2.10}$$

$\mathbf{n}_{ij}$ is the outward unit normal associated with the face between nodes i and j, $\mathbf{P}$ and $\mathbf{P}^{-1}$ are respectively the right and the left eigenvectors of the Jacobian of the projected physical convective flux, constructed using the Roe averaged state, and $|\mathbf{\Lambda}|$ is a diagonal matrix with entries corresponding to the absolute value of the eigenvalues of the same Jacobian. The Roe's average state, $\bar{\mathbf{U}}$, is the value assumed by the conservative variables so that

$$\left(\mathbf{F}^c_i - \mathbf{F}^c_j\right) = \bar{\mathbf{A}}^c \left(\mathbf{U}_i - \mathbf{U}_j\right), \tag{2.11}$$

where $\bar{\mathbf{A}}^c$ is exactly the projected convective physical flux Jacobian computed in the Roe's state [i.e., $\bar{\mathbf{A}}^c = \mathbf{A}^c(\bar{\mathbf{U}})$]. An additional equation, namely,

$$\bar{\chi}(\rho_i - \rho_j) + \bar{\kappa}(\rho_i e_i - \rho_i e_j) = (p_i - p_j), \tag{2.12}$$

arises if the system of equations (2.11) is considered for an arbitrary thermodynamic model, and $\bar{\chi}$ and $\bar{\kappa}$ are the Roe's average values of the two secondary thermodynamics quantities defined as

$$\chi = \left(\frac{\partial P}{\partial \rho}\right)_{\rho e} = \left(\frac{\partial P}{\partial \rho}\right)_e - \frac{e}{\rho}\left(\frac{\partial P}{\partial e}\right)_\rho, \qquad \kappa = \left(\frac{\partial P}{\partial \rho e}\right)_\rho = \frac{1}{\rho}\left(\frac{\partial P}{\partial e}\right)_\rho. \tag{2.13}$$

For a fluid obeying to the PIG law, χ is always equal to zero, and κ assumes a constant value equal to $\gamma - 1$; thus the extra condition (2.12) is satisfied. On the contrary, if a not-ideal model is used, only one equation (2.12) is available to compute the two unknowns quantities $\bar{\chi}$ and $\bar{\kappa}$. Consequently, the Roe-average state remains uniquely defined if and only if a proper closure condition is given. Several approaches [20,29–31] were proposed in the past to solve this problem, and the solution suggested by Vinokur-Montagne' [20] was utilized in this work.

After the Roe's average state has been computed, the computation of the numerical convective flux, Eq. (2.10), can be completed by evaluating the eigenstructure, $\mathbf{P}|\mathbf{\Lambda}|\mathbf{P}^{-1}$, whose a mathematical formulation for an arbitrary thermodynamic model is available in Appendix 2.7. Second-order spatial accuracy is obtained by using a Monotone Upstream-Centered Schemes for Conservation Laws (MUSCL) approach [32] with gradient limitation.

The time integration, Eq. (2.9), requires the computation of the Jacobian of the numerical convective fluxes, $\frac{\partial \tilde{\mathbf{F}}^c_{ij}}{\partial \mathbf{U}}$. In SU2, first order accurate convective Jacobians are computed. Specifically for the Roe's scheme, the Jacobian is calculated by only considering the first term of the right hand side of Eq. (2.10), namely the projected physical flux in i and j. Similarly to the eigenstructure, the expression of the projected Jacobian of physical convective flux for an arbitrary thermodynamic model is reported in Appendix 2.7.

2.4.1.2 Viscous flux and Jacobian

Following the AVG approximation, the numerical viscous flux is evaluated by using Eq. (2.2), in which each flow quantity is computed as average value between the node i and node j. Given x as generic flow quantity used to compute the flux, its average is computed as

$$x_{\mathrm{m}} = \frac{x_{\mathrm{i}} + x_{\mathrm{j}}}{2},$$ (2.14)

thus,

$$\tilde{\mathbf{F}}_{ij}^{v} = \mathbf{F}^{v}(\mathbf{v}_{\mathrm{m}}, \partial_{\mathrm{m}}\mathbf{v}, \partial_{\mathrm{m}}T, \mu_{\mathrm{tot,m}}, k_{\mathrm{tot,m}}).$$ (2.15)

The viscous flux Jacobian is then derived using the *Thin Shear-Layer* approximation. [21]

2.4.2 Boundary Conditions

A new type of boundary condition implementing the approach proposed in a previous work [33] was added to the SU2 suite to automatically detect inflow/outflow boundaries for hyperbolic systems. By means of an eigenvalue analysis, the right number of enforceable unknowns is determined, and the variables that can be specified at the boundary are automatically selected.

The Euler equations for compressible flows, namely the inviscid component of Eq. (2.8),

$$\partial_t \mathbf{U} + \nabla \cdot \mathbf{F}^c = 0,$$ (2.16)

can be linearized along the outward normal direction of a boundary $\mathbf{n}$ as follows

$$\partial_t \mathbf{U} + \mathbf{A}^c \, \partial_{\mathbf{n}} \mathbf{U} = 0.$$ (2.17)

The characteristic variables jump associated to Eq. (2.17) can, therefore, be computed as

$$\delta \mathbf{c} \equiv \mathbf{P}^{-1} \delta \mathbf{U} = \mathbf{P}^{-1} (\mathbf{U}_e - \mathbf{U}_i),$$ (2.18)

where $\delta \mathbf{U} = \mathbf{U}_e - \mathbf{U}_i$ is the difference between the outer conservative vector, $\mathbf{U}_e$, and the solution, $\mathbf{U}_i$, at the i-th boundary node. A characteristic line entering the domain is related to a locally negative eigenvalue, this means that the information carried by the characteristic line travels across the boundary inside the domain. Hence, in case of a negative eigenvalue, the boundary value will be imposed by the corresponding component of the vector $\mathbf{U}_e$. Otherwise, the values at the boundary are specified by means of the values taken from the internal solution $\mathbf{U}_i$. Following this reasoning, the characteristic jump to be imposed at the i-th boundary node can be redefined as

$$\delta \mathbf{c}_i = \psi_i \left(\mathbf{P}^{-1} [\mathbf{U}_e - \mathbf{U}_i] \right),$$ (2.19)

with

$$\psi_i = \psi(\lambda_i) = \begin{cases} 1 & \text{if } \lambda_i < 0 \\ 0 & \text{if } \lambda_i \geq 0. \end{cases}$$ (2.20)

The boundary conservative solution is retrieved as

$$\mathbf{U}_b = \mathbf{U}_i + \mathbf{P}\delta\mathbf{v}_i = \mathbf{U}_i + \mathbf{P}\operatorname{diag}(\vec{\psi})\,\mathbf{P}^{-1}\left[\mathbf{U}_e - \mathbf{U}_i\right], \tag{2.21}$$

and it is finally used to compute the boundary numerical fluxes and respective Jacobians. In this procedure, the eigenvalues, λ_i, and $\mathbf{P}$ and $\mathbf{P}^{-1}$ are evaluated locally at the each boundary node.

2.5 Applications

As opposed to CFD solvers used for aerodynamic applications, no canonical test cases exist for assessing the accuracy of non-ideal compressible flow solvers. Consequently, the results provided by SU2 are first verified against analytical solutions and then compared with the results provided by ANSYS-CFX,[23] which is a commercial CFD software widely adopted for the analysis of NICFD applications.

2.5.1 Rarefaction shock-wave

In thermodynamic conditions close to the critical point, fluids of complex molecules are supposed, by theory, to give rise to non-classical gas dynamic phenomena such as rarefaction shock waves or compression fans. The non-classical region encloses all the possible states of a thermodynamic system, defined as a combination of pressure, temperature and density, that produce a negative value of the *fundamental derivative of gas-dynamics* $\Gamma < 0$.[2] For instance, linear siloxanes, synthetically denoted as MD_nM, are supposed to be endowed with this very particular region. For this family of fluids, cubic equations of state, like the Van der Waals model, admit the onset of the non-classical phenomena mentioned earlier. The fluid considered in this test-case is, therefore, a *MDM* siloxane and its properties are listed in Table 2.1. The geometry of the test-case consists of a simple

p_{cr}	14.152	[bar]
T_{cr}	564.1	[K]
ρ_{cr}	256.82	[kg/m^3]
γ	1.0125	[-]
R^*	35.152	[J/kg/K]
Acentric factor	0.529	[-]

Table 2.1: MDM thermodynamic properties.

square domain containing an edge with a design slope of $\theta = 15.945°$. The fluid flows through the domain from the left to the right boundary. A symmetry condition is applied at the upper border, while at the bottom surface it is prescribed an inviscid wall boundary condition. The results were obtained assuming fluid conditions close to the critical point to show and highlight non-classical phenomena. The inlet conditions imposed to obtain

such a non-classical behavior are summarized in Table 2.2. Inviscid simulations were carried out for this test-case, and the convective fluxes were evaluated using an implicit, second-order Roe numerical scheme modified according to Section 2.4.

p_1	15.0	[bar]
ρ_1	202.9	[kg/m^3]
M_1	1.7	[-]

Table 2.2: Fluid conditions at the inlet.

By assuming gas ideality, i.e. fluid modeled with the PIG model, this problem can be solved analytically through the well-known Prandtl-Meyer expansion function. By means of this relation, it is possible to compute an analytical Mach value of 2.03729 downstream of the fan. Simulation using SU2 with a PIG fluid model predicts an after-expansion Mach number of 2.03728, which is almost identical to the theoretical value. Finally, Fig. 2.2 and 2.3 show the density and the Mach number contours of the expansion fan generated around the edge.

On the contrary, if NICFD effects are taken into account by modeling the fluid with a PVdW EoS, a non-classical rarefaction shock wave occurs. Different structured meshes, with a different level of resolution, were used to simulate this phenomenon. Table 2.3 lists the total number of elements in each mesh. Figure 2.4 depicts the Mach number profiles at $y = 0.4$ along the x axis, for all the different level of space discretization. For grid A, the numerical dissipation causes a smearing out of the rarefaction shock over a wide portion of the domain. Nonetheless, the trend shows that the solution tends to converge to a shock discontinuity by increasing the level of mesh resolution. Although very small differences can still be found, the Mach trends for grid E and F suggest that, eventually, the solution becomes independent from the mesh adopted.

The same conclusion, in terms of adequate level of discretization, can be obtained by looking at the rarefaction shock-wave shown in the density and the Mach number contours for grid A and E in Figs. 2.5, 2.6, 2.7, and 2.8.

Table 2.4, which reports the normalized quantities with respect to the critical values before and after the rarefaction shock further show that, differently from a standard shock-wave, the values of pressure and density drop across the rarefaction shock. The numerical value of the pressure after the rarefaction shock can be compared with its analytical solution. The analytical value of the pressure after the rarefaction shock wave can

mesh tag	A	B	C	D	E	F
N elements	2301	5251	14751	49551	104351	179151

Table 2.3: Number of elements composing each mesh used to discretize the domain and computational time for a single solver iteration.
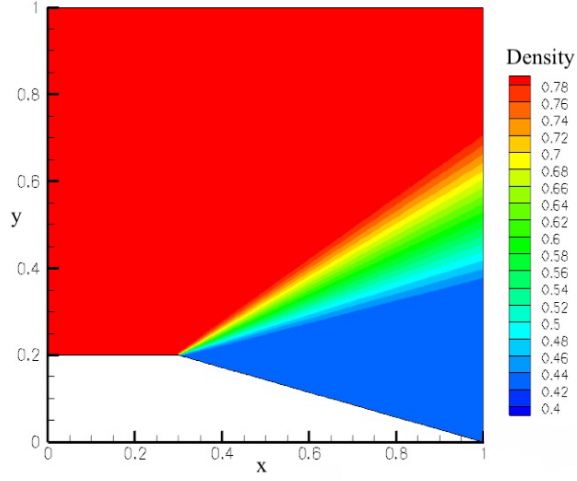
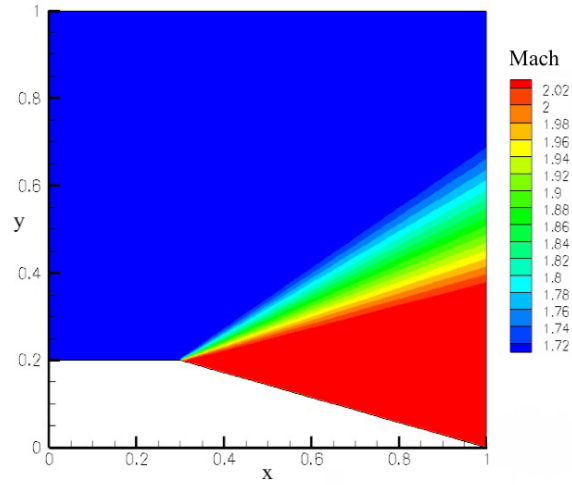Figure 2.2: Density contour computed using the PIG EoS.

Figure 2.3: Mach number contour computed using the PIG EoS.
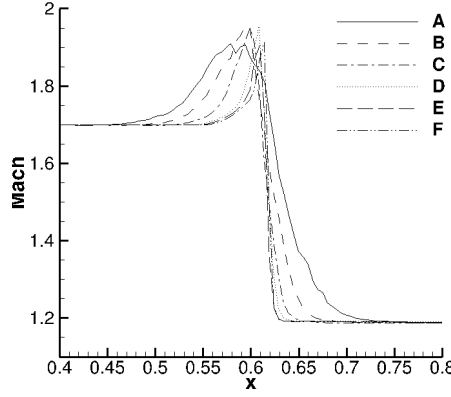
Figure 2.4: Mach profile along $y = 0.4$ for solution computed over different meshes.

	Before (1)	After (2)	
Density	0.790	0.450	[-]
Pressure	1.06	0.930	[-]
Mach	1.70	1.19	[-]
Sound speed	0.504	0.0433	[-]

Table 2.4: Fluid state before and after the rarefaction shock-wave.

be computed using Rankine-Hugoniot condition across the shock:

$$h_2 - h_1 = (e_2 + p_2 v_2) - (e_1 + p_1 v_1) = \frac{1}{2} (p_2 - p_1)(v_2 - v_1). \tag{2.22}$$

By substituting the expression for the internal energy for a Van der Waals gas, the Rankine-Hugoniot condition becomes

$$p_2 = \frac{\dfrac{v_1 - b}{\gamma - 1}\left(p_1 + \dfrac{a}{v_1^2}\right) - \dfrac{a}{v_1} - \dfrac{p_1}{2}(v_2 - v_1) + a\left(1 - \dfrac{1}{\gamma - 1}\right)\dfrac{1}{v_2} + \dfrac{ab}{(\gamma - 1)v_2^2}}{\left(\dfrac{1}{2} + \dfrac{1}{\gamma - 1}\right)v_2 - \left(\dfrac{v_1}{2} + \dfrac{b}{\gamma - 1}\right)}. \tag{2.23}$$

Using Eq.(2.23), it is estimated that the deviation between the numerical value and the theoretical value of p_2 is in the order of 10^{-5}. Finally, the value of the angle β, i.e. the angle between the shock and the direction of the x-axis, is compared against its theoretical value. The analytical relation of β is

$$\beta = \arcsin \sqrt{\frac{p_2 - p_1}{\rho_2 - \rho_1} \frac{\rho_2}{\rho_1} \frac{1}{c_1^2 M_1^2}}, \tag{2.24}$$

Figure 2.5: Density contour computed using the PVdW EoS for grid A

Figure 2.6: Mach number contour computed using the PVdW EoS for grid A

Figure 2.7: Density contour computed using the PVdW EoS for grid E

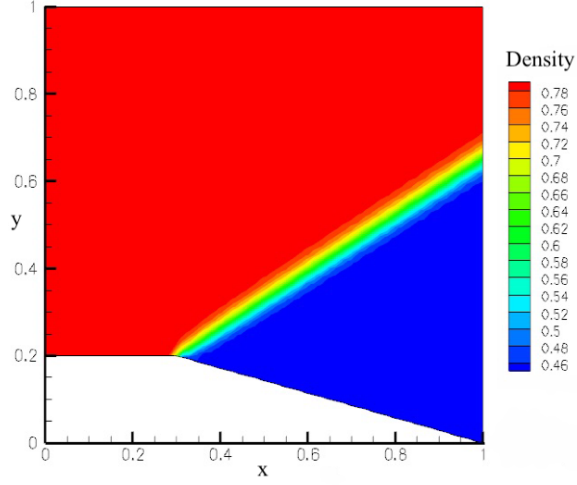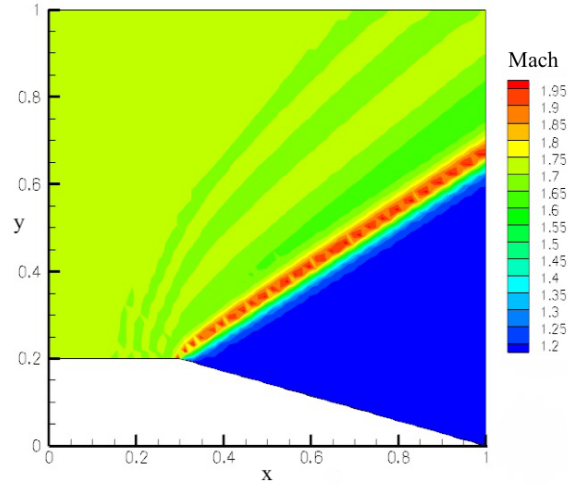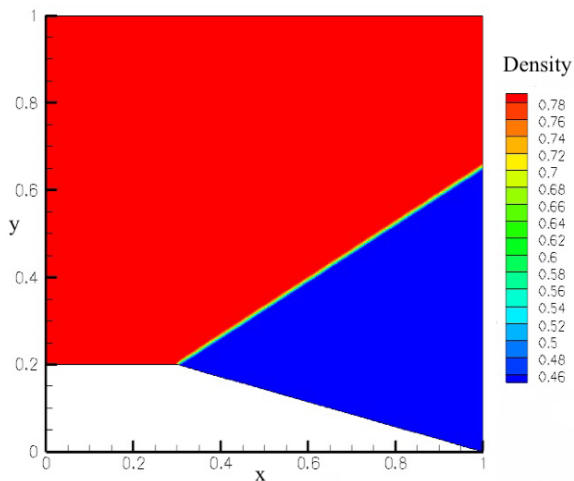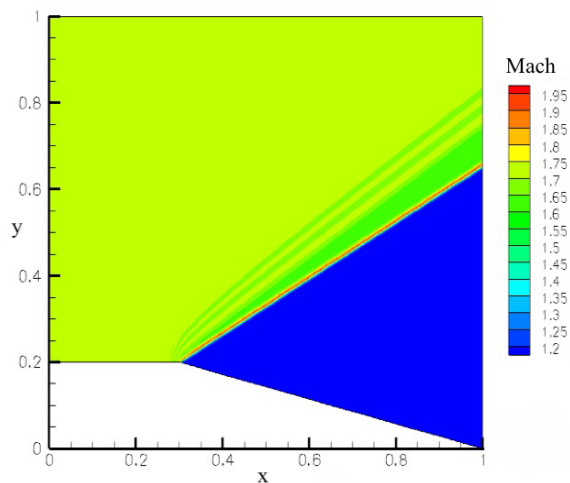Figure 2.8: Mach number contour computed using the PVdW EoS for grid E

$T_{\text{tot,in}}$	530.0	$[^\circ K]$
$p_{\text{tot,in}}$	18.4	[bar]
p_{out}	2.0	[bar]
$\left(\frac{\mu_{\text{tur}}}{\mu_{\text{lam}}}\right)_{\text{in}}$	100.0	[-]
$I_{\text{tur,in}}$	0.05	[-]

Table 2.5: Input parameters for the supersonic nozzle test case.

which depends only on the thermodynamic state of the fluid before and after the shock. In the present case, the analytical value is $\beta = 32.860°$ and the numerical one is $\beta = 32.735°$, with a deviation in the order of 10^{-3}.

2.5.2 Supersonic Nozzle for Laboratory Experiments

The flow-field within a supersonic nozzle is documented in this section. Particularly, the nozzle considered is the test section of the ORCHID facility, a closed-loop research rig currently under construction at Delft University of Technology.[34] The purpose of this rig is to perform fundamental studies on dense organic flows and validate NICFD tools, such as SU2. The test-bench is operated with siloxane MM, here modeled through the multi-parameter Span-Wagner EoS available in FluidProp. Results obtained with SU2 are verified against the one provided by the commercial package Ansys-CFX,[23] which, to the author's knowledge, represents the standard CFD tool for the ORC industry. For the spatial discretization, a second order upwind generalized Roe was used in SU2, while the so called *High Resolution Method* option was selected in CFX. In both solvers, the time integration was performed using an implicit Euler algorithm based on CFL adaptation, and the SST-kω was selected as turbulence model. Table 2.5 summarizes the input parameters for this simulation.

Figures 2.9 and 2.10 display the Mach contour and the pressure distribution along the nozzle mid section respectively. The results fairly well correlate, suggesting that, pending experimental confirmation, SU2 can be adopted for simulating NICFD flows in practical applications.

2.6 Conclusions

In this chapter, the capability of SU2 for simulating non-ideal compressible flows were illustrated and demonstrated through model problems and practical examples. The results showed that SU2 can be successfully used to predict non-classical gas dynamic phenomena such as rarefaction shock waves. The numerical outcomes furthermore indicated that SU2 is highly suited for the analysis of flows in the non-ideal compressible flow regime. Finally, in 2018, Spinelli et al.[35] confirmed the accuracy of SU2 in predicting flows in the NICFD regime against experimental results.
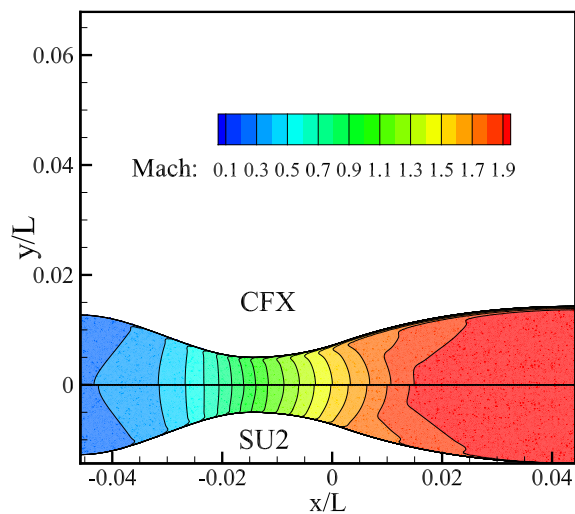
Figure 2.9: Mach contour at the mid section of the nozzle.
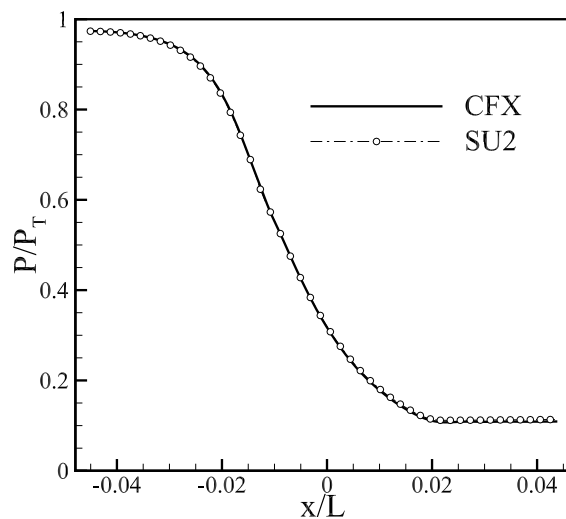
Figure 2.10: Streamwise distribution of the static pressure at the mid section of the nozzle.

2.7   Appendix A: Generalized spatial schemes

The Jacobian of the projected physical convective flux derived with respect to the conservative variables and for an arbitrary fluid model can be written as

$$
\mathbf{A}^c = \begin{bmatrix}
0 & n_1 & n_2 & n_3 & 0 \\
-v_1 q_n + \zeta n_1 & q_n + v_1 n_1 - \kappa n_1 v_1 & v_1 n_2 - \kappa n_1 v_2 & v_1 n_3 - \kappa n_1 v_3 & \kappa n_1 \\
-v_2 q_n + \zeta n_2 & v_2 n_1 - \kappa n_2 v_1 & q_n + v_2 n_2 - \kappa n_2 v_2 & v_2 n_3 - \kappa n_2 v_3 & \kappa n_2 \\
-v_3 q_n + \zeta n_3 & v_3 n_1 - \kappa n_3 v_1 & v_3 n_2 - \kappa n_3 v_2 & q_n + v_3 n_3 - \kappa n_3 v_3 & \kappa n_3 \\
(\zeta - H) q_n & H n_1 - \kappa v_1 q_n & H n_2 - \kappa v_2 q_n & H n_3 - \kappa v_3 q_n & (1 + \kappa) q_n
\end{bmatrix}
\tag{2.25}
$$

where

$$
\zeta = \left(\chi + \frac{1}{2} \kappa |v|^2 \right),
\tag{2.26}
$$

and

$$
q_n = v_1 n_1 + v_2 n_2 + v_3 n_3.
\tag{2.27}
$$

The right and the left eigenvectors of the projected Jacobian $\mathbf{A}^c$ are

$$
\mathbf{P} = \begin{bmatrix}
n_1 & n_2 & n_3 & \frac{1}{2} \frac{\rho}{c} & \frac{1}{2} \frac{\rho}{c} \\
v_1 n_1 & v_1 n_2 - \rho n_3 & v_1 n_3 + \rho n_2 & \sigma_1^+ & \sigma_1^- \\
v_2 n_1 + \rho n_3 & v_2 n_2 & v_2 n_3 - \rho n_1 & \sigma_2^+ & \sigma_2^- \\
v_3 n_1 - \rho n_2 & v_3 n_2 + \rho n_1 & v_3 n_3 & \sigma_3^+ & \sigma_3^- \\
\psi_1 + \rho(v_2 n_3 - v_3 n_2) & \psi_2 + \rho(v_3 n_1 - v_1 n_3) & \psi_3 + \rho(v_1 n_2 - v_2 n_1) & \varphi^+ & \varphi^-
\end{bmatrix},
\tag{2.28}
$$

where

$$
\psi_i = \left(|v|^2 - \frac{\zeta}{\kappa} \right) n_i
\tag{2.29}
$$

$$
\sigma_i^\pm = \frac{1}{2} \left(\frac{\rho}{c} v_i \pm \rho n_i \right)
\tag{2.30}
$$

$$
\varphi^\pm = \frac{1}{2} \left(\frac{\rho}{c} H \pm \rho q_n \right),
\tag{2.31}
$$

and

$$
\mathbf{P}^{-1} = \left[
\begin{array}{ccccc}
\left(1 - \frac{\zeta}{c^2}\right)n_1 - \frac{v_2}{\rho}n_3 + \frac{v_3}{\rho}n_2 & \frac{v_1\kappa}{c^2}n_1 & \frac{v_2\kappa}{c^2}n_1 + \frac{1}{\rho}n_3 & \frac{v_3\kappa}{c^2}n_1 - \frac{1}{\rho}n_2 & -\frac{\kappa}{c^2}n_1 \\
\left(1 - \frac{\zeta}{c^2}\right)n_2 - \frac{v_3}{\rho}n_1 + \frac{v_1}{\rho}n_3 & \frac{v_1\kappa}{c^2}n_2 - \frac{1}{\rho}n_3 & \frac{v_2\kappa}{c^2}n_2 & \frac{v_3\kappa}{c^2}n_2 + \frac{1}{\rho}n_1 & -\frac{\kappa}{c^2}n_2 \\
\left(1 - \frac{\zeta}{c^2}\right)n_3 - \frac{v_1}{\rho}n_2 + \frac{v_2}{\rho}n_1 & \frac{v_1\kappa}{c^2}n_3 + \frac{1}{\rho}n_2 & \frac{v_2\kappa}{c^2}n_3 - \frac{1}{\rho}n_1 & \frac{v_3\kappa}{c^2}n_3 & -\frac{\kappa}{c^2}n_3 \\
\frac{\zeta}{\rho c} - \frac{q_n}{\rho} & -\frac{v_1\kappa}{\rho c} + \frac{1}{\rho}n_1 & -\frac{v_2\kappa}{\rho c} + \frac{1}{\rho}n_2 & -\frac{v_3\kappa}{\rho c} + \frac{1}{\rho}n_3 & \frac{\kappa}{\rho c} \\
\frac{\zeta}{\rho c} + \frac{q_n}{\rho} & -\frac{v_1\kappa}{\rho c} - \frac{1}{\rho}n_1 & -\frac{v_2\kappa}{\rho c} - \frac{1}{\rho}n_2 & -\frac{v_3\kappa}{\rho c} - \frac{1}{\rho}n_3 & \frac{\kappa}{\rho c}
\end{array}
\right]
\tag{2.32}
$$

The characteristic variables with respect to the conservative variables are computed as

$$
\delta\mathbf{c} = \mathbf{P}^{-1}\delta\mathbf{U}
\begin{pmatrix}
\delta\rho - \frac{\delta P}{c^2} \\
n_1 v_3 - n_3 v_0 \\
n_2 v_1 - n_1 v_2 \\
\frac{\delta P}{c\rho} + q_n \\
\frac{\delta P}{c\rho} - q_n
\end{pmatrix},
\tag{2.33}
$$

and the eigenvalues as

$$
\mathbf{\Lambda} = \left[
\begin{array}{ccccc}
q_n & 0 & 0 & 0 & 0 \\
0 & q_n & 0 & 0 & 0 \\
0 & 0 & q_n & 0 & 0 \\
0 & 0 & 0 & q_n + c & 0 \\
0 & 0 & 0 & 0 & q_n - c
\end{array}
\right].
\tag{2.34}
$$

2.8   Appendix B: thermodynamic models

2.8.1   Polytropic Perfect gas

The set of equations describing the volumetric and caloric behavior of a polytropic ideal gas (PIG) can be written as

$$
\begin{cases}
p(T, v) = \dfrac{RT}{v} \\
e(T, v) = e(T) = e_{\text{ref}} + c_v (T - T_{\text{ref}}) \\
s(T, v) = s_{\text{ref}} + c_v \ln \frac{T}{T_{\text{ref}}} + R \ln \frac{v}{v_{\text{ref}}} \\
c_v = \frac{1}{\gamma - 1} R
\end{cases}
\tag{2.35}
$$

Where $\gamma = \frac{C_p}{C_v}$ is the specific heat ratio. Reference values for energy and entropy are defined as

$$
\begin{cases}
e_{\text{ref}} = c_v T_{\text{ref}} \\
s_{\text{ref}} = -c_v \ln T_{\text{ref}} + R \ln v_{\text{ref}}
\end{cases}
\tag{2.36}
$$

T_{ref} and v_{ref} together with p_{ref} are defined by the user to make the variables dimensionless. This approach allow to simplify the implementation of the equations of entropy and energy

$$
\begin{cases}
e\,(T,v) = c_v T \\
s\,(T,v) = c_v \ln T + R \ln v
\end{cases}
\tag{2.37}
$$

Thermodynamic Derivatives

Four secondary properties are needed for computing the numerical schemes. For a PIG gas they can be written as

$$
\left(\frac{\partial p}{\partial e}\right)_\rho = (\gamma - 1) \cdot \rho
\tag{2.38}
$$

$$
\left(\frac{\partial p}{\partial \rho}\right)_e = (\gamma - 1) \cdot e
\tag{2.39}
$$

$$
\left(\frac{\partial T}{\partial e}\right)_\rho = \frac{(\gamma - 1)}{R}
\tag{2.40}
$$

$$
\left(\frac{\partial T}{\partial \rho}\right)_e = 0.
\tag{2.41}
$$

and speed of sound can be more generally recovered as a combination of the first two properties as

$$
c^2 = \left(\frac{\partial p}{\partial \rho}\right)_e + \frac{p}{\rho^2}\left(\frac{\partial p}{\partial e}\right)_\rho
\tag{2.42}
$$

2.8.2 PolytropicVan der Waals

The equations of a polytropic Van der Waals gas (PVdW) model are

$$
\begin{cases}
p\,(T,v) = \dfrac{RT}{v-b} - \dfrac{a}{v^2} \\[2mm]
e\,(T,v) = c_v T - \dfrac{a}{v} \\[2mm]
s\,(T,v) = c_v \ln T + R \ln (v - b)
\end{cases}
\tag{2.43}
$$

43

where a represents a measure of the intensity of the inter-molecular attractive force while b is the covolume.

Both these two values are supposed to be constant and depend from the chemical composition of the gas

$$\begin{cases} a = \frac{27}{64} \frac{R^2 T_{cr}^2}{P_{cr}} \\ b = \frac{1}{8} \frac{R T_{cr}}{P_{cr}} \end{cases} \tag{2.44}$$

T_{cr} and P_{cr} are the critical temperature and pressure respectively. Notice that for consistency the equations of the energy and entropy use the same e_{ref} and s_{ref}, defined in Eq. 2.36.

Thermodynamic Derivatives

For a Van der Waals gas the secondary properties are given by:

$$\left(\frac{\partial p}{\partial e} \right)_\rho = \frac{\rho (\gamma - 1)}{1 - \rho b} \tag{2.45}$$

$$\left(\frac{\partial p}{\partial \rho} \right)_e = \frac{\left(e + 2\rho a - \rho^2 ab \right)}{\rho (1 - \rho b)} \left(\frac{\partial p}{\partial e} \right)_\rho - 2\rho a \tag{2.46}$$

$$\left(\frac{\partial T}{\partial e} \right)_\rho = \frac{(\gamma - 1)}{R} \tag{2.47}$$

$$\left(\frac{\partial T}{\partial \rho} \right)_e = \frac{1}{a} \left(\frac{\partial T}{\partial e} \right)_\rho \tag{2.48}$$

Finally the speed of sound is computing using Eq. 2.42.

2.8.3 Polytropic Peng-Robinson

Peng-Robinson proposed their non-ideal gas model in 1976. Basically, the model is a modified SRK ($Soave-Redlich-Kwong$) equation of state which improves the prediction of liquid density values, vapor pressures, and equilibrium ratios. The polytropic Peng Robinson model can be conveniently written as

$$\begin{cases} p(T, v) = \dfrac{RT}{v - b} - \dfrac{a\alpha^2(T)}{v^2 + 2bv - b^2} \\ e(T, v) = c_v T - \dfrac{a\alpha(T)(k+1)}{b\sqrt{2}} \tanh^{-1} \dfrac{b\sqrt{2}}{v + b} \\ s(T, v) = c_v lnT + R \ln(v - b) - \dfrac{a\alpha(T)k}{b\sqrt{2TT_{cr}}} \tanh^{-1} \dfrac{b\sqrt{2}}{v + b}, \end{cases} \tag{2.49}$$

whereby $\alpha(T)$ represents the inter-molecular attraction force, which depends on the temperature T, while a and b are usually treated as temperature independent. Their values are calculated as follows

$$
\begin{cases}
a = 0.45724 \frac{(RT_{\text{cr}})^2}{P_{\text{cr}}} \\
b = 0.0778 \frac{RT_{\text{cr}}}{P_{\text{cr}}} \\
\alpha(T, \omega) = \left[1 + k \left(1 - \sqrt{\frac{T}{T_{\text{cr}}}} \right) \right] \\
k = \begin{cases} 0.37464 + 1.54226\omega - 0.26992\omega^2 & \omega \leq 0.49 \\ 0.379642 + 1.48503\omega - 0.164423\omega^2 + 0.016666\omega^3 & \omega > 0.49 \end{cases}
\end{cases}
\tag{2.50}
$$

Again for matters of consistency the energy and the entropy equations use the same e_{ref} and s_{ref}, defined in Eq. 2.36.

Thermodynamic Derivatives

For a Peng-Robinson gas the secondary properties are given by

$$
\left(\frac{\partial p}{\partial e} \right)_\rho = \frac{\left(\frac{\partial p}{\partial T} \right)_\rho}{\left(\frac{\partial e}{\partial T} \right)_\rho}
\tag{2.51}
$$

$$
\left(\frac{\partial p}{\partial \rho} \right)_e = \left(\frac{\partial p}{\partial \rho} \right)_T - \left(\frac{\partial p}{\partial e} \right)_\rho \left(\frac{\partial e}{\partial \rho} \right)_T
\tag{2.52}
$$

$$
\left(\frac{\partial T}{\partial e} \right)_\rho = \frac{1}{\left(\frac{\partial e}{\partial T} \right)_\rho}
\tag{2.53}
$$

$$
\left(\frac{\partial T}{\partial \rho} \right)_e = \left(\frac{\partial T}{\partial \rho} \right)_p - \left(\frac{\partial T}{\partial p} \right)_\rho \frac{\left(\frac{\partial e}{\partial T} \right)_p}{\left(\frac{\partial \rho}{\partial T} \right)_p}
\tag{2.54}
$$

where

$$
\left(\frac{\partial p}{\partial T} \right)_\rho = \frac{R}{(v - b)} - \frac{2a\alpha\alpha'}{[v(v + b) + b(v - b)]}, \qquad \alpha' = \frac{d\alpha}{dT}
\tag{2.55}
$$

$$\left(\frac{\partial e}{\partial T}\right)_\rho = \frac{R}{\gamma - 1} - \frac{a}{b\sqrt{2}}\left[2\alpha\alpha' + k\alpha'\sqrt{\frac{T}{T_c}} + \frac{1}{2}k\alpha\,(TT_C)^{-\frac{1}{2}}\right]f\,(v) \tag{2.56}$$

$$\left(\frac{\partial p}{\partial \rho}\right)_T = -\frac{1}{\rho^2}\left(\frac{\partial p}{\partial v}\right)_T = -\left(-\frac{RT}{(v-b)^2} + \frac{2a\alpha^2\,(v+b)}{[v\,(v+b) + b\,(v-b)]^2}\right)v^2 \tag{2.57}$$

$$\left(\frac{\partial e}{\partial \rho}\right)_T = \frac{\partial}{\partial \rho}\left(-\frac{a\alpha\,(T)}{b\sqrt{2}}\left[\alpha\,(T) + k\sqrt{\frac{T}{T_c}}\right]\tanh^{-1}\frac{b\sqrt{2}}{v+b}\right) = -\frac{a\alpha\,(T)}{b\sqrt{2}}\left[\alpha\,(T) + k\sqrt{\frac{T}{T_c}}\right]\frac{b\sqrt{2}}{1+2\rho b - \rho^2 b^2} \tag{2.58}$$

$$\left(\frac{\partial \rho}{\partial T}\right)_p = -\rho^2\left(\frac{\partial v}{\partial T}\right)_p \tag{2.59}$$

$$\left(\frac{\partial T}{\partial \rho}\right)_p = \frac{1}{\left(\dfrac{\partial \rho}{\partial T}\right)_p} \tag{2.60}$$

$$\left(\frac{\partial v}{\partial T}\right)_p = -\left[\left(\frac{\partial p}{\partial v}\right)_T\left(\frac{\partial T}{\partial p}\right)_v\right]^{-1} = -\left(\frac{\partial p}{\partial v}\right)_T^{-1}\left(\frac{\partial p}{\partial T}\right)_v \tag{2.61}$$

$$\left(\frac{\partial e}{\partial T}\right)_p = \left(\frac{\partial h}{\partial T}\right)_p - p\left(\frac{\partial v}{\partial T}\right)_p \tag{2.62}$$

$$\left(\frac{\partial h}{\partial T}\right)_p = \left(\frac{\partial e}{\partial T}\right)_v + T\left(\frac{\partial p}{\partial T}\right)_v\left(\frac{\partial v}{\partial T}\right)_p \tag{2.63}$$

Finally the speed of sound is computed using the general expression in Eq. 2.42.

References

[1] Nicfd 2016: 1st international seminar on non-ideal compressible-fluid dynamics for propulsion and power.

[2] Colonna, P., and Guardone, A., 2006. "Molecular interpretation of nonclassical gas dynamics of dense vapors under the van der Waals model". *Physics of Fluids,* **18**, pp. 056101–14.

[3] Colonna, P., Guardone, A., and Nannan, N. R., 2007. "Siloxanes: a new class of candidate Bethe-Zeldovich-Thompson fluids". *Physics of Fluids,* **19**.

[4] Nannan, N., Guardone, A., and Colonna, P., 2014. "Critical point anomalies include expansion shock waves". *Physics of Fluids,* **26**, pp. 021701–7.

[5] Drescher, U., and Bruggeman, D., 2007. "Fluid selection for the Organic Rankine Cycle (ORC) in biomass power and heat plants". *Applied Thermal Engineering,* **27**(1), pp. 223–228.

[6] Lang, W., Colonna, P., and Almbauer, R., 2013. "Assessment of waste heat recovery from a heavy-duty truck engine by means of an orc turbogenerator". *Journal of Engineering for Gas Turbines and Power,* **135**(4), p. 042313.

[7] Quoilin, S., Broek, M. V. D., Declaye, S., Dewallef, P., and Lemort, V., 2013. "Techno-economic survey of Organic Rankine Cycle (ORC) systems". *Renewable and Sustainable Energy Reviews,* **22**(0), pp. 168–186.

[8] Casati, E., Vitale, S., Pini, M., Persico, G., and Colonna, P., 2014. "Centrifugal Turbines for Mini-Organic Rankine Cycle Power Systems". *Journal of Engineering for Gas Turbines and Power,* **136**, pp. 122607–1–11.

[9] Dostal, V., Hejzlar, P., and Driscoll, M., 283-301. "The supercritical carbon dioxide power cycle: comparison to other advanced power cycles". *Nuclear technology,* **154**(3).

[10] Lettieri, C., Baltadjiev, N., Casey, M., and Spakovszky, Z., 2014. "Low-Flow-Coefficient Centrifugal Compressor Design for Supercritical CO_2". *Journal of Turbomachinery,* **136**, pp. 081008–1–9.

[11] Lettieri, C., Yang, D., and Spakovszky, Z., 2014. "An Investigation of Condensation Effects in Supercritical Carbon Dioxide Compressors". In The 4th International Symposium - Supercritical CO_2 Power Cycles.

[12] Subramaniam, B., Rajewski, R., and Snavely, K., 1997. "Pharmaceutical processing with supercritical carbon dioxide". *Journal of Pharmaceutical Sciences,* **86**(8).

[13] Bober, W., and Chow, W., 1990. "Nonideal Isentropic Gas Flow Through Converging-Diverging Nozzles". *Journal of Fluids Engineering,* **112**(4), pp. 455–460.

[14] Guardone, A., Spinelli, A., and Dossena, V., 2013. "Influence of Molecular Complexity on Nozzle Design for an Organic Vapor Wind Tunnel". *ASME Journal of Engineering for Gas Turbines and Power,* **135**.

[15] Perullo, C. A., Mavris, D. N., and Fonseca, E., 2013. "An integrated assessment of an organic rankine cycle concept for use in onboard aircraft power generation". In ASME Turbo Expo 2013: Turbine Technical Conference and Exposition, American Society of Mechanical Engineers, pp. V002T01A028–V002T01A028.

[16] Head, A., Iyer, S., de Servi, C., and Pini, M., 2017. "Towards the validation of a cfd solver for non-ideal compressible flows". *Energy Procedia,* **129**, pp. 240–247.

[17] Economon, T. D., Palacios, F., Copeland, S. R., Lukaczyk, T. W., and Alonso, J. J., 2015. "Su2: an open-source suite for multiphysics simulation and design". *AIAA Journal*.

[18] Colonna, P., and van der Stelt, T., 2005. FluidProp: A program for the estimation of thermo-physical properties of fluids. Tech. rep.

[19] Montagne, J., Yee, H., and Vinokur, M., 1989. "Comparative Study of High-Resolution Shock-CapturingSchemes for a Real Gas". *AIAA Journal,* **27**(10), pp. 1332–1346.

[20] Montagne, J., and Vinokur, M., 1990. "Generalized flux-vector splitting and Roe average for an equilibrium real gas". *Journal of Computational Physics,* **89**(2), pp. 276–300.

[21] Blazek, J., 2005. *Computational Fluid Dynamics: Principles and Applications*. Elsevier, Oxford.

[22] Wilcox, D., 1998. *Turbulence Modeling for CFD*. 2nd Ed., DCW Industries, Inc.

[23] ANSYS Inc. Academic Research, R. ., 2012. *CFX*.

[24] Landau, L., and Lifshitz, E., 1993. *Fluid Mechanics (2nd Edition)*. Pergamon Press.

[25] Palacios, F., Alonso, J., Duraisamy, K., Colonno, M., Hicken, J., Aranake, A., Campos, A., Copeland, S., Economon, T., Lonkar, A., et al., 2013. "Stanford university unstructured (su 2): an open-source integrated computational environment for multi-physics simulation and design". In 51st AIAA Aerospace Sciences Meeting Including the New Horizons Forum and Aerospace Exposition, p. 287.

[26] Borzı, A., 2005. Introduction to multigrid methods. Tech. rep., Technical report, Institut für Mathematik und Wissenschaftliches Rechnen, Karl-Franzens-Universität Graz, Austria.

[27] Rinaldi, E., Pecnik, R., and Colonna, P., 2014. "Exact Jacobians for implicit Navier-Stokes simulations of equlibrium real gas flows". *Journal of Computational Physics,* **270**, pp. 459–477.

[28] Roe, P. L., 1981. "Approximate riemann solvers, parameter vectors, and difference schemes". *Journal of Computational Physics,* **43**(2), pp. 357–372.

[29] Guardone, A., and Vigevano, L., 2002. "Roe Linearization for the van der Waals Gas". *Journal of Computational Physics,* **175**(10), pp. 50–78.

[30] Cinnella, P., 2006. "Roe-type schemes for dense gas flow computations". *Computers & Fluids,* **35**(10), pp. 1264–1281.

[31] Glaister, P., 1988. "An approximate linearised riemann solver for the Euler equations for real gases". *Journal of Computational Physics,* **74**(2), pp. 382–408.

[32] van Leer, B., 1979. "Towards the ultimate conservative difference scheme V. a second-order sequel to Godunov's method". *Journal of Computational Physics,* **32**(1), July, pp. 101–136.

[33] Guardone, A., Isola, D., and Quaranta, G., 2011. "Arbitrary Lagrangian Eulerian formulation for two-dimensional flows using dynamic meshes with edge swapping". *Journal of Computational Physics,* **230**(20), pp. 7706–7722.

[34] Head, A. J., De Servi, C., Casati, E., Pini, M., and Colonna, P., 2016. "Preliminary design of the orchid: A facility for studying non-ideal compressible fluid dynamics and testing orc expanders". In ASME Turbo Expo 2016: Turbomachinery Technical Conference and Exposition, American Society of Mechanical Engineers, pp. V003T25A001–V003T25A001.

[35] Spinelli, A., Cammi, G., Gallarini, S., Zocca, M., Cozzi, F., Gaetani, P., Dossena, V., and Guardone, A., 2018. "Experimental evidence of non-ideal compressible effects in expanding flow of a high molecular complexity vapor". *Experiments in Fluids,* **59**(8), Jul, p. 126.

3

Extension and application of a RANS direct and adjoint solver for the analysis and design of NICFD turbomachinery

Abstract   *Non-Ideal Compressible Fluid-Dynamics (NICFD) has recently been established as a sector of fluid mechanics dealing with the flows of dense vapors, supercritical fluids, and two-phase fluids, whose properties significantly depart from those of the ideal gas. The flow through an Organic Rankine Cycle turbine is an exemplary application, as stators often operate in the supersonic and transonic regime, and are affected by NICFD effects. Other applications are turbomachinery using supercritical CO_2 as working fluid or other fluids typical of the oil and gas industry, and components of air conditioning and refrigeration systems. Due to the comparably lower level of experience in the design of this fluid machinery, and the lack of experimental information on NICFD flows, the design of the main components of these processes (i.e., turbomachinery and nozzles) may benefit from adjoint-based automated fluid-dynamic shape optimization. Hence, this work is related to the development and testing of a fully-turbulent adjoint method capable of treating NICFD flows. The method was implemented within the SU2 open-source software infrastructure. The adjoint solver was obtained by linearizing the discretized flow equations and the fluid thermodynamic models by means of advanced Automatic Differentiation techniques. The new adjoint solver was tested on exemplary turbomachinery cases. Results demonstrate the method effectiveness in improving simulated fluid-dynamic performance, and underline the importance of accurately modeling non-ideal thermodynamic and viscous effects when optimizing internal flows characterized by NICFD phenomena.*

3.1   Introduction

Non-Ideal Compressible Fluid-Dynamics (NICFD) is a new branch of fluid-mechanics[1] concerned with the flows of dense vapors, supercritical fluids, and two-phase fluids, in cases in which the ideal gas law does not apply. In these flows, the isentropic variation of the speed of sound with density is different if compared to the flow of an ideal gas;[2] thus, the flow field is bound to be quantitatively[3] or even qualitatively different.[4]

NICFD internal flows occur in numerous heterogeneous industrial processes. The supersonic and transonic flow through an Organic Rankine Cycle (ORC) turbine nozzle is an example.[5] Another case in the energy sector is the transonic flow occurring in the compressor of supercritical CO_2 power plant,[6] or of CO_2 capture and sequestration plants.[7] Similarly, flows of fluids in dense-vapor or two-phase conditions are relevant in throttling valves, compressors, and ejectors of refrigeration and heat pump systems.[8,9] Turbomachinery and nozzles partly operating in the NICFD regime are common in the oil and gas industry,[10–12] and these unconventional flows can also occur in pipelines for fuel distribution.[13] Dense vapors made of heavy molecules can be used in supersonic wind tunnels instead of air to achieve higher Reynolds numbers, which can be varied almost independently from the Mach number.[14] Finally, supercritical CO_2 nozzle flows are used in the pharmaceutical industry to extract chemicals.[15]

The technical and economic viability of these processes can be greatly enhanced if the performance of fluid flow components is improved. Fluid-dynamic shape optimization (FSO) arguably allows a quantum step progress in this respect.[16] FSO has played

a crucial role in the development of more conventional technologies,[17–19] but it can be even more important in the case of technologies entailing NICFD flows, where design experience and experimental information are much more limited. Hence, concerted research efforts have been recently devoted to develop FSO techniques for NICFD applications, in particular for nozzles and turbomachinery blades.[20–24]

The FSO of nozzles and of turbomachinery blades can be performed with either gradient-free[25] or gradient-based[26] methods. Gradient-free algorithms only demand the evaluation of the objective function (e.g., genetic algorithms), and they are often coupled with surrogate models to reduce the computational cost.[19,27,28] Nevertheless, the number of function evaluations necessary to converge to an optimum solution are comparatively large, and only few design variables can be concurrently optimized.[29] Instead, gradient-based methods can reach an optimal solution in far fewer iterations. However, these techniques require not only the computation of the objective function, but also the expensive estimation of its gradient with respect to the design variables. The use of the adjoint method makes the computational cost of the gradient evaluation of the same order of magnitude of that of the objective function, regardless of the number of design variables.[30] Thus, if the problem involves a large number of design variables and the estimation of the objective function is computationally expensive, adjoint-based methods are the only viable technique.

The already difficult task of linearizing the flow equations[31] becomes even more challenging in the context of NICFD, where complex thermo-physical fluid models must be adopted to accurately estimate fluid properties, raising the need of specialized numerical methods.[32,33]. Despite that, recent work on the subject[21,22] has demonstrated the potential of adjoint-based method for the FSO of NICFD flows occurring in ORC turbine cascades. However, this approach was limited to inviscid flows, restricting the adjoint applicability to some supersonic flow cases where viscous effects are not of concern.

In this work the adjoint method was extended to fully-turbulent NICFD flows; thus, the approach can be applied, without restrictions, to the FSO of any NICFD application. The adjoint solver was obtained by linearizing the discretized flow equations by means of Automatic Differentiation (AD). Nevertheless, the use of AD, if performed by differentiating individual subroutines like in the work of *Pini et al.*,[21] still requires additional error-prone steps whenever new numerical schemes or fluid models are added to the source-code. On the contrary, in this work a holistic linearization approach was adopted, whereby AD is applied in a black-box manner to the entire source code. This is accomplished with the help of modern meta-programming features[34] in combination with a reformulation of the state constraint into a fixed-point problem.[35] The result is a fast and accurate discrete adjoint solver that includes all the flow solver features, such as arbitrary complex equations of state and turbulence models.

The new RANS adjoint solver was developed by leveraging on the open-source software infrastructure of SU2,[36] a platform conceived for solving multi-physics PDE and PDE-constrained optimization problems using general unstructured meshes. The SU2 flow solver, previously extended to model NICFD flows,[37] was adapted to simulate turbomachinery flows.

The developed adjoint solver was naturally integrated into the automatic constrained

FSO framework already available in SU2. The optimizer uses the objective function and constrain sensitivities to accordingly re-shape the target geometry by moving the control points of a free-form deformation box. To avoid re-meshing at each design cycle, a linear-elasticity method is applied to propagate the surface perturbation to the entire mesh.

The capability of the new design tool was tested on two exemplary cases: a super-sonic and a transonic ORC turbine cascade. The results demonstrate the importance of accurately modeling non-ideal thermodynamic and viscous effects for adjoint-based FSO applied to NICFD applications.

This chapter is organized as follows. Section 3.2 describes the SU2 flow solver and its extension to accurately simulate and analyze turbomachinery NICFD flows. Section 3.3 focuses on the derivation of the discrete adjoint solver, also taking into account the surface and volume mesh deformation. Section 3.4 reports the application of the new adjoint solver to the re-designing of two typical ORC blades, and discusses the different results obtained using a turbulent or an inviscid approach. Finally, in Section 3.5 the more accurate NICFD approach is compared with the more standard ideal-gas based method. Concluding remarks and future work are briefly treated in Section 3.6.

3.2 Flow Solver

This section reports the modification needed to extend the SU2 RANS solver, described in Section 2.2 and 2.4, to accurately simulate two-dimensional flows in NICFD turbomachinery applications. Specifically, ad-hoc inflow and outflow boundary conditions were implemented. Furthermore, this section also documents the algorithm used to compute average flow quantities at the inflow and outflow boundaries. This average state is not only used to linearized the flow equations at the boundaries, but also to compute some performance parameters which are then adopted as objective functions for the discrete adjoint solver.

3.2.1 Non-reflecting boundary conditions

Non-reflecting boundary conditions (NRBC) were implemented according to the method proposed by Giles. [38] Any incoming boundary characteristic δc_i^{BC} can be seen as a contribution of two different components:

$$\delta c_i^{BC} = \delta \hat{c}_i + \delta \bar{c}_i. \tag{3.1}$$

The harmonic boundary solution, $\delta \hat{\mathbf{c}}$, is calculated using the 2D non-reflecting theory, and this is the component that prevents the formation of non-physical boundary reflections. The average component, $\delta \bar{\mathbf{c}}$ (also known as zero-th fourier mode), is computed according to the standard 1D characteristic-based approach, and allows the user to specify quantities at the boundary.

The incoming harmonic characteristic at the outflow can be computed as

$$\delta\hat{c}_4 = \text{Re}\left[\sum_{-\infty,m\neq0}^{\infty}\left(\frac{1}{S}\int_0^S\left(\frac{2\bar{v}_\text{n}}{\alpha+\bar{v}_\text{t}}\delta\dot{c}_2 - \frac{\alpha+\bar{v}_\text{t}}{\alpha-\bar{v}_\text{t}}\delta\dot{c}_3\right)e^{-i\frac{2\pi m}{S}y}dy\right)e^{i\frac{2\pi y}{S}m}\right] - \delta\dot{c}_4, \qquad (3.2)$$

while the incoming harmonic characteristic at the inflow can be calculated as

$$\begin{pmatrix}\delta\hat{c}_1\\\delta\hat{c}_2\\\delta\hat{c}_3\end{pmatrix} = \begin{pmatrix}-\delta\dot{c}_1\\\text{Re}\left[\sum_{-\infty,m\neq0}^{\infty}\left(\frac{1}{S}\int_0^S -\frac{\alpha+\bar{v}_\text{t}}{\bar{a}+\bar{v}_\text{n}}\delta\dot{c}_4 e^{-i\frac{2\pi m}{S}y}dy\right)e^{i\frac{2\pi y}{S}m}\right] - \delta\dot{c}_2\\\text{Re}\left[\sum_{-\infty,m\neq0}^{\infty}\left(\frac{1}{S}\int_0^S\left(\frac{\alpha+\bar{v}_\text{t}}{\bar{a}+\bar{v}_\text{n}}\right)^2\delta\dot{c}_4 e^{-i\frac{2\pi m}{S}y}dy\right)e^{i\frac{2\pi y}{S}m}\right] - \delta\dot{c}_3\end{pmatrix}. \qquad (3.3)$$

$\delta\dot{c}_i$ is the local characteristic value computed with the difference between the primitive local values (at each grid node) and the average boundary values:

$$\begin{pmatrix}\delta\dot{c}_1\\\delta\dot{c}_2\\\delta\dot{c}_3\\\delta\dot{c}_4\end{pmatrix} = \begin{bmatrix}-\bar{a}^2 & 0 & 0 & 1\\0 & 0 & \bar{\rho}\bar{a} & 0\\0 & \bar{\rho}\bar{a} & 0 & 1\\0 & -\bar{\rho}\bar{a} & 0 & 1\end{bmatrix}\begin{pmatrix}\rho-\bar{\rho}\\v_\text{n}-\bar{v}_\text{n}\\v_\text{t}-\bar{v}_\text{t}\\p-\bar{p}\end{pmatrix}, \qquad (3.4)$$

and α is a parameter calculated as

$$\alpha = \begin{cases}sign(m)i\sqrt{\bar{a}^2 - (\bar{v}_\text{n}^2 + \bar{v}_\text{t}^2)}, & \bar{a}^2 > (\bar{v}_\text{n}^2 + \bar{v}_\text{t}^2)\\\text{or,}\\sign(\bar{v}_\text{t})\sqrt{(\bar{v}_\text{n}^2 + \bar{v}_\text{t}^2) - \bar{a}^2}, & \bar{a}^2 < (\bar{v}_\text{n}^2 + \bar{v}_\text{t}^2).\end{cases} \qquad (3.5)$$

S is the pitch of the simulated cascade, m is the frequency of the domain, and y is the spatial coordinate along the tangential direction. Finally, if the flow at the boundary is supersonic, $\delta\hat{\mathbf{c}}$ is computed using only the local characteristic variables without the use of the Fourier transformation.[38] The average characteristic change at the outflow boundary is determined in order to achieve the user-specified exit pressure. Since the variation of the incoming characteristic at the outflow with respect to the pressure is calculated as

$$\frac{\partial c_4}{\partial p} = 2, \qquad (3.6)$$

the average change on the fourth characteristic can be computed as

$$\delta\bar{c}_4 = 2(p_\text{u} - \bar{p}). \qquad (3.7)$$

A different approach has to be followed to compute the inflow $\delta\bar{c}_i$, because the computed average entropy, stagnation enthalpy, and flow direction differ from the user-specified values if NRBCs are imposed at the inlet.[39] To ensure that a correct solution is found,

the average incoming characteristics are computed by driving the difference between the computed average quantities and the user-specified quantities,

$$R_1 = \bar{s} - s_u,$$
$$R_2 = \bar{v}_t - \bar{v}_n \tan(\beta_u), \tag{3.8}$$
$$R_3 = \bar{h}_{tot} - h_{tot,u},$$

to zero at each time step. The resulted non-linear system,

$$\begin{pmatrix} R_1 \\ R_2 \\ R_3 \end{pmatrix} + \frac{\partial(R_1, R_2, R_3)}{\partial(c_1, c_2, c_3)} \begin{pmatrix} \delta\bar{c}_1 \\ \delta\bar{c}_2 \\ \delta\bar{c}_3 \end{pmatrix} = 0, \tag{3.9}$$

is solved via a Newton-Raphson iteration, where the Jacobian of the residuals with respect to the characteristic variables for an arbitrary thermodynamic model can be written as

$$\frac{\partial(R_1, R_2, R_3)}{\partial(c_1, c_2, c_3)} = \begin{bmatrix} -\frac{1}{a^2}\left(\frac{\partial s}{\partial \rho}\right)_p & 0 & \frac{1}{2a^2}\left(\frac{\partial s}{\partial \rho}\right)_p + \frac{1}{2}\left(\frac{\partial s}{\partial p}\right)_\rho \\ 0 & \frac{1}{\rho a} & -\frac{1}{2\rho a}tan(\beta_u) \\ -\frac{1}{a^2}\left(\frac{\partial h}{\partial \rho}\right)_p & \frac{v_t}{\rho a} & \frac{1}{2a^2}\left(\frac{\partial h}{\partial \rho}\right)_p + \frac{v_n}{\rho a} + \frac{1}{2}\left(\frac{\partial h}{\partial p}\right)_\rho \end{bmatrix}. \tag{3.10}$$

The enthalpy derivatives are computed as

$$\left(\frac{\partial h}{\partial \rho}\right)_p = -\left(\frac{\partial p}{\partial \rho}\right)_u \left(\frac{\partial p}{\partial u}\right)_\rho^{-1} - \frac{p}{\rho^2}, \tag{3.11}$$

$$\left(\frac{\partial h}{\partial p}\right)_\rho = \left(\frac{\partial p}{\partial u}\right)_\rho^{-1} + \frac{1}{\rho}, \tag{3.12}$$

in which the partial pressure derivatives are also used to calculate the speed of sound

$$a = \sqrt{\left(\frac{\partial p}{\partial \rho}\right)_u + \frac{P}{\rho^2}\left(\frac{\partial p}{\partial u}\right)_\rho}. \tag{3.13}$$

The entropy derivatives can be written in terms of the partial derivatives of pressure with respect to temperature and density as

$$\left(\frac{\partial s}{\partial \rho}\right)_p = -a^2\left(\frac{\partial s}{\partial p}\right)_\rho, \tag{3.14}$$

$$\left(\frac{\partial s}{\partial p}\right)_\rho = \left[\rho^2\left(\frac{\partial p}{\partial T}\right)_\rho^{-1}\left(a^2 - \left(\frac{\partial p}{\partial \rho}\right)_T\right)\right]^{-1}. \tag{3.15}$$

Once the average and the harmonic component of each incoming characteristic, and the local outgoing characteristic have been computed, the characteristic change at the boundary nodes can be converted back into the change of the primitive variables. For instance, for the inflow boundary:

$$
\begin{pmatrix} \delta\rho \\ \delta v_n \\ \delta v_t \\ \delta p \end{pmatrix} = \begin{bmatrix} -\frac{1}{\bar{a}^2} & 0 & \frac{1}{2\bar{a}^2} & \frac{1}{2\bar{a}^2} \\ 0 & 0 & \frac{1}{2\bar{\rho}\bar{a}} & -\frac{1}{2\bar{\rho}\bar{a}} \\ 0 & \frac{1}{\bar{\rho}\bar{a}} & 0 & 0 \\ 0 & 0 & \frac{1}{2} & \frac{1}{2} \end{bmatrix} \begin{pmatrix} \delta c_1^{BC} \\ \delta c_2^{BC} \\ \delta c_3^{BC} \\ \delta \dot{c}_4 \end{pmatrix}.
\tag{3.16}
$$

The primitive variables change is summed to the average primitive variables to compute the boundary primitive variables:

$$
\begin{pmatrix} \rho^{BC} \\ v_n^{BC} \\ v_t^{BC} \\ p^{BC} \end{pmatrix} = \begin{pmatrix} \bar{\rho} + \delta\rho \\ \bar{v}_n + \delta v_n \\ \bar{v}_t + \delta v_t \\ \bar{p} + \delta p \end{pmatrix}.
\tag{3.17}
$$

These are used to compute the vector of conservative variables at the boundary, $\mathbf{U}^{BC}$, and the convective and the viscous numerical fluxes (cf. Section 2.4) for the residual in Eq. (2.8).

3.2.2 Average of Flow Quantities

NRBCs require that the Euler equations are linearized at the boundaries around an average state (cf. Eq. (3.17)). The *mixed-out* averaging procedure is the only physically consistent method for the average of flow quantities. [40] In this case, the fluxes based upon the average quantities must be equal to the specific integral fluxes at the boundary of interest. Thus, the averaged primitive variables $(\bar{\rho}, \bar{v}_n, \bar{v}_t. \bar{p})$ are computed by solving the following non linear system of equations:

$$
\bar{F}_\rho = \frac{1}{A} \int_A \rho v_n dA = \bar{\rho}\bar{v}_n,
\tag{3.18a}
$$

$$
\bar{F}_{v_n} = \frac{1}{A} \int_A (\rho v_n + p)\, dA = \bar{\rho}\bar{v}_n\bar{v}_n + \bar{p},
\tag{3.18b}
$$

$$
\bar{F}_{v_t} = \frac{1}{A} \int_A \rho v_n v_t dA = \bar{\rho}\bar{v}_n\bar{v}_t,
\tag{3.18c}
$$

$$
\bar{F}_e = \frac{1}{A} \int_A \rho v_n h_{tot} dA = \bar{\rho}\bar{v}_n\bar{h}_{tot},.
\tag{3.18d}
$$

By expressing the enthalpy as a function of the the average density and pressure

$$\bar{h}_{tot} = h(\bar{\rho}, \bar{p}) + \frac{\bar{v}_n^2 + \bar{v}_t^2}{2},$$ (3.19)

the energy flux equation can be reformulated as

$$f^n = \bar{F}_e - \bar{\rho}^n \bar{v}_n^n \left(h(\bar{\rho}^n, \bar{p}^n) + \frac{(\bar{v}_n^n)^2 + (\bar{v}_t^n)^2}{2} \right) = 0.$$ (3.20)

Equation (3.20) is solved iteratively to obtain the average pressure $\bar{p}$ and, successively, the average state.

The performance parameters can be determined once the average state has been computed. Those implemented are the entropy-generation rate, the total-pressure and the kinetic loss coefficient:

$$s_{gen} = \frac{\bar{s}_{out} - \bar{s}_{in}}{\bar{s}_{in}},$$ (3.21a)

$$z_{p,tot} = \frac{\bar{p}_{tot,in} - \bar{p}_{tot,out}}{\bar{p}_{tot,in} - \bar{p}_{out}}.$$ (3.21b)

$$z_{kin} = \frac{\bar{h}_{out} - \bar{h}_{is,out}}{(\bar{v}_{is,out})^2}.$$ (3.21c)

3.3 Fluid Dynamic Design Chain

3.3.1 Dependence of the objective function from design variables

Figure 3.1 schematically shows the dependence of the objective function $\hat{J}(\mathbf{D}) := J(\mathbf{U}(\mathbf{D})\mathbf{X}(\mathbf{D}))$ from the design variables $\mathbf{D}$. In the implementation described here, $\hat{J}$ can be any of the parameters in Eq. (3.21), while $\mathbf{D}$ is the surface variation. A change in $\mathbf{D}$ causes a variation in the surface coordinates $\mathbf{X}_{surf}$ which, in turn, requires a continuous deformation of the volume mesh $\mathbf{X}$. The deformed mesh is then used as an input to the flow solver to compute any arbitrary performance parameter.

3.3.1.1 Surface Deformation with FFD

The use of the surface nodes as design variables (i.e., $\mathbf{D} \,\widehat{=}\, \mathbf{X}_{surf}$) may lead to discontinuous solutions. Thus, it was selected the Free-Form Deformation (FFD) algorithm[41] that allows to continuously deform a rigid body enclosed in a lattice of control points.
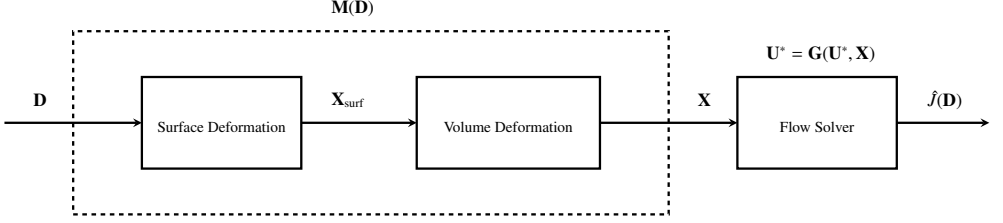
Figure 3.1: Formal representation of the evaluation of the performance parameter $\hat{J}(\mathbf{D}) :=$ $J(\mathbf{U}(\mathbf{D}), \mathbf{X}(\mathbf{D}))$.

If $\mathbf{X}_{\text{surf}}^k = (x_k, y_k)^T$ is a point on the surface enclosed in the lattice, its incremental displacement, expressed in local coordinates (d, g) and dependent on the control points variation $(\Delta\mathbf{P}_{i,j} = (\Delta x_{i,j}, \Delta y_{i,j})^T)$ is given by

$$\Delta\mathbf{X}_{\text{surf}}^k = \sum_{j=0}^{q} \sum_{i=0}^{o} B_i^o(d) B_j^q(g) \Delta\mathbf{P}_{i,j}, \tag{3.22}$$

where $B_i^o(d)$ and $B_j^q(g)$ are the i-th and j-th Bernstein polynomials of degree d and g. Therefore, to ensure continuity along the entire optimization process, the vector of the design variables is defined as the FFD control points (CP):

$$\mathbf{D} := (\Delta\mathbf{P}_{0,0}, \ldots, \Delta\mathbf{P}_{0,n}, \Delta\mathbf{P}_{1,0}, \ldots, \Delta\mathbf{P}_{m,n}). \tag{3.23}$$

3.3.1.2 Volume Deformation with the Linear Elasticity Equation

Since a re-meshing of the computational grid after each design step can be relatively CPU-expensive, the mesh deformation method devised by Dwight[42] was applied. In this approach, the mesh is modeled as an elastic solid using the linear elasticity equations. Hence, if a surface deformation $\Delta\mathbf{X}_{\text{surf}}$ is imposed as Dirichlet condition, the mesh deformation $\Delta\mathbf{X}$ can be computed by solving the following linear system:

$$\mathbf{K}\Delta\mathbf{X} = \mathbf{V}\Delta\mathbf{X}_{\text{surf}}, \tag{3.24}$$

where $\mathbf{K}$ is a constant stiffness matrix and $\mathbf{V}$ a projection matrix which reorders $\Delta\mathbf{X}_{\text{surf}}$ in accordance with $\mathbf{X}$. The mesh corresponding to the next iteration is then given by

$$\mathbf{X} = \mathbf{X}_{\text{old}} + \Delta\mathbf{X}. \tag{3.25}$$

Mesh periodicity is guaranteed at each iteration step.

3.3.1.3 Fixed-point Formulation of the Flow Solver

The solution of the flow equations formulated as $\mathbf{R}(\mathbf{U}, \mathbf{X}) = 0$ is often used as a constraint in the optimization problem.[43] However, this results in the decoupling of the discrete adjoint solver from the direct solver, leading to unnecessary loss of consistency, which

often diminishes the convergence properties of the adjoint solver. [35] On the contrary, the same convergence properties of the flow solver are inherited by the adjoint solver if it is applied the *fixed point iteration* approach, in which the constraint is the solution method of the flow equations itself(cf. Eq (2.9)):

$$\mathbf{U}^{n+1} = \mathbf{U}^n - \mathbf{B}^{-1}(\mathbf{U}^n, \mathbf{X})\mathbf{R}(\mathbf{U}^n, \mathbf{X}) =: \mathbf{G}(\mathbf{U}^n, \mathbf{X}). \tag{3.26}$$

$\mathbf{B}(\mathbf{U}, \mathbf{X})$ is a customarily first-order approximation of the flow Jacobian,

$$\mathbf{B}(\mathbf{U}, \mathbf{X}) \approx \frac{\partial \mathbf{R}(\mathbf{U}, \mathbf{X})}{\partial \mathbf{U}}, \tag{3.27}$$

and it is assumed that $\mathbf{G}$ is stationary only at feasible points $\mathbf{U}^*$:

$$\mathbf{R}(\mathbf{U}^*, \mathbf{X}) = 0 \Leftrightarrow \mathbf{U}^* = \mathbf{G}(\mathbf{U}^*, \mathbf{X}). \tag{3.28}$$

3.3.2 Discrete Adjoint Solver

The discrete adjoint solver was implemented following the approach proposed by *Albring et al.*.[35] Based on the design chain described in 3.3.1, the optimization problem is formulated as

$$\min_{D} \quad J(\mathbf{U}(\mathbf{D}), \mathbf{X}(\mathbf{D})), \tag{3.29}$$

$$\text{s.t.} \quad \mathbf{U} = \mathbf{G}(\mathbf{U}, \mathbf{X}), \tag{3.30}$$

$$\mathbf{X} = \mathbf{M}(\mathbf{D}). \tag{3.31}$$

$\mathbf{M}(\mathbf{D})$ is a linear function that formally contains the surface and mesh deformation as shown in Fig. 3.1. The Lagrangian associated to this problem is

$$L(\mathbf{D}, \mathbf{U}, \mathbf{X}, \bar{\mathbf{U}}, \bar{\mathbf{X}}) = J(\mathbf{U}, \mathbf{X}) + [\mathbf{G}(\mathbf{U}, \mathbf{X}) - \mathbf{U}]^T \bar{\mathbf{U}} + [\mathbf{M}(\mathbf{D}) - \mathbf{X}]^T \bar{\mathbf{X}} \tag{3.32}$$

$$= N(\mathbf{U}, \bar{\mathbf{U}}, \mathbf{X}) - \mathbf{U}^T \bar{\mathbf{U}} + [\mathbf{M}(\mathbf{D}) - \mathbf{X}]^T \bar{\mathbf{X}}, \tag{3.33}$$

where the shifted Lagrangian N is

$$N(\mathbf{U}, \bar{\mathbf{U}}, \mathbf{X}) := J(\mathbf{U}, \mathbf{X}) + \mathbf{G}^T(\mathbf{U}, \mathbf{X})\bar{\mathbf{U}}, \tag{3.34}$$

and $\bar{\mathbf{X}}$, $\bar{\mathbf{U}}$ are arbitrary Lagrange multipliers. Differentiating L with respect to $\mathbf{D}$, and by choosing $\bar{\mathbf{X}}$ and $\bar{\mathbf{U}}$ in such a way that the terms $\frac{\partial \mathbf{U}}{\partial \mathbf{D}}$ and $\frac{\partial \mathbf{X}}{\partial \mathbf{D}}$ can be eliminated, leads to the adjoint and the mesh sensitivity equation:

$$\bar{\mathbf{U}} = \frac{\partial}{\partial \mathbf{U}} N(\mathbf{U}, \bar{\mathbf{U}}, \mathbf{X}) = \frac{\partial}{\partial \mathbf{U}} J^T(\mathbf{U}, \mathbf{X}) + \frac{\partial}{\partial \mathbf{U}} \mathbf{G}^T(\mathbf{U}, \mathbf{X})\bar{\mathbf{U}}, \tag{3.35}$$

$$\bar{\mathbf{X}} = \frac{\partial}{\partial \mathbf{X}} N(\mathbf{U}, \bar{\mathbf{U}}, \mathbf{X}) = \frac{\partial}{\partial \mathbf{X}} J^T(\mathbf{U}, \mathbf{X}) + \frac{\partial}{\partial \mathbf{X}} \mathbf{G}^T(\mathbf{U}, \mathbf{X})\bar{\mathbf{U}}. \tag{3.36}$$

Similarly to the iterative method used for the solution of the flow equations, Eq. (3.26), the adjoint equation, Eq. (4.17), is solved iteratively with the fixed-point iteration:

$$\bar{\mathbf{U}}^{n+1} = \frac{\partial}{\partial \mathbf{U}} N(\mathbf{U}^*, \bar{\mathbf{U}}^n, \mathbf{X}), \tag{3.37}$$
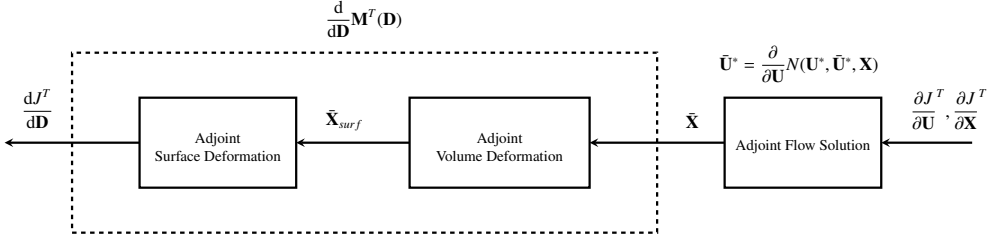
Figure 3.2: Formal representation of the evaluation of $\frac{\mathrm{d}\hat{J}}{\mathrm{d}\mathbf{D}}$.

where $\mathbf{U}^*$ is a numerical solution of the flow equations. Once the adjoint solution $\bar{\mathbf{U}}^*$ has been found, the mesh node sensitivity $\bar{\mathbf{X}}$ is computed by evaluating Eq. (3.36), and the total derivative of J with respect to the design variables, which is also the total derivative of the Lagrangian, is given by

$$\frac{\mathrm{d}J}{\mathrm{d}\mathbf{D}}^T = \frac{\mathrm{d}L}{\mathrm{d}\mathbf{D}}^T = \frac{\mathrm{d}}{\mathrm{d}\mathbf{D}}\mathbf{M}^T(\mathbf{D})\bar{\mathbf{X}}. \tag{3.38}$$

As for the dependence of the objective function from the design variables, shown in Section 3.3.1, it is also possible to define a corresponding reverse dependence for the gradient $\frac{\mathrm{d}\hat{J}}{\mathrm{d}\mathbf{D}}$ (cf.Fig. 3.2). The partial derivatives of the objective function are given as input parameters to the adjoint flow solver, which computes the adjoint solution $\bar{\mathbf{U}}$, Eq. (3.35), and the node sensitivity $\bar{\mathbf{X}}$, Eq. (3.36). $\bar{\mathbf{X}}$ is then the input to the routine computing the volume and the surface sensitivity, and the gradient of the objective function with respect to the design variables $\frac{\mathrm{d}J}{\mathrm{d}\mathbf{D}}^T$, Eq. (3.38).

3.3.3 Gradients Evaluation with Algorithmic Differentiation

Algorithmic Differentiation, also known as *Automatic Differentiation*, is a method to calculate the derivative of a programmed function by manipulating the source-code.[44] As an example, consider a generic function $\mathbf{y} = \mathbf{f}(\mathbf{x})$. It can be demonstrated that the product

$$\bar{\mathbf{x}} = \left[\frac{\partial\mathbf{f}(\mathbf{y})}{\partial\mathbf{y}}\right]^T \bar{\mathbf{y}}, \tag{3.39}$$

where $\bar{\mathbf{y}}$ is an arbitrary seed vector, can be obtained by using the reverse mode of AD. Eq. (3.39) resembles the second term of the right hand side of the adjoint equation (3.35), where $\mathbf{f}$, $\mathbf{y}$, and $\bar{\mathbf{y}}$ denote the fixed-point iteration associated with the flow equations $\mathbf{G}$, the state vector $\mathbf{U}$, and the adjoint vector $\bar{\mathbf{U}}$, respectively.

The open-source AD tool CoDiPack,[34] which had been already successfully applied to SU2,[35] was also selected for this work. Compared to other AD approaches, CoDi-Pack exploits the Expression Templates feature of C++. This approach introduces only a small overhead in terms of statement run-time. Thus, the black-box application of AD to complicated non-linear iterative functions becomes feasible. Furthermore, this method is

computationally efficient whenever there are code parts containing statements that are not directly involved in the calculation of derivatives, which avoids to perform the extensive derivative-dependency analysis that is necessary in most applications of AD. [45]

3.4 Results and Discussion

The capabilities of the FSO method described in Section 3.3 are demonstrated by re-designing a supersonic and a transonic cascade that are representative of typical cascades adopted in single-stage and multi-stage ORC turbines. [46] The illustration of the two test cases follows the same structure. First, the gradient validation is reported, in which the adjoint sensitivities of the objective function and constraint are compared with their finite-difference (FD) equivalent. Second, the results of the optimization are documented. Lastly, the optimization results obtained with the inviscid flow and adjoint solver are also discussed and compared with the ones obtained with the RANS solvers.

In both test-cases the chosen working medium is siloxane MDM, modeled with the polytropic Peng-Robinson (PR) equation of state (EoS). The parameters of the model are listed in Table 3.1. Turbulent computations are carried out with the k-ω SST model, [47] ensuring wall y+ below unity along the blade surface. The optimizer is the *minimize*

Fluid	MDM	-
R^*	35.23	$[\text{Jkg}^{-1}\text{K}^{-1}]$
γ	1.02	[-]
T_{cr}	564.1	[K]
p_{cr}	1.415	[MPa]
θ	0.529	[-]

Table 3.1: Peng-Robinson EoS parameters for the MDM organic fluid.

routine of the python library *scipy.optimize*. This routine implements the Sequential Least SQuares Programming (SLSQP) algorithm introduced by Kraft. [48]

3.4.1 Supersonic Cascade

The supersonic cascade considered in this work was previously investigated and documented.[5,21,22] The simulation of the flow around the baseline geometry shows that significant fluid-dynamic penalties are present because of a strong shock-wave forming on the rear suction side of the blade.

The optimization problem was set up as

$$\min_{CPs} \quad s_{\text{gen}} \tag{3.40}$$

$$\text{subject to} \quad \dot{m} = \dot{m}_{\text{b}}. \tag{3.41}$$

The entropy-generation rate is minimized under the constraint of preserving the baseline mass-flow rate. The boundary conditions for the simulation are summarized in Table 3.2. Although total inlet temperature and pressure quantities are given as input for the inflow conditions, these are internally converted to total enthalpy and entropy, which are eventually imposed at the boundary (cf. Section 3.2.1).

$T_{\text{tot,in}}$	545.1	[K]
$p_{\text{tot,in}}$	0.80	[MPa]
β_{in}	0.0	[°]
p_{out}	0.10	[MPa]
$I_{\text{tur,in}}$	0.03	[-]
$\left(\frac{\mu_{\text{tur}}}{\mu_{\text{lam}}}\right)_{\text{in}}$	100.0	[-]

Table 3.2: Inlet and outlet boundary conditions values for the supersonic nozzle test-case.

According to the convergence study on the baseline geometry, a maximum number of 1200 iterations was set for both the flow and the adjoint solver, and the solutions were obtained with an implicit time-marching Euler scheme with a CFL number of 40 on 44000 grid points mesh.

3.4.1.1 Gradient Validation

The gradient of the objective function and constraint were first validated against FD. To ease the process, a simple FFD box of 9 control points was selected (Fig. 3.3), and the validation was conducted by using a FD step-size equal to 1E-05. Figure 3.4 shows that the objective function and constraint gradient provided by the NICFD adjoint very accurately correlate with the correspondent FD values. This result is also a confirmation that the selected convergence criterion guarantees an accurate estimation of the gradient.

3.4.1.2 Optimization

Differently from the validation, in which the process can be considered FFD-degree independent, the FFD box for the optimization is composed by 121 control points, as can
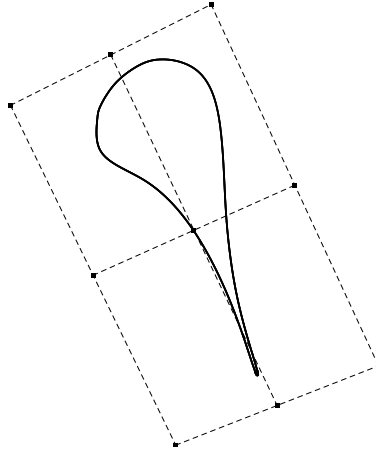
Figure 3.3: 2D FFD box of degree two on both directions (9 CPs) used for the validation of the discrete adjoint gradient against FD for the supersonic nozzle test-case.

be seen in Fig. 3.5. This choice was made to ensure a high level of design flexibility, which is of primary concern for cascades operating in the supersonic regime, for which slight geometrical modifications can lead to largely different performance. In addition, to prevent unfeasible designs, the sensitivity around the trailing-edge was nullified at each optimization iteration. This has a twofold effect. First, it ensures that a minimum acceptable value of the blade thickness is maintained, without directly introducing a geometrical constraint on the thickness distribution. Second, it alleviates mesh deformation issues at the trailing-edge. To guarantee a smooth convergence, the step size of the SLSPQ optimizer was under-relaxed with a value equal to 1E-05 for both the objective function sensitivity and the constraint sensitivity.

The normalized optimization history in Fig. 3.6 shows that, within 5 iterations, the blade entropy-generation rate is reduced by as much as 45%. A similar reduction is found for the other two performance parameters (Table 3.3), suggesting that the optimal shape is independent from the type of performance parameter. The equality constrain on the mass-flow rate is satisfied with an negligible error of 0.01% with respect to the prescribed value.

The Mach contours of both the baseline and the optimal solution are depicted in Figs. 3.7 and 3.8, and the normalized pressure distributions in Fig. 3.9. In the baseline configuration the simulated flow over-accelerates in the semi-blade region after the outlet divergent section, and this generates an oblique shock on the rear suction side. The
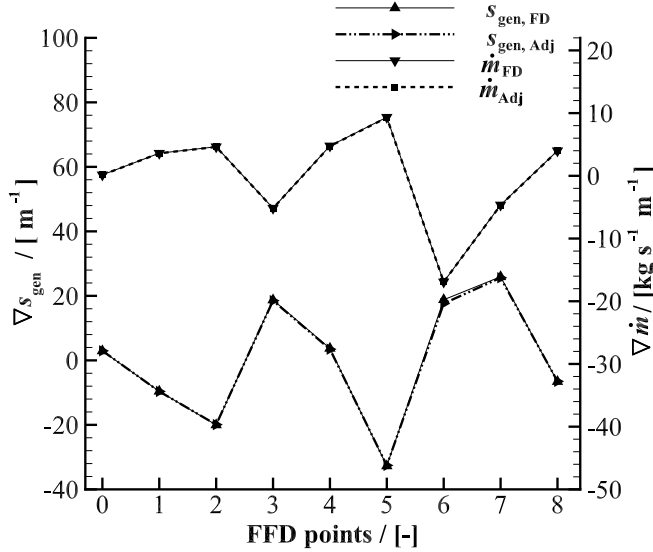
Figure 3.4: FD discrete adjoint gradient validation of the objective function and constrain used for the supersonic-nozzle optimization.

	s_{gen}	$z_{p,tot}$	z_{kin}	
baseline	176.7	22.78	7.833	[%]
optimal	97.20	12.62	4.157	[%]
ratio	55.00	55.39	53.07	[%]

Table 3.3: Fluid-dynamic loss reduction measured with three different performance parameters for the supersonic-nozzle test-case.

over-acceleration is promoted by the continuing increase of flow passage area in the semi-blade region. On the contrary, in the optimized nozzle, the flow acceleration is more pronounced in the divergent channel, after which the flow keeps smoothly expanding trough the re-designed straight semi-bladed channel. This results in the complete removal of the shock-wave from the suction-side, and, consequently, in a much more uniform flow at the outlet.

Figure 3.10 illustrates the geometrical transformation performed by the optimizer. The baseline curve FX-T1 deforms into FX-T2, generating a straight semi-blade channel ($\overline{FXSB1} \simeq \overline{T2SB2}$), which allows avoiding the over speed. The curve P1-T1 transforms into P1-T2 in order to maintain the constrained trailing-edge shape, and so does the S1-S2 curve, thus preserving the throat dimension ($\overline{oo} = \overline{gg}$) imposed by the mass-flow con-
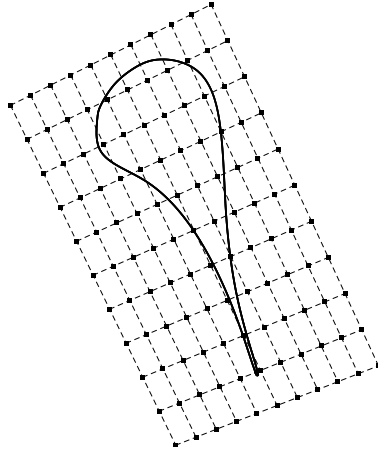
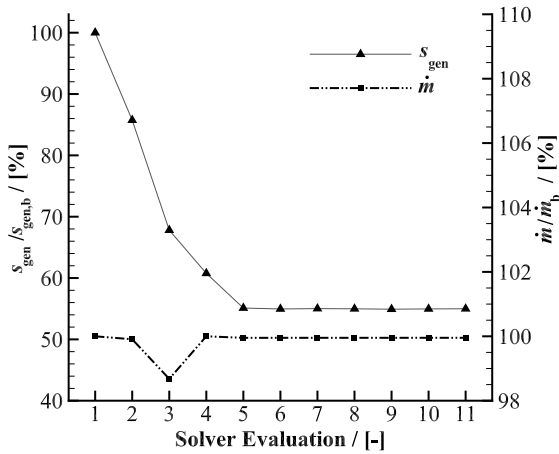Figure 3.5: 2D FFD box of degree ten on both directions (121 CPs) used for the supersonic-nozzle optimization.

Figure 3.6: Convergence history of the turbulent supersonic-nozzle optimization.
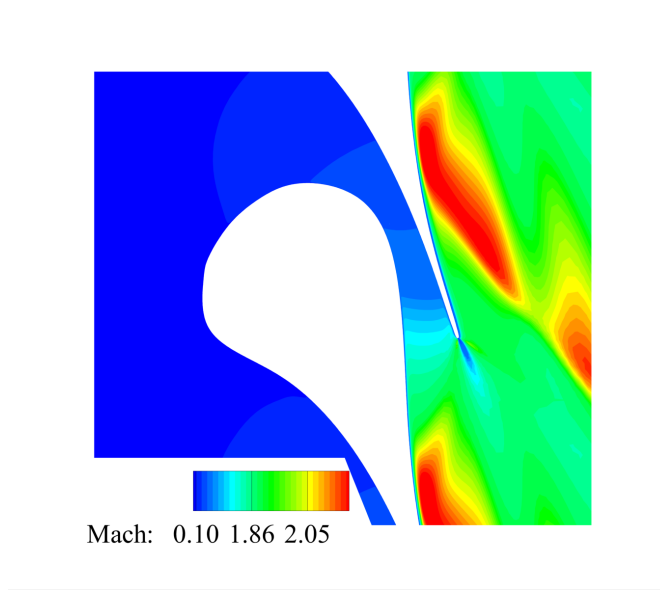
Mach: 0.10 1.86 2.05

Figure 3.7: Mach number contour of the baseline supersonic nozzle test-case.

straint. The optimized throat $\overline{gg}$ is also shifted slightly upstream to better accommodate the higher expansion ratio of the divergent channel ($\overline{D2T2} > \overline{D1T1}$). The two geometrical deformations driving the optimization are: i) the S2-FX curve, which increases the divergent's expansion ratio; ii) the straightening of FX-T2, which defines the constant passage-area in the semi-blade channel. All the other transformations ensure the preservation of all the constraints.

3.4.1.3 Inviscid Optimization

To gain knowledge of the influence of simulated viscous effects on the design of supersonic ORC cascades, the optimization was repeated using the inviscid adjoint solver. As expected, the use of the inviscid model results into an underestimation of the actual value of the entropy-generation rate, which in the case of the baseline geometry is equal to 129% compared to around 177% predicted by the turbulent solver. Nevertheless, Fig. 3.11 shows that the inviscid and the turbulent optimizations converge to the same optimal geometry, suggesting that the solution of the design problem is driven by the inviscid flow phenomena (i.e., shock-waves). In addition, the computed boundary-layer viscous losses are very similar in the two studied cases. Further numerical experiments demonstrated that this is only valid if the the trailing-edge thickness is constrained to its initial value; since, if the thickness is not constrained, the optimization with the turbulent adjoint would lead to a sharp trailing edge, as expected.
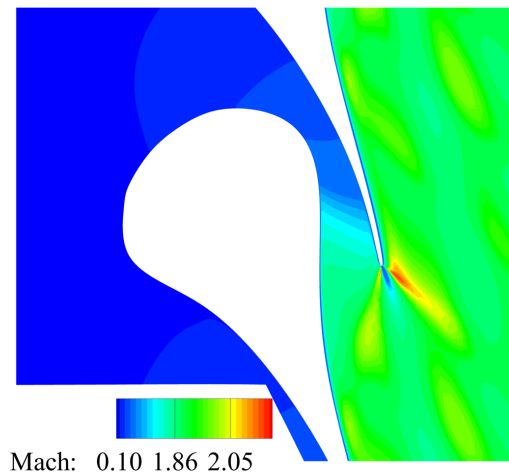
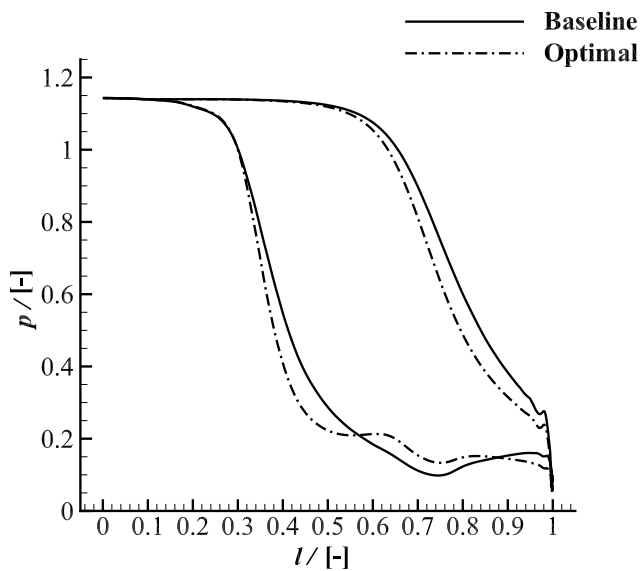Figure 3.8: Mach number contour of the optimized supersonic nozzle test-case.

Figure 3.9: Comparison of the profile normalized pressure distribution between the baseline and the optimal solution of the supersonic-nozzle test-case.
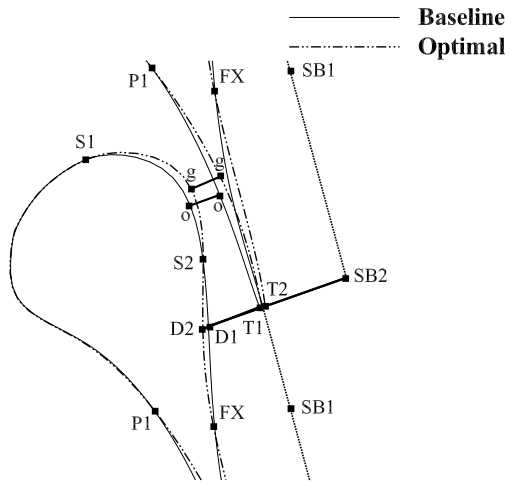
Figure 3.10: Geometrical comparison between the baseline and the optimal profile of the supersonic-nozzle test case.
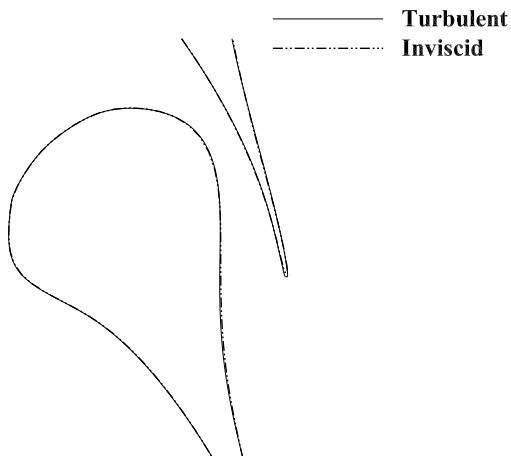

Figure 3.11: Comparison between the turbulent and the inviscid supersonic-nozzle optimized profile.

3.4.2 Transonic Cascade

The second exemplary test case is representative of the fluid dynamic design of transonic cascades commonly found in multi-stage ORC turbines. The operating conditions of the cascade are listed in Table 3.4. The inlet total pressure and temperature correspond to the inlet turbine conditions of a super-heated MDM thermodynamic cycle; the outlet back pressure was chosen such to obtain a sonic flow at the outlet.

$T_{tot,in}$	592.3	[K]
$p_{tot,in}$	1.387	[MPa]
β_{in}	0.0	[°]
p_{out}	0.10	[MPa]
$I_{tur,in}$	0.03	[-]
$\left(\frac{\mu_{tur}}{\mu_{lam}}\right)_{in}$	100.0	[-]

Table 3.4: Operating conditions of the transonic cascade test-case.

Under the above conditions, the simulated suction-side flow reaches a maximum Mach number of 1.12 at about 90% of the axial-chord length. Afterwards, a shock-wave is generated allowing for a pressure matching downstream of the trailing-edge. The shock causes a sudden increase of the boundary-layer thickness, which eventually results in a more pronounced wake, and, correspondingly, to significant profile losses.[49]

The cascade was optimized by minimizing the total-pressure loss coefficient

$$\min_{CPs} \quad z_{p,tot}. \tag{3.42}$$

However, since the profile-losses are proportional to the flow-deflection,[49] an unconstrained optimization would ideally converge to a zero-deflection blade. To overcome this issue, the optimization problem was constrained by imposing a minimum tolerable value of the the outlet flow angle

$$\text{subject to} \quad \beta_{out} > 74.0°. \tag{3.43}$$

The optimization was performed with a FFD box of degree four in both directions (Fig. 3.12). However, only 20 of the 25 FFD CPs were chosen as a design variables, and the remaining five, belonging to the short-side of the box next to the trailing-edge were kept fixed to prevent unfeasible designs. The flow and adjoint simulations were marched in time for 2000 iterations on a grid of 17,500 elements using an implicit Euler scheme with a CFL equal to 30.

3.4.2.1 Gradient Validation

In order to verify the accuracy of the adjoint for predominantly viscous flows, the gradient values was validated against the FD ones using a step-size of 5.0E-06. Figure 3.13 shows
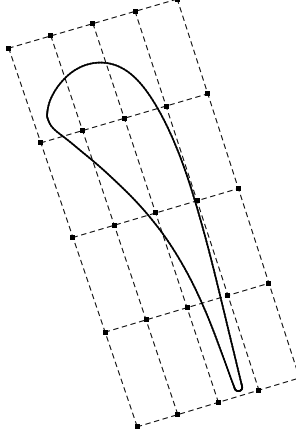
Figure 3.12: 2D FFD box of degree four on both directions (25 CPs) used for transonic-cascade optimization.

that the norm of the two gradients correlates well, confirming the correct linearization of the RANS flow solver.

3.4.2.2 Optimization

As Fig. 3.14 shows, the optimization process converges in 16 iterations. The total-pressure loss coefficient is reduced of about 20% with respect to the initial value, and, as expected, similar reductions are also obtained for the other performance parameters (Table 3.5). Furthermore, the optimized flow angle is set to the lower bound of 74° so that, given the constant inflow angle, the flow deflection is reduced to its minimum allowable value.

	$s_{\mathrm{gen,b}}$	$z_{p,\mathrm{tot}}$	z_{kin}	
baseline	5.274	5.492	4.116	[%]
optimal	4.177	4.295	3.238	[%]
ratio	79.20	78.20	78.67	[%]

Table 3.5: Fluid-dynamic loss reduction measured with three different performance parameters for the transonic-cascade test-case.
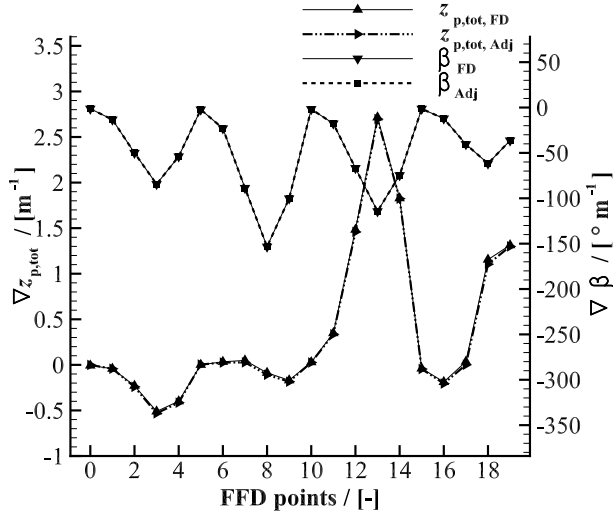
Figure 3.13: FD discrete adjoint gradient validation of the objective function and constrain used for the transonic-cascade optimization.
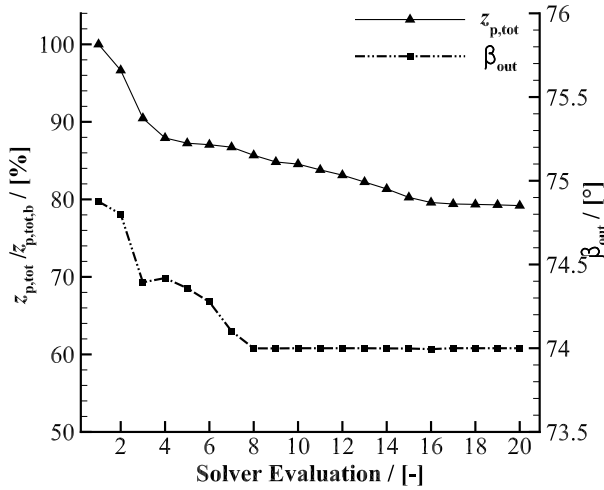

Figure 3.14: Convergence history of the turbulent transonic-cascade optimization.

The baseline and the optimal profile (Fig. 3.15) are compared in terms of normalized pressure distribution in Fig. 3.16. It can be observed that the suction-side velocity peak occurs much more upstream in the optimized blade than in the baseline blade, leading to a smoother flow deceleration on the rear suction side, thus weakening the strength of the shock-wave. This is more evident if the Mach number contours depicted in Figs. 3.17 and 3.18 are considered. The optimal blade features a reduced outgoing boundary-layer thickness and wake with respect to the baseline. On the contrary, the simulated flow around both geometries display similar characteristics on the pressure side, confirming that most of the losses in transonic ORC cascades are caused by adverse pressure gradients on the rear suction side.
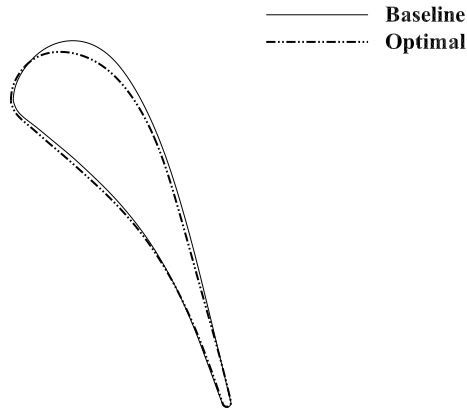

Figure 3.15: Comparison between the optimized and the baseline profiles of the transonic cascade test-case.

3.4.2.3   Inviscid Optimization

The optimization of the transonic cascade was repeated by using the inviscid flow solver in order to gain insight whether the use of a simpler model can still be advantageous for the design of transonic ORC blades. Interestingly, though Fig. 3.19 shows that the optimization process leads to a reduction of the (inviscid) total-pressure loss coefficient of about 13%, the optimal geometry is practically coincident with the baseline (Fig. 3.20), and the performance improvement predicted by the turbulent solver is negligible (around 1% w.r.t. the initial turbulent value). Apparently, since the main cause of irreversibility are the viscous losses in the boundary-layer, the inviscid adjoint is inadequate for such cases and only a fully viscous adjoint method is suitable for the optimization of transonic ORC cascades.
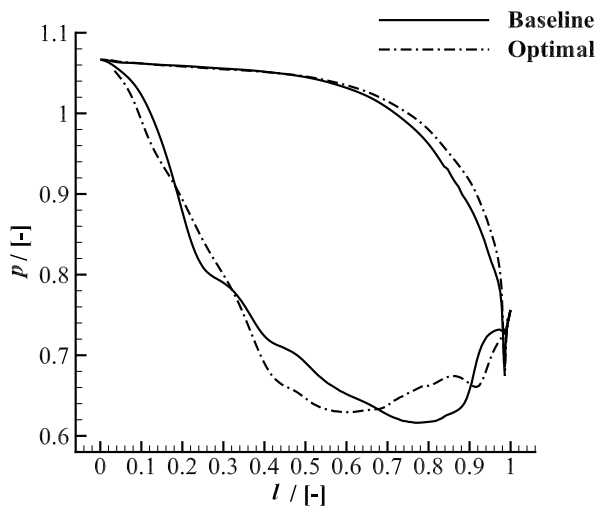
Figure 3.16: Comparison of the profile normalized pressure distribution between the baseline and the optimal solution of the transonic cascade test-case.
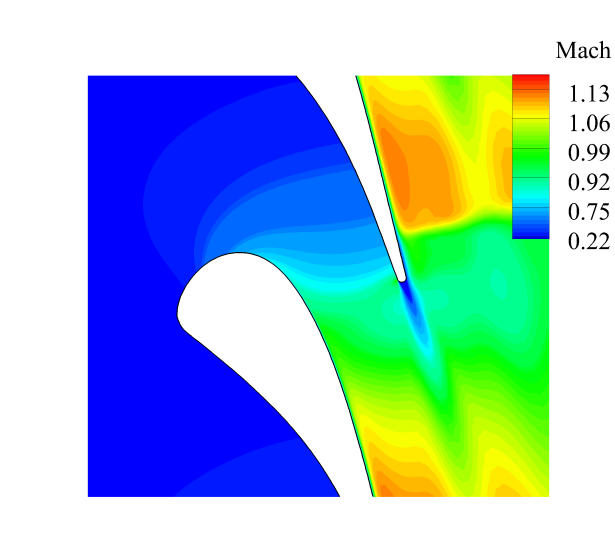

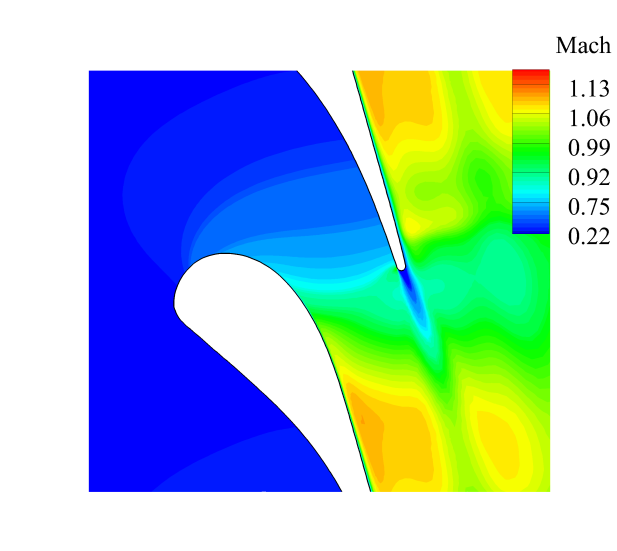Figure 3.17: Mach number contour of the baseline transonic cascade test-case.

Figure 3.18: Mach number contour of the optimized transonic cascade test-case.
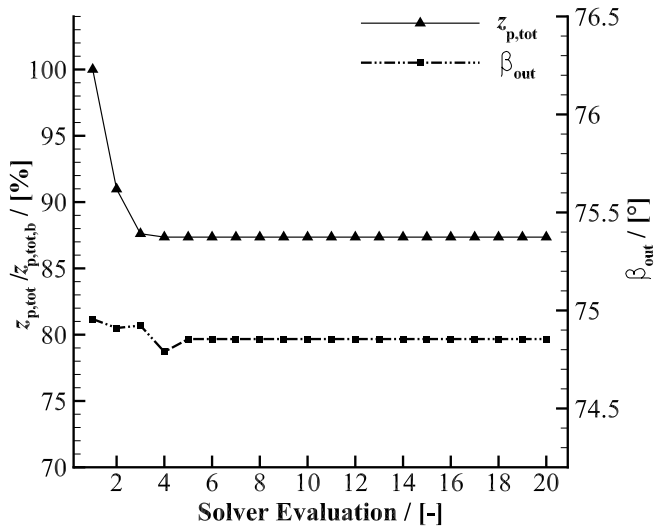

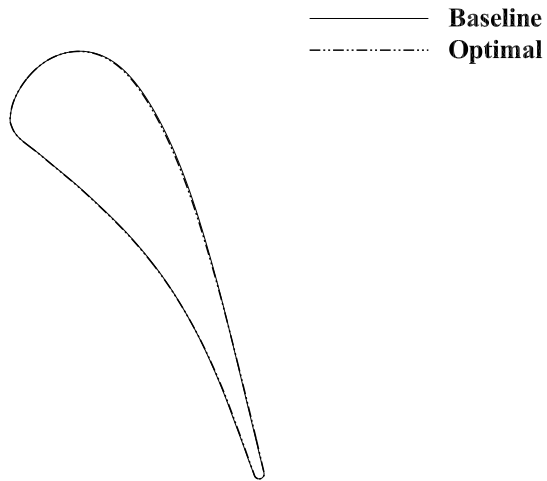Figure 3.19: Inviscid optimization history of the transonic cascade.

Figure 3.20: Comparison between the baseline and the optimal solution obtained using the inviscid solver for the transonic cascade test-case.

3.5   Influence of the thermodynamic model on the optimal solution

The nozzle of ORC turbines commonly operate with the fluid in thermodynamic states far from ideal gas conditions. As demonstrated in a previous work,[5] the use of over-simplified thermodynamic models may lead to inaccurate predictions of the main flow features. Table 3.6 shows, for example, that there are some discrepancies between supersonic-nozzle performance values calculated with the Ideal Gas (IG) EoS and those calculated with the more accurate PR EoS. Correspondingly, neglecting non-ideal effects in the gra-

	IG	PR	
$z_{p,tot}$	18.36	22.78	[%]
$\dot{m}$	6.384	5.953	[-]
M_{out}	1.965	1.913	[-]
β_{out}	77.27	76.05	[°]

Table 3.6: Summarized results of the supersonic-nozzle test-case for different EoSs.

dient calculation may lead to sub-optimal blade shape configurations. Nevertheless, as the majority of the available turbomachinery adjoint solvers only implement the polytropic ideal gas model, it is of practical interest to evaluate when the adoption of such model may lead to satisfactory results. To this purpose, the blade geometries documented in Section 3.4 were re-optimized using the polytropic ideal gas model. The optimal solutions were then compared with the ones shown in Section 3.4. The optimal solution calculated using the polytropic ideal gas model is labeled "Optimal-IG", while that calculated with the PR model is labeled "Optimal" as in all the figures in Section 3.4.

In order to correctly evaluate the performance of the optimized geometry obtained with the flow and adjoint solver linked to the polytropic ideal gas model, the flow solution around such geometry was computed also with the PR model. This solution was then compared with optimized solution illustrated in Section 3.4. Except the thermodynamic model, all the other test-case parameters (optimization problems, boundary conditions, meshes, FFD box, etc.) were kept the same.

Figure 3.21 depicts the IG-optimization history of the supersonic nozzle test case. It shows that an optimal solution is found within 9 iteration. The predicted entropy generation reduction is around 37%, and the constant mass-flow rate constrain is tightly satisfied.

As shown in Fig. 3.22, the optimizer is able to calculate a solution for which no shock wave occurs at the rear suction-side of the blade, even if the ideal gas model is used for the computation of fluid properties. The obtained geometry is very similar to the one obtained using the PR model, except for a slight offset, see Fig. 3.23. Even if the geometries are very similar, the calculated performance is different, as reported in Table 3.7. The performance improvement calculated for the Optimal-IG geometry is 5% lower if compared to that calculated for the Optimal geometry.
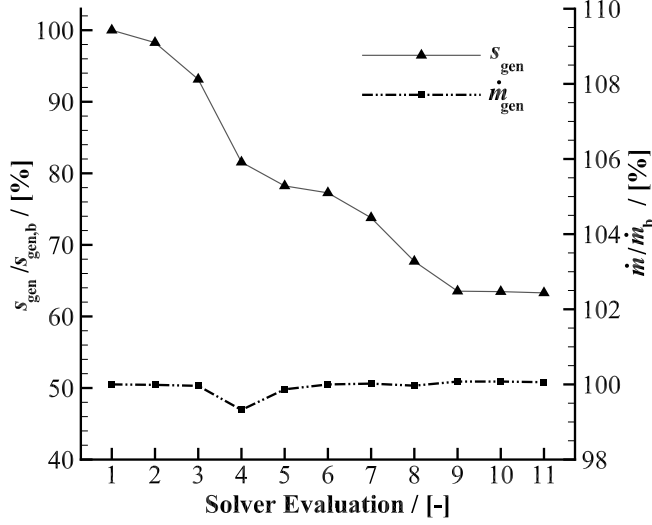
Figure 3.21: Convergence history of the turbulent supersonic-nozzle optimization using the IG EoS.

	baseline	optimal	optimal-IG	
s_{gen}	176.7	97.20	106.3	[%]
$s_{\text{gen,opt}}/s_{\text{gen,b}}$	-	55.00	60.51	[%]

Table 3.7: Summarized results of the supersonic-nozzle optimization for different EoSs.

However, even the use of the inaccurate ideal gas model allows to calculate a substantial improvement with respect to the baseline, though suboptimal. This result can be explained by observing that the geometry optimization occurs mainly in an area of the flow field where the compressibility factor is close to unity, see Figs. 3.24 and 3.10.

	baseline	optimal	optimal-IG	
$z_{\text{p,tot}}$	5.27	4.18	6.49	[%]
$z_{\text{p,tot,opt}}/z_{\text{p,tot,b}}$	-	79.32	123.1	[%]

Table 3.8: Summarized results of the supersonic-nozzle optimization for different EoS.
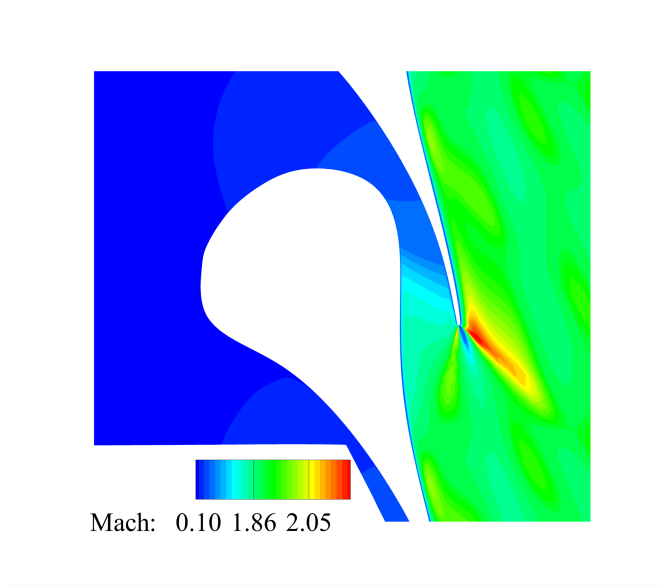
Figure 3.22: Mach number contour of the Optimal-IG supersonic nozzle.

On the contrary, if the cascade is transonic and operates with the fluid completely in the non-ideal thermodynamic regime, the use of the more accurate thermodynamic model is mandatory (Fig. 3.25). Table 3.8 shows that the simulation corresponding to the Optimal-IG geometry (see Fig. 3.26) leads to the estimation of a performance that is lower than that of the baseline. This is due to the fact that the peak velocity is higher, and the normal shock wave on the suction side is stronger (Fig. 3.27).
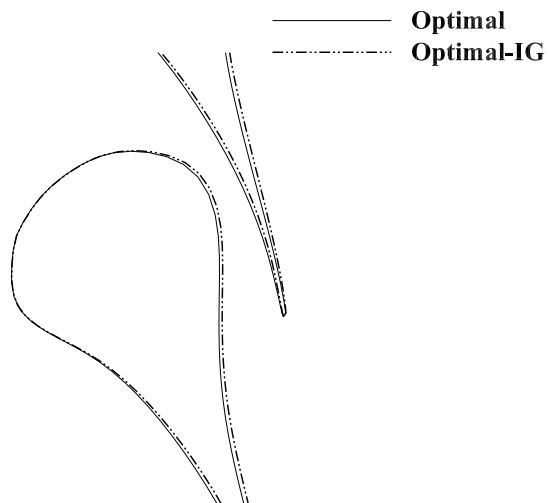
Figure 3.23: Comparison between the PR and IG optimal profile for the supersonic nozzle test-case.

Figure 3.24: Compressibility factor contour of the supersonic-nozzle test-case.

Figure 3.25: Compressibility factor contour of the transonic cascade test-case.

Figure 3.26: Comparison between the PR and IG optimal profile for the transonic cascade test-case.
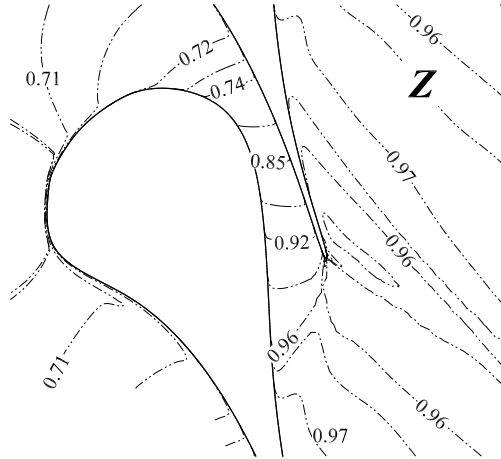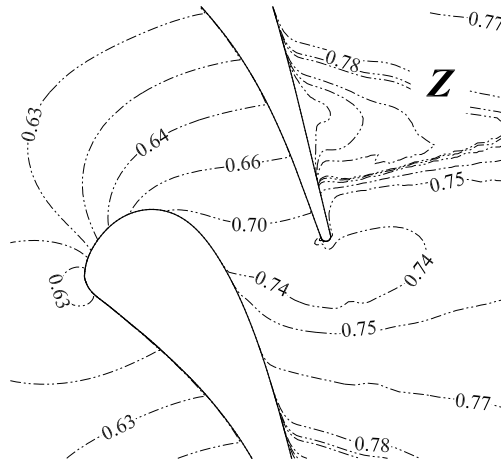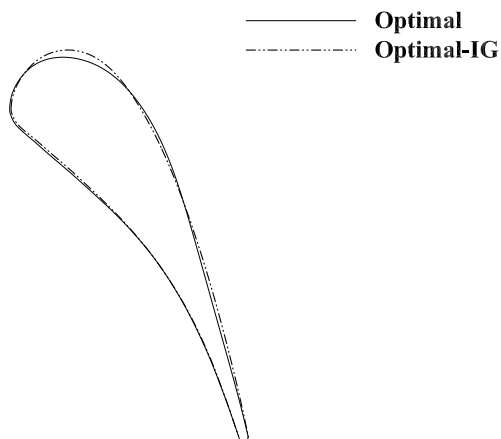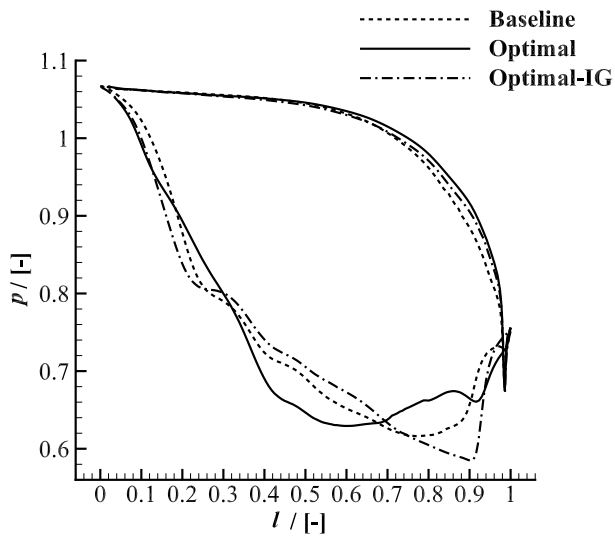

Figure 3.27: Normalized pressure distribution of the baseline, and the PR and IG optimal solutions for the transonic cascade test-case.

3.6 Conclusion

This chapter documents the derivation, validation and application of a NICFD fully-turbulent adjoint solver for the design of Organic Rankine Cycle turbomachinery. To achieve this goal, the flow solver of SU2, an open-source CFD suite, was extended with ad-hoc turbomachinery boundary conditions. The adjoint solver was devised by resorting to automatic differentiation. The effectiveness of the NICFD adjoint solver was tested by re-designing two exemplary cases: a supersonic and a transonic ORC turbine cascade.

Based on the results of this chapter, the following main conclusions can be drawn.

1. Despite the high level of additional complexity due to the need of treating accurate fluid thermodynamic models, it was possible to obtain an exact fully-turbulent adjoint. The linearization of the flow solver was performed with an open-source operator-overloading AD tool (CoDiPack). Given its small overhead in terms of run-time, the AD was applied to the entire flow solver iteration in a black-box manner, thus avoiding a posteriori and ad hoc intervention, which is error-prone.

2. The capability of the new method was demonstrated by redesigning two typical 2D ORC turbine cascades, in which fluid properties are calculated with the polytropic Peng-Robinson model. In both cases, the optimization performed with the RANS flow and adjoint solver substantially improved the simulated cascades performance, while satisfying the imposed constraints. The optimization process was also repeated assuming inviscid flows. The results emphasize the importance of incorporating the viscous and turbulent gradient contributions, especially for the design of transonic ORC cascades.

3. The potential of the non-ideal compressible RANS adjoint was also shown by comparison with a more conventional ideal gas adjoint method, using the same test cases. The results demonstrate that the simplified approach provides physically inaccurate gradient information leading to sub-optimal cascade configurations, if NICFD effects are moderate. Instead, in case of strong NICFD effects, the calculated performance can be even worse than that of the starting geometry.

Future work will be devoted to the extension of the proposed approached to deal with fluid thermodynamic libraries that are external with respect to the flow solver. In this way, the method can leverage the large number of available software. In addition, the capability of optimizing 3D and multi-stage geometries is being implemented.

Nomenclature

Abbreviations

NICFD	Non-Ideal Compressible Fluid-Dynamics
FSO	Fluid-Dynamic Shape Optimization
ORC	Organic Rankine Cycle
AD	Algorithmic Differentiation
NRBC	Non Reflecting Boundary Condition
CP	Control Point
FFD	Free-Form Deformation
FD	Finite Difference
PR	Peng-Robinson
EoS	Equation of State
SLSPQ	Sequential Least SQuares Programming
IG	Ideal-Gas

Symbols

$\mathbf{U}$	Conservative or State Variables Vector
$\mathbf{F}$	Flux Vector
Ω	Volume
t	Time
Q	Source Term
p	Pressure
T	Temperature
C_p	Specific Heat Capacity at Constant Pressure
μ	Dynamic Viscosity
k	Thermal Conductivity
$\mathbf{R}$	Residuals Vector
δ_{ij}	Kronecker Delta
$(\hat{\cdot})$	Boundary Harmonic Value
$(\bar{\cdot})$	Boundary Average Value
$(\cdot)$	Boundary Local Value
$\mathbf{c}$	Characteristic Variables Vector
v	Velocity
S	Pitch
y	Tangential/Pitch-wise Coordinate
m	Fourier Frequency
α	Giles' Parameter
ρ	Density
a	Speed of Sound
h	Enthalpy
s	Entropy
β	Flow Angle
u	Internal Energy
A	Flow Passage Area

z	Loss coefficient
f	Generic Function
D	Design Variables Vector
J	Objective Function
X	Surface and Volume Mesh Nodes
P	Cartesian Control Point
B	Bernstein Polynomial
d, g	Local Parametric Coordinates
o, q	Generic Polynomial Degrees
K	Constant Stiffness Matrix
V	Reordering Matrix
B	Flow Jacobian
G	Flow Solver Iteration
M	Surface and Mesh Deformation Matrix
L	Lagrangian
N	Shifted Lagrangian
$\bar{\mathbf{U}}$	Flow Adjoint Variables Vector
$\bar{\mathbf{X}}$	Mesh Adjoint Variables Vector
$\bar{\mathbf{x}}, \bar{\mathbf{y}}$	Generic Vectors
R^*	Specific Gas Constant
γ	Specific Heat Capacity Ratio
θ	Acentric Factor
$\dot{m}$	Mass Flow rate
I_{tur}	Turbulent Intensity
Superscript	
c	Convective
v	Viscous
n	n-th Iteration
BC	Boundary Condition Value
Subscript	
mol	Molecular
tur	Turbulent
tot	Total
i, j, k	Indices
t	Tangential
n	Normal
u	User-Specified
kin	Kinetic
gen	Generation
in	inlet
out	outlet
is	isentropic
surf	surface
cr	critical

b   Baseline
opt   Optimal

References

[1] Nicfd 2016: 1st international seminar on non-ideal compressible-fluid dynamics for propulsion and power.

[2] Cramer, M., 1991. "On the mach number variation in steady flows of dense hydrocarbons". *ASME J. Fluids Eng.,* **113**(4), pp. 675–680.

[3] Harinck, J., Guardone, A., and Colonna, P., 2009. "The influence of molecular complexity on expanding flows of ideal and dense gases". *Physics of fluids,* **21**(8), pp. 86–101.

[4] Zamfirescu, C., Guardone, A., and P., C., 2008. "Admissibility region for rarefaction shock waves in dense gases". *Journal of Fluid Mechanics,* **599**, pp. 363–281.

[5] Colonna, P., Harinck, J., Rebay, S., and Guardone, A., 2008. "Real-gas effects in organic rankine cycle turbine nozzles". *Journal of Propulsion and Power,* **24**(2), pp. 282–294.

[6] Pecnik, R., Rinaldi, E., and Colonna, P., 2012. "Computational fluid dynamics of a radial compressor operating with supercritical co_2". *ASME J. Eng. Gas Turbines Power,* **134**(12).

[7] Baltadjiev, N., Lettieri, C., and Spakovszky, Z., 2014. "An investigation of real gas effects in supercritical $c0_2$ centrifugal compressors". *Journal of Turbomachinery,* **137**(9).

[8] Bassi, F., Pelagalli, L., Rebay, S., Betto, A., Orefice, M., and Pinto, A., 2000. "Numerical simulation of a reciprocating compressor for household refrigerators". *International Compressor Engineering Conference*.

[9] Bartosiewicza, Y., Aidouna, Z., and Mercadierb, Y., 2006. "Numerical assessment of ejector operation for refrigeration applications based on cfd". *Applied Thermal Engineering,* **25**(5–6), pp. 604–612.

[10] Boncinelli, P., Rubechini, F., Arnone, A., M., C., and Cortese, C., 2004. "Real gas effects in turbomachinery flows: A computational fluid dynamics model for fast computations". *Journal of Turbomachinery,* **126**(2), pp. 268–286.

[11] Jassim, E., Abedinzadegan Abdi, M., and Muzychka, Y., 2008. "Computational fluid dynamics study for flow of natural gas through high-pressure supersonic nozzles: Part 1. real gas effects and shockwave". *Petroleum Science and Technology,* **26**, pp. 1757–1772.

[12] Pacheco, J., Fakhiry, S., Vezier, C., and Koch, J., 2013. "Lng propane compressor performance prediction and large scale test validation". *Proceedings of the 42nd Turbomachinery Symposium.*

[13] Thorley, A., and Tiley, C., 1987. "Unsteady and transient flow of compressible fluids in pipelines-a review of theoretical and some experimental studies". *International Journal of Heat and Fluid Flow,* **8**(1), pp. 3–15.

[14] Anderson, W., 1991. "Numerical study on using sulfur hexafluoride as a wind tunnel test gas". *AIAA Journal,* **29**(12), pp. 2179–2180.

[15] Turk, M., 2000. "Influence of thermodynamic behaviour and solute properties on homogeneous nucleation in supercritical solutions". *Journal of Supercritical Fluids,* **18**, pp. 169–184.

[16] Mohammadi, B., and Pironneau, O., 2004. "Shape optimization in fluid mechanics". *Annu. Rev. Fluid Mech.,* **36**, pp. 255–279.

[17] Jameson, A., and Reuther, J., 1994. "Control theory based airfoil design using the euler equations". *5th AIAA/USAF/NASA Symposium on Multidisciplinary Analysis and Optimization.*

[18] Kim, S., Alonso, J. J., and Jameson, A., 2004. "Multi-element high-lift configuration design optimization using viscous continuous adjoint method". *Journal of Aircraft,* **41**(5), pp. 1082–1097.

[19] Pierret, S., Coelho, R., and Kato, H., 2007. "Multidisciplinary and multiple operating points shape optimization of three-dimensional compressor blades". *Struct. Multidisc. Optim.,* **33**, pp. 61–70.

[20] Harinck, J., Pasquale, D., Pecnik, R., Buijtenen, J., and Colonna, P., 2013. "Performance improvement of a radial organic rankine cycle turbine by means of automated computational fluid dynamic design". *Proceedings of the Institution of Mechanical Engineers, Part A: Journal of Power and Energy,* **227**(6), pp. 637–645.

[21] Pini, M., Persico, G., and Dossena, V., 2014. "Robust adjoint-based shape optimization of supersonic turbomachinery cascades". *ASME Turbo Expo.*

[22] Pini, M., Persico, G., Pasquale, D., and Rebay, S., 2015. "Adjoint method for shape optimization in real-gas flow applications". *ASME J. Eng. Gas Turbines Power,* **137**(3).

[23] Fernandez, P., and Persico, G., 2015. "Automatic design of orc turbine profiles by using evolutionary algorithms". *ASME 3rd International Seminar on ORC power systems*.

[24] Persico, G., 2016. "Evolutionary optimization of centrifugal nozzles for organic vapours". *1st International seminar on Non Ideal Compressible Fluid Dynamics for Propulsion and Power*.

[25] Lian, Y., and Liou, M., 2005. "Multi-objective optimization of transonic compressor blade using evolutionary algorithm". *Journal of Propulsion and Power,* **21**(6), pp. 979–987.

[26] Luo, J., Zhou, C., and Liu, F., 2014. "Multipoint design optimization of a transonic compressor blade by using an adjoint method". *Journal of Turbomachinery,* **136**.

[27] Samad, A., and Kim, K., 2008. "Shape optimization of an axial compressor blade by multi-objective genetic algorithm". *Proceedings of the Institution of Mechanical Engineers, Part A: Journal of Power and Energy,* **222**(16), pp. 599–611.

[28] Samad, A., Kim, K., Goel, T., Haftka, R., and Shyy, W., 2008. "Multiple surrogate modeling for axial compressor blade shape optimization". *Journal of Propulsion and Power,* **24**(2).

[29] Quagliarella, D., 1998. "Genetic algorithms and evolution strategy in engineering and computer science: recent advances and industrial applications". *John Wiley & Son Ltd*.

[30] Peter, J., and Dwight, R., 2009. "Numerical sensitivity analysis for aerodynamic optimization: A survey of approaches". *Computer & Fluids,* **39**(3), pp. 373–391.

[31] Walther, B., and Nadarajah, S., 2015. "Adjoint-based constrained aerodynamic shape optimization for multistage turbomachines". *Journal of Propulsion and Power,* **31**(5).

[32] Rinaldi, E., Pecnik, R., and Colonna, P., 2014. "Exact jacobians for implicit navier-stokes simulations of equilibrium real gas flows". *Journal of Computational Physics,* **270**, pp. 459–477.

[33] Colonna, P., and Rebay, S., 2004. "Numerical simulation of dense gas flows on unstructured grids with an implicit high resolution upwind euler solver". *Int. J. Numer. Methods in Fluids,* **46**(7), pp. 735–765.

[34] Sagebaum, M., Albring, T., and Gauger, N. R., 2017. Codipack code differentiation package — scientific computing.

[35] Albring, T. A., Sagebaum, M., and Gauger, N. R., 2016. "Efficient aerodynamic design using the discrete adjoint method in su2". *17th AIAA/ISSMO Multidisciplinary Analysis and Optimization Conference*.

[36] Economon, D. T., Palacios, F., Copeland, S. R., Lukaczyk, T. W., and Alonso, J. J., 2015. "Su2: An open-source suite for multiphysics simulation and design". *AIAA Journal,* **54**(3), pp. 828–846.

[37] Vitale, S., Gori, G., Pini, M., Guardone, A., Economon, T. D., Palacios, F., Alonso, J. J., and Colonna, P., 2015. "Extension of the su2 open source cfd code to the simulation of turbulent flows of fluids modelled with complex thermophysical laws". *22nd AIAA Computational Fluid Dynamics Conference.*

[38] Giles, M. B., 1990. "Nonreflecting boundary conditions for euler equation calculations". *AIAA journal,* **28**(12), pp. 2050–2058.

[39] Giles, M., 1991. Unsflo: A numerical method for the calculation of unsteady flow in turbomachinery. Tech. rep., Cambridge, Mass.: Gas Turbine Laboratory, Massachusetts Institute of Technology,[1991].

[40] Saxer, A. P., 1992. A numerical analysis of 3-d inviscid stator/rotor interactions using non-reflecting boundary conditions. Tech. rep., Cambridge, Mass.: Gas Turbine Laboratory, Massachusetts Institute of Technology,[1992].

[41] Sederberg, T. W., and Parry, S. R., 1986. "Free-form deformation of solid geometric models". *ACM SIGGRAPH computer graphics,* **20**(4), pp. 151–160.

[42] Dwight, R. P., 2009. "Robust mesh deformation using the linear elasticity equations". *Computational Fluid Dynamics 2006*, pp. 401–406.

[43] Giles, M. B., and Pierce, N. A., 2000. "An introduction to the adjoint approach to design". *Flow, turbulence and combustion,* **65**(3-4), pp. 393–415.

[44] Griewank, A., and Walther, A., 2008. *Evaluating derivatives: principles and techniques of algorithmic differentiation.* SIAM.

[45] Bischof, C. H., Hovland, P. D., and Norris, B., 2008. "On the implementation of automatic differentiation tools". *Higher-Order and Symbolic Computation,* **21**(3), pp. 311–331.

[46] Colonna, P., Casati, E., Trapp, C., Mathijssen, T., Larjola, J., Turunen-Saaresti, T., and Uusitalo, A., 2015. "Organic rankine cycle power systems: From the concept to current technology, applications, and an outlook to the future". *ASME J. Eng. Gas Turbines Power,* **137**(10).

[47] Menter, F. R., 1993. "Zonal two equation k-ω turbulence models for aerodynamic flows". *24th AIAA Fluid Dynamics Conference.*

[48] Kraft, D., 1988. "A software package for sequential quadratic programming". *Forschungsbericht- Deutsche Forschungs- und Versuchsanstalt fur Luft- und Raumfahrt.*

[49] Denton, J. D., 1993. "Loss mechanisms in turbomachines". In ASME 1993 International Gas Turbine and Aeroengine Congress and Exposition, American Society of Mechanical Engineers, pp. V002T14A001–V002T14A001.

4

Extension and application of a RANS direct and adjoint solver for the analysis and design of 3D multi-stage turbomachinery

4.1   Introduction

The use of computational fluid dynamics (CFD) has become irreplaceable within the turbomachinery design process. CFD provides the aerodynamicist with information that, in the past, had to be obtained with limited, greatly more expensive, and time-consuming wind tunnel experiments. Thus, the use of CFD has resulted in a substantial performance enhancement of turbines and compressors. However, this progress has made increasingly difficult to achieve even better efficiency. In order to improve the efficiency of just a fraction of a percentage point, the designer has to take into account such a vast number of aspects that the problem can only be solved by coupling steady-state CFD simulations with numerical optimization techniques.

The simultaneous optimization of multiple blade rows allows to achieve better performance if compared to the solution that would be obtained by optimizing each row separately. Although gradient-free optimization methods may still be a viable option for 3D single blade-row fluid dynamic design,[1,2] adjoint methods are the only practical solution for multi-stage design because of the comparatively larger number of design variables.[3]

The adjoint method was first applied to compressible fluid-dynamic design problems by Jameson and Reuther in 1988,[4] and since then it has been extensively applied to external flow problems.[5–10] However, due to the additional complexity of deriving the adjoint equations for internal flow problems, in particular for what concerns the linearization of the inflow and outflow boundary conditions, the application of adjoint-based optimization to turbomachinery design is less widespread and scarcely documented in the literature.[3] Only in recent years a research effort has been made to extend the adjoint method for turbomachinery applications. Some works have documented adjoint methods for single-blade optimization,[11–19] and much fewer for multi-stage optimal designs.[20–23] In this case, the linearization of the mixing-plane interface is an additional challenge. Furthermore, nearly all the studies were restricted to the use of the constant eddy viscosity approximation[24] to avoid dealing with the differentiation of the turbulent transport equations.

The open-source CFD platform SU2[25] has recently gained recognition because of the implementation of a flexible, accurate, and efficient discrete adjoint (DA) solver.[26] The DA solver is automatically derived by means of advanced algorithmic differentiation (AD) techniques.[27] Various applications of this new design framework have been presented. *Albring et al.*[26] described an application of the SU2 DA solver to external aerodynamic problems; *Becket et al.*[29] showed the possibility of employing it for the design of wings taking into account aeroacoustic constraints; *Sanchez et al.*[30] used it for the solution aeroelasticity problems in aeronautics; *Vitale et al.*[31] employed the DA to show how the aerodynamic performance of single blade ORC turbine cascades can be improved, but limited to 2D test cases; finally, *Rubino et al.*[32] extended the DA solver in order to perform the unsteady optimization of 2D cascades using the harmonic balance method. However, although these last two efforts demonstrate the feasibility of deriving an accurate and efficient fully-turbulent turbomachinery adjoint within the SU2 design framework, yet the solution of industrially relevant problems requires the extension of those approaches to

handle 3D multi-stage turbomachinery.

Therefore, the work described here documents the extension and validation of the discrete adjoint solver of SU2 to 3D fully-turbulent multi-stage turbomachinery applications. In order to accomplish that, the SU2 RANS solver was first enriched with the implementation of a conservative and non-reflecting mixing-plane interface to perform accurate simulations of flows through three-dimensional multi-row geometries.[33] The DA solver was then obtained by differentiating the newly developed multi-domain RANS solver and the mixing-plane boundary conditions. Similarly to the work described in chapter 3, the method is based on the duality-preserving approach[26] obtained by reformulating the state constraint into a fixed-point problem. This results in an adjoint solver that inherits the same convergence properties of the primal solver.

In order to test the capabilities of the new design framework, the flow solver was first validated against the experimental results obtained from two conventional turbines whose test-cases where available in literature: the Aachen Turbine,[34] and the single-stage radial turbine of an Auxiliary Power Unit referred in this chapter as the APU turbine.[35] Secondly, the flow solver was also verified against experimental measurements performed on a small radial ORC turbine partially operating in the so-called NICFD regime. To the authors knowledge, this represents the first contribution to the open-literature in which a CFD solver is validated against measurements performed on a mini-ORC turbine. Finally, the adjoint solver, together with the entire optimization framework of SU2, was applied to re-design the Aachen turbine in order to demonstrate the unique capabilities of the automated design procedure.

This chapter is structured as follows. Section 4.2 focuses on the extension of the SU2 unstructured vertex-based RANS solver to accurately simulate 3D multi-stage turbomachinery. Section 4.3 describes the generalization of the adjoint equations for multiple flow domains. Section 4.4 reports a series of test-cases used to validate the solver by comparison with experimental data. Section 4.5 documents the re-design of the Aachen turbine using the newly developed discrete adjoint solver. Concluding remarks and future work are briefly discussed in Section 4.6.

4.2 Mixing-Plane Interface

4.2.1 Node ordering algorithm

The RANS flow solver of SU2 was extended to simulate multiple flow-domains via a mixing-plane interface in order to handle multi-stage turbomachinery design problem. The adoption of the mixing-plane approach required the implementation of a new data structure at the inflow and outflow boundaries in order to transfer the information from one domain to the other. This new data structure allows to access the mesh-nodes information in a span- and pitch-wise ordered manner. The span-wise ordering is necessary to impose the mixing-plane condition,[36] while both orderings are needed to compute the Fourier decomposition of the outgoing characteristic such that quasi-3D non-reflecting boundary conditions(NRBC) can be imposed.[37]

The new data-structure encodes the boundary node geometrical data in cartesian and cylindrical coordinates and contains the information of the particular turbomachinery configuration (i.e, axial and radial) under study. With these two pieces of information, the code automatically 1) selects the span-wise direction in which the mixing-plane layers are computed, and 2) computes the velocity components. For example, in an axial machine (see Fig. 4.1 left-side) the span-wise levels are computed along the radial coordinate (R), while the normal velocity component is parallel to the $z-$axis of rotation. Instead, for a radial cascade (see Fig. 4.1 right-side), the span-wise bands are computed along the $z-$axis and the normal velocity component is parallel to the radial direction.
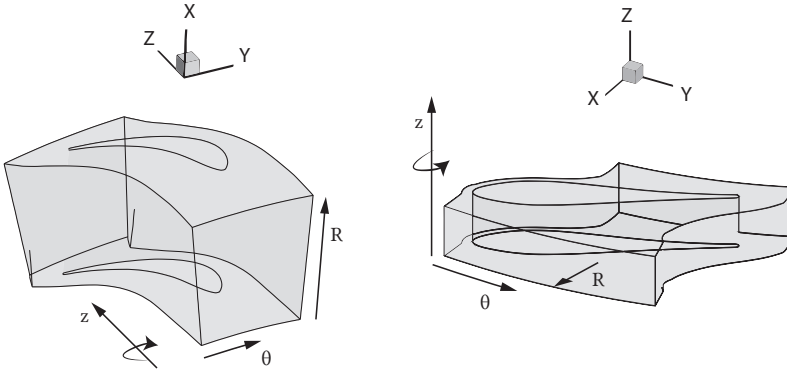

Figure 4.1: Axial and radial turbomachine flow domain example.

Figures 4.2 and 4.3 illustrate the fundamentals of the ordering algorithm. First, the number of span-wise bands in which a generic inflow or outflow boundary is discretized are automatically calculated from their intersection with a periodic boundary (cf. Fig. 4.2). Once the band levels are determined, the mesh-nodes are assigned to the closest band in a pitch-wise ordered manner (cf. Fig. 4.3).

4.2.2 Boundary condition specification

For each i-th node belonging to a specific band-level ζ, the characteristic jump is composed by an average and a harmonic component

$$\delta \mathbf{c}_{i,\zeta} = \delta \bar{\mathbf{c}}_{\zeta} + \delta \dot{\mathbf{c}}_{i,\zeta}. \tag{4.1}$$

The average component $\delta \bar{\mathbf{c}}_{\zeta}$ is the characteristic contribution that ensures that the flow quantities match at the interface. In order to achieve this objective, the average
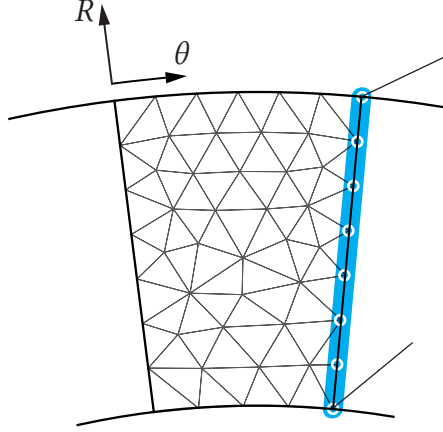
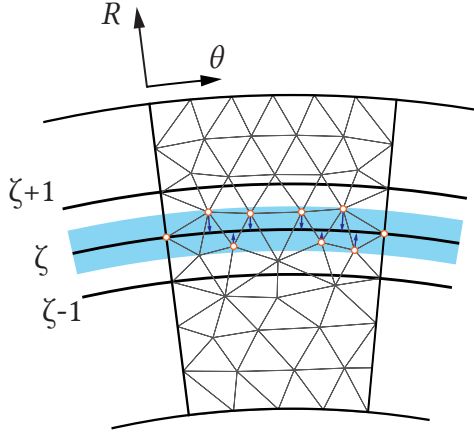Figure 4.2: Node ordering algorithm: computation of the span-wise bands.

Figure 4.3: Node ordering algorithm: allocation of the vertexes to the closest span-wise band.

characteristic jump at each band-level is computed as

$$
\left(\begin{array}{c} \delta \bar{c}_1 \\ \delta \bar{c}_2 \\ \delta \bar{c}_3 \\ \delta \bar{c}_4 \\ \delta \bar{c}_5 \end{array} \right)_\zeta = \left[\begin{array}{ccccc} -\bar{a}^2 & 0 & 0 & 0 & 1 \\ 0 & 0 & \bar{\rho}\bar{a} & 0 & 0 \\ 0 & 0 & 0 & \bar{\rho}\bar{a} & 0 \\ 0 & \bar{\rho}\bar{a} & 0 & 0 & 1 \\ 0 & -\bar{\rho}\bar{a} & 0 & 0 & 1 \end{array} \right]_\zeta \left(\begin{array}{c} \rho^{\text{donor}} - \bar{\rho}^{\text{target}} \\ v_{\text{n}}^{\text{donor}} - \bar{v}_{\text{n}}^{\text{target}} \\ v_{\theta}^{\text{donor}} - \bar{v}_{\theta}^{\text{target}} \\ v_{\zeta}^{\text{donor}} - \bar{v}_{\zeta}^{\text{target}} \\ p^{\text{donor}} - \bar{p}^{\text{target}} \end{array} \right)_\zeta , \qquad (4.2)
$$

where $(\bar{\rho}, \bar{\mathbf{v}}, \bar{p})$ are the primitive variables averaged at each span-wise level and $\bar{a}$ is the speed of sound; the target side of the interface is the side in which the boundary condition is actually imposed.

Since in most applications, especially in the presence of tip clearance, the target- and donor-side of the interface are discretized with a different number of span-wise levels, the donor quantities on the right hand side of Eq.(4.2) are computed using an interpolation algorithm. For example, using a linear interpolation algorithm (cf. Fig. 4.4), the donor average quantities used in Eq.(4.2) for the ζ-th band level, are computed using the average quantities of the $(\Psi - 1)$-th and Ψ-th band levels on the donor side.
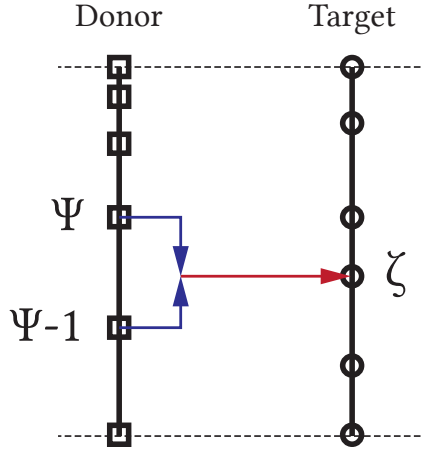

Figure 4.4: Schematic view of the interpolation approach used at the mixing-plane interface to transfer information from the donor- to the target-side.

Note that the current mixing-plane interface is conservative with respect to the mass, momentum and energy fluxes if and only if the primitive variables are averaged using the mixed-out procedure (cf. Section 3.2.1).

The harmonic component $\delta\dot{\mathbf{c}}_{i,\zeta}$ is calculated using the Quasi-3D approach of Saxer, [37] and it prevents the occurrence of non-physical wave reflections at boundaries. However, with respect to the original work of Saxer, a modification of the Fourier spatial decomposition is needed in order to take into account the data-structure of SU2.

According to the original work of Saxer, the discrete form of the spatial Fourier transform or a generic outgoing characteristic c_j can be computed as

$$\hat{c}_{j,k,\zeta} = \frac{1}{P} \sum_{i=0}^{n_\zeta - 1} c_{j,i,\zeta} e^{-\frac{2\pi i k}{P} y_i} \Delta y_i, \quad \text{with} \quad \left(-\frac{n_\zeta}{2} + 1 < k < \frac{n_\zeta}{2} - 1\right), \tag{4.3}$$

where P is the pitch length, n_ζ is the number of node per band, k is frequency, Δy_i,

$$\Delta y_i = y_i - y_{i-1} \quad \left(i = 1, 2, .., n_\zeta\right),$$ (4.4)

is the pitch-wise distance between two adjacent mesh-nodes of the same band, and y_i,

$$y_i = \sum_{m=1}^{i} \Delta y_m \quad \text{with} \quad \left(i = 1, 2, .., n_\zeta\right),$$ (4.5)

is the cumulative pitch-wise length. However, in the case of unstructured grids, the nodes belonging to the same band do not lay at the same span-wise distance (cf. Fig. 4.3); thus, the computation of the pitch-wise distance between to adjacent nodes becomes meaningless.

A more general formulation can be instead obtained by using the coordinate transformation

$$\theta_i = \frac{y_i}{R_i}$$ (4.6)

where θ_i, is the cumulative angular distance that can be computed as

$$\theta_i = \sum_{m=1}^{i} \Delta\theta_m \quad \text{with} \quad \left(i = 1, 2, .., n_\zeta\right),$$ (4.7)

and $\Delta\theta_i$ is the angular distance between two adjacent nodes

$$\Delta\theta_i = \theta_i - \theta_{i-1} \quad \left(i = 1, 2, .., n_\zeta\right).$$ (4.8)

Using this transformation, Eq. (4.3) can be re-formulated as

$$\hat{c}_{j,k,\zeta} = \frac{1}{P} \sum_{j=0}^{n-1} c_{j,i,\zeta} e^{-\frac{2\pi i k}{P} R_i \theta_i} R_i \Delta\theta_i, \quad \text{with} \quad \left(-\frac{n_\zeta}{2} + 1 < k < \frac{n_\zeta}{2} - 1\right).$$ (4.9)

However, since the difference in span-wise coordinate among the nodes of the same band is in general negligible if compared to the pitch wise length, the dependence of Eq. (4.3) from R_i can be eliminated, and thus Eq. (4.3) simplifies into

$$\hat{c}_{j,k,\zeta} = \frac{1}{\theta_{\text{pitch}}} \sum_{i=0}^{n_\zeta-1} c_{j,i,\zeta} e^{-\frac{2\pi i k}{\theta_{\text{pitch}}} \theta_i} \Delta\theta_i \quad \text{with} \quad \left(-\frac{n_\zeta}{2} + 1 < k < \frac{n_\zeta}{2} - 1\right).$$ (4.10)

The schematic difference between the two approaches is illustrated in Fig. 4.5. When unstructured grids are used, the points belonging to the same band-level are all projected to the same radial distance. This approximation is not needed when structure grids are employed. The Fourier decompositions of all the outgoing characteristics of a specific boundary are first linearly combined (according to the 2D non reflecting theory), and then
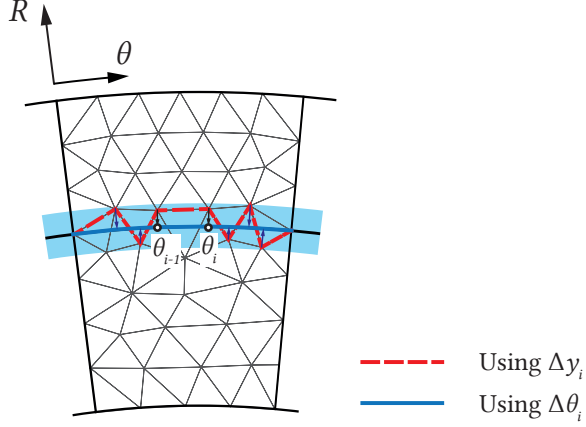
Figure 4.5: Schematic illustration of the distance between adjacent nodes using both approaches.

transformed back into the spatial domain. The result of this procedure gives the harmonic component of Eq. (4.1).

Once both the average and the harmonic component have been computed, the change of the characteristic variables $\delta \mathbf{c}_{i,\zeta}$ is finally converted into a primitive variable perturbation, as illustrated in Section 3.2.1. The overall procedure is repeated for all the span-wise levels of the boundary.

4.3 Discrete Adjoint Solver for Multiple-Flow Domains

The discrete adjoint method applied to multi-stage turbomachinery problems involves the generalization of the discrete adjoint equations for single flow domain to multiple domains, coupled through a steady mixing-plane interface. Following Section 3.3, let J be the objective function of a multi-stage turbomachinery design problem in which the flow solution is obtained by solving the RANS equations on N multiple-flow domains. Assume that the goal of the optimization problem is to find the minimum of the objective function. If the mesh and surface deformation are performed with linear elasticity equations [38] and free-form deformation algorithm, [39] the optimization problem can be written as

$$\min_{\mathbf{D}} \quad J\left[\mathbf{U}_1\left(\mathbf{D}\right), \mathbf{X}_1\left(\mathbf{D}_1\right), ..., \mathbf{U}_N\left(\mathbf{D}\right), \mathbf{X}_N\left(\mathbf{D}_N\right)\right], \tag{4.11}$$

$$\text{s.t.} \quad \mathbf{U}_k = \mathbf{G}_k\left(\mathbf{U}, \mathbf{X}_k\right), \quad \text{with} \quad k = 1, 2, ..., N, \tag{4.12}$$

$$\mathbf{X}_k = \mathbf{M}_k(\mathbf{D}_k), \quad \text{with} \quad k = 1, 2, ..., N, \tag{4.13}$$

with

$$\mathbf{D} = \{\mathbf{D}_1, \mathbf{D}_2, ..., \mathbf{D}_N\}, \tag{4.14}$$

$$\mathbf{U} = \{\mathbf{U}_1, \mathbf{U}_2, ..., \mathbf{U}_N\}. \tag{4.15}$$

$\mathbf{D}_k$ represents the design variables used to deform the blade in the k-th domain, and $\mathbf{U}_k$ and $\mathbf{X}_k$ are the respective flow solution and mesh of the same domain. While $\mathbf{X}_k$ depends only on the design variables that act on the k-th domain, $\mathbf{U}_k$, as shown in Eq. (4.12), is influenced by the solutions of the other flow domains through the mixing-plane interface and, as such, by the entire vector of design variables ($\mathbf{D}$). As for the single flow domain case (cf. Section 3.3), $\mathbf{M}_k$ is a linear function which represents the mesh and surface deformation, while $\mathbf{G}_k$ is the flow solver iteration. Differently from the single flow domain case, N constraints on the flow solution, Eq. (4.12), and on the surface and volume deformation iterative process, Eq. (4.13), must be imposed to ensure that convergence is reached in any of the flow domains for both the flow solver and the mesh deformation process.

The Lagrangian associated to this problem can be then expressed as

$$L(\mathbf{D}, \mathbf{U}, \mathbf{X}, \bar{\mathbf{U}}, \bar{\mathbf{X}}) = J(\mathbf{U}, \mathbf{X}) + [\mathbf{G}_1(\mathbf{U}, \mathbf{X}_1) - \mathbf{U}_1]^T \bar{\mathbf{U}}_1 + ... + [\mathbf{G}_N(\mathbf{U}, \mathbf{X}_N) - \mathbf{U}_N]^T \bar{\mathbf{U}}_N$$
$$+ [\mathbf{M}_1(\mathbf{D}_1) - \mathbf{X}_1]^T \bar{\mathbf{X}}_1 + ... + [\mathbf{M}_N(\mathbf{D}_N) - \mathbf{X}_N]^T \bar{\mathbf{X}}_N, \tag{4.16}$$

where $\bar{\mathbf{X}}_k, \bar{\mathbf{U}}_k$ are arbitrary Lagrange multipliers. Differentiating L with respect to each $\mathbf{D_k}$, and by choosing each $\bar{\mathbf{X}}_k$ and $\bar{\mathbf{U}}_k$ in such a way that the terms $\frac{\partial \mathbf{U}_i}{\partial \mathbf{D}_k}$ and $\frac{\partial \mathbf{X}_i}{\partial \mathbf{D}_k}$ can be eliminated, leads to N adjoint equations

$$\bar{\mathbf{U}}_k = \frac{\partial}{\partial \mathbf{U}_k} J^T(\mathbf{U}, \mathbf{X}) + \sum_{i=1}^{N} \frac{\partial}{\partial \mathbf{U}_k} \mathbf{G}_i^T(\mathbf{U}, \mathbf{X}_i)\bar{\mathbf{U}}_i, \quad \text{with} \quad k = 1, 2, ..., N, \tag{4.17}$$

and to N mesh sensitivity equations

$$\bar{\mathbf{X}}_k = \frac{\partial}{\partial \mathbf{X}_k} J^T(\mathbf{U}, \mathbf{X}) + \frac{\partial}{\partial \mathbf{X}_k} \mathbf{G}_k^T(\mathbf{U}, \mathbf{X}_k)\bar{\mathbf{U}}_k, \quad \text{with} \quad k = 1, 2, ..., N. \tag{4.18}$$

Once all the adjoint solutions $\bar{\mathbf{U}}_k$ have been computed, the mesh node sensitivity at each flow domain $\bar{\mathbf{X}}_k$ is computed by evaluating Eq. (4.18), and, finally, the N total derivatives of J with respect to the design variables of each k-th domain are given by

$$\frac{\mathrm{d}J}{\mathrm{d}\mathbf{D}_k}^T = \frac{\mathrm{d}}{\mathrm{d}\mathbf{D}_k}\mathbf{M}_k^T(\mathbf{D}_k)\bar{\mathbf{X}}_k, \quad \text{with} \quad k = 1, 2, ..., N. \tag{4.19}$$

As for the method described in Section 3.3, the derivatives $\frac{\partial \mathbf{J}}{\partial \mathbf{U}_k}, \frac{\partial \mathbf{J}}{\partial \mathbf{X}_k}, \frac{\partial \mathbf{G}_i}{\partial \mathbf{U}_k}, \frac{\partial \mathbf{G}_k}{\partial \mathbf{X}_k}$, and $\frac{\mathrm{d}\mathbf{M}_k}{\mathrm{d}\mathbf{D}_k}$ are computed by resorting to the reverse mode of the open-source Algorithmic Differentiation tool CodiPack.[26,27]

4.4 Validation of the RANS solver

The newly developed RANS solver for internal compressible flows applicable to turbo-machinery was validated by comparing simulation results to experimental data related to two turbine test cases documented in the literature. The first test-case considered is referred to as Aachen turbine and consists of a one-and-half stage of an axial turbine that was conceived and realized in order to provide data-sets for turbomachinery code validation. [34] The second test case is a single-stage radial turbine of an Auxiliary Power Unit, here referred to as the the APU turbine. [35] The third validation test-case is a single-stage radial ORC turbine designed for small scale applications; [40] thus it will be referred in the following as the Mini ORC Turbine.

4.4.1 Aachen Turbine

The three flow-domains of the Aachen turbine (i.e., stator1, rotor1, stator2) were discretized using structured grids generated with a well known commercial software. [41] The grid is composed by a total amount of five million elements. The turbulence effects are modeled using the k-ω SST turbulence model [42] and a full resolution of the boundary-layer was obtained by ensuring wall $y+ < 1.0$ at the blades and at the hub and shroud surfaces. The span-wise values of the quantities imposed as boundary conditions at the inlet of the first stator (i.e, total pressures, total temperatures, flow directions) and at the outlet of the second stator (static pressures) are the one corresponding to the reported experimental data with lower mass-flow rate. [34]

The convective terms are discretized using a Roe upwind scheme [43] for which second-order accuracy is achieved with the MUSCL reconstruction, while the viscous terms are discretized using the Average-Gradient formulation. For both fluxes, the gradients are evaluated using a Least-Squares method. [44] A convergence rate of six order of magnitude on both the flow and turbulent quantities was achieved in 2000 iterations using an Euler implicit time-marching scheme with a CFL of 20 without multi-grid.

Figure 4.6 shows the entropy distribution on different secondary planes in the stream-wise direction. As expected, the larger entropy generation occurs on the suction side of each blade rows. The appearance of the tip clearance vortex at the tip of the rotor cascade is also evident. Although the tip-vortex is averaged out by the mixing-plane interface between the rotor and the second stator, the span-wise flow distribution at the inlet of the second stator remains highly non-uniform, resulting in larger secondary flow losses if compared to the ones occurring in the first row.

Table 4.1 shows that the mixing-plane algorithm, implemented following the method described in section 4.2, is capable to conserve the overall fluxes across the two interfaces. The fluxes are conserved even along the span-wise direction, proving the full conservative property of the mixing-plane method.

The results obtained with SU2 were compared to the experimental data and to the flow simulations results obtained with other RANS solvers (i.e., TFLOW, 3DFLOW, APNASA-V5) reported in the work of *Yao et al.* [45] Figures 4.7 and 4.8 show the absolute flow angle and total-pressure span-wise distributions predicted by all these CFD
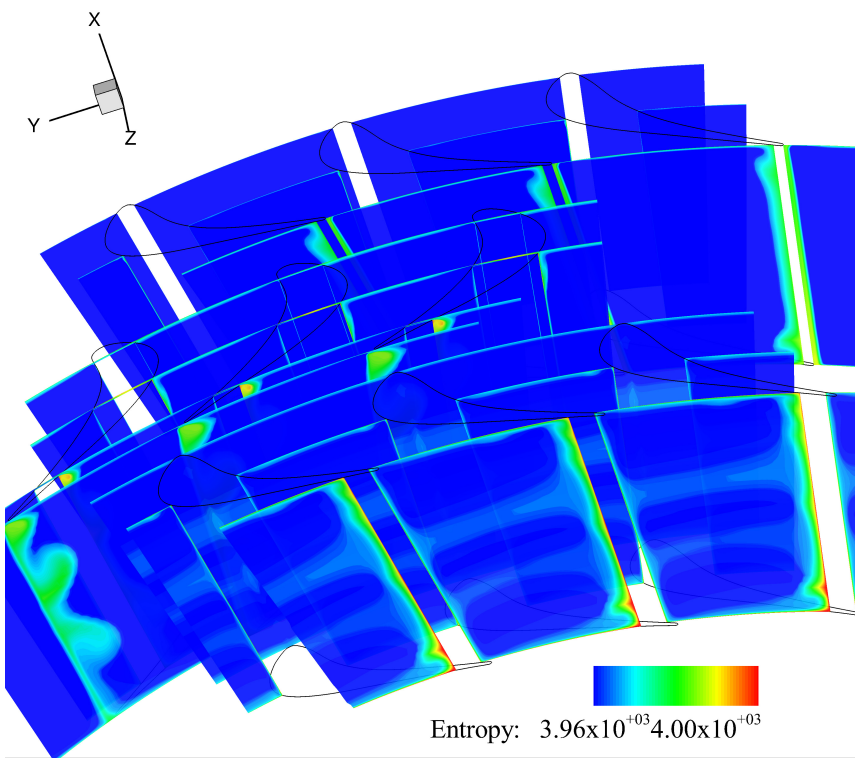
Figure 4.6: Entropy contour of the Aachen turbine.

Fluxes rel. err.	stator1-rotor	rotor-stator2	
F_ρ	8.8E-04	9.2E-04	[-]
F_{v_n}	2.0E-05	8.2E-06	[-]
F_{v_t}	8.6E-04	1.6E-03	[-]
F_k	3.5E-03	4.8E-03	[-]
F_ω	1.5E-03	1.2E-02	[-]

Table 4.1: Fluxes relative error across the mixing-plane stotor-rotor and rotor-stator interfaces.

tools and those measured at the interface between the rotor and second stator. Figures 4.9 and 4.10 display the same quantities at the outlet section of the second stator. It can be observed that SU2 predictions are generally in good agreement with the quantities calculated with the other flow solvers for what concerns the flow angle distribution, whilst are closer to the experimental data with regard to the span-wise trend of the total pressure.
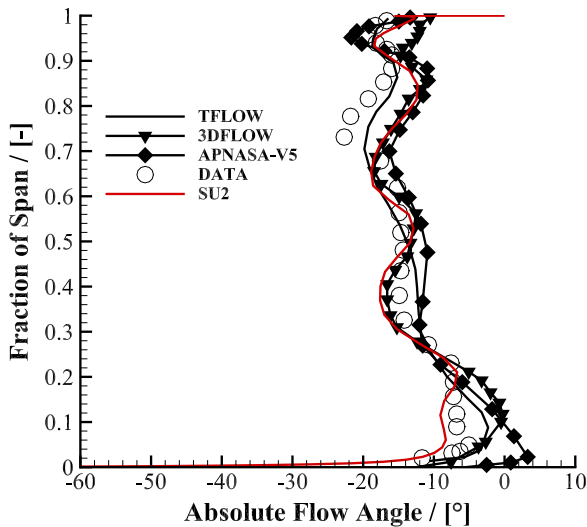
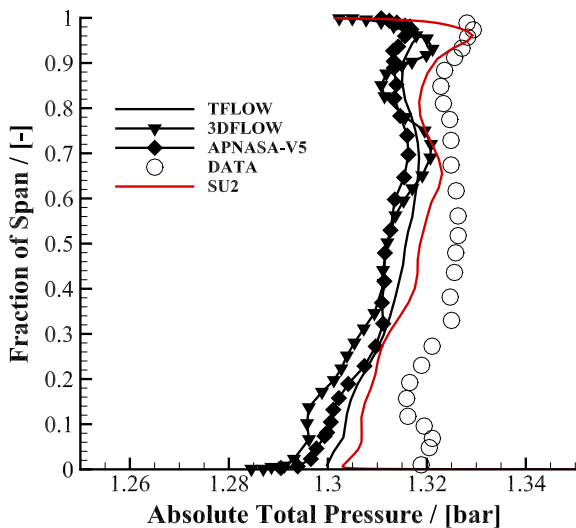Figure 4.7: Absolute Flow Angle at rotor-stator interface

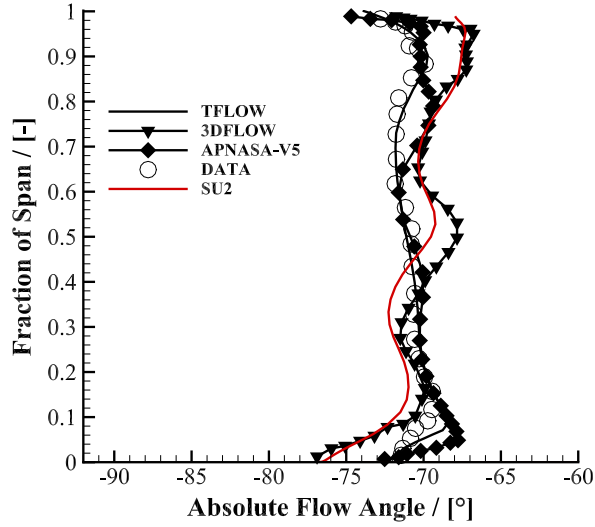Figure 4.8: Total pressure at rotor-stator interface.

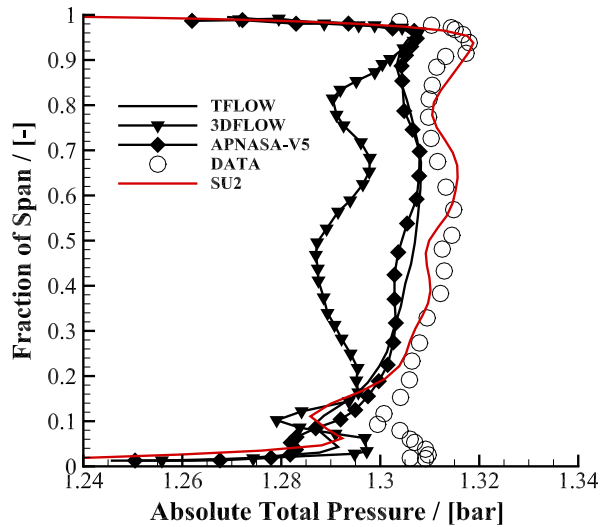Figure 4.9: Absolute Flow Angle at the outlet section of the second stator.

Figure 4.10: Total pressure at the outlet section of the second stator.

4.4.2 APU Turbine

The geometry of the APU turbine was reconstructed using the information available in Sauret[46] and adopting the method proposed by Verstraete.[47] Since no information was given with respect to the shape of the spinner, an elliptical spinner was utilized because it facilitates the convergence of the simulations. Figure 4.11 shows the meridional section of the turbine.

The three flow domains (i.e., stator, rotor and diffuser) were discretized using structured grids for a total amount of three million elements. The selected turbulence model was the k-ω SST,[42] and y+ < 1.0 was ensured at the wall boundaries. The boundary conditions selected for this test case are the one corresponding to the 5.7 pressure-ratio of the experimental campaign[35] and are shown in Table 4.2. The convective terms were

$T_{\text{tot,in}}$	477.6	[K]
$p_{\text{tot,in}}$	413.6	[kPa]
β_{in}	0.0	[°]
p_{out}	72.4	[kPa]
Ω	71700	[rpm]
$I_{\text{tur,in}}$	0.05	[-]
$\left(\frac{\mu_{\text{tur}}}{\mu_{\text{lam}}}\right)_{\text{in}}$	100.0	[-]

Table 4.2: Inlet and outlet boundary conditions values for the APU turbine test-case.

discretized using a second-order Roe upwind method whereby the monotonicity of the scheme is ensured by applying the Van Albada limiter.[48] The viscous terms are discretized using the Average-Gradient formulation and the gradients are computed using a Least-Squares method. A reduction of five orders of magnitude on both the flow and turbulent residuals was obtained in 3000 time-steps using an implicit Euler scheme with a CFL number of 20. To guarantee a smooth convergence, the rotational speed was linearly increased from zero to the final value during the first 500 iterations.

The entropy contours at different streamwise locations are shown in Fig. 4.12. As expected, the highest fluid-dynamic losses take place on the suction side of the rotor due to the presence of a large tip-clearance vortex. The intensity of the vortex is then dissipated within the diffuser generating additional mixing losses. Additionally, a large area of flow separation is visible at the center of the diffuser because of the abrupt increase of passage area.

The variation of the total to static efficiency with respect to the rotational speed for a constant expansion ratio value is shown in Fig. 4.13. The CFD results were obtained by varying the rotational speed from 85% to 110% of its nominal value which corresponds to a specific speed of $u/v_{\text{ax}} = 0.7$. The results show that SU2 is capable of reproducing the experimental trend and of correctly computing the point of maximum efficiency, which corresponds to $u/v_{\text{ax}} = 0.75$. An absolute difference which varies from 0.5% to
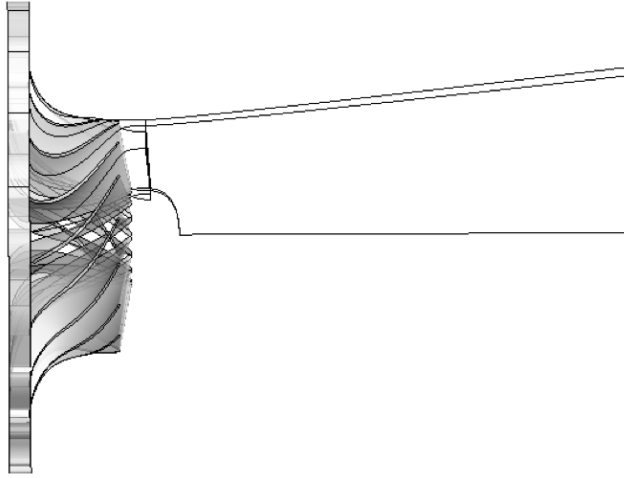
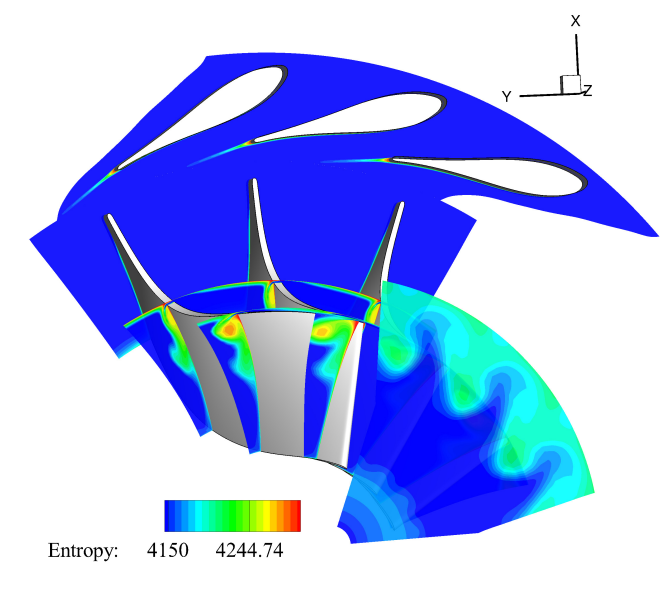Figure 4.11: Meridional view of the APU turbine.

Figure 4.12: Entropy contour of the APU turbine.

around 2% is observed between the measurements and the CFD predictions. This deviation monotonically increases going from lower to higher specific speeds. This can be arguably attributed to the averaging of quantities which is inherent to the modeling of the rotor-stator flow interface by means of the mixing-plane method. As shown in Fig. 4.14, at lower specific speeds the flow becomes highly transonic and comparatively more non-uniform at the outlet of the stator. The use of the mixing-plane interface results in the simulation of a less dissipative flow, leading to the calculation of a higher rotor performance and eventually to the over-estimation of the turbine total-to-static efficiency, especially at lower specific speed. Similar conclusions about the diffusivity of the mixing-plane interface in the presence of transonic flows are also reported in other works in the literature.[49] The accuracy of the flow solver of SU2 is also confirmed by the comparison of the averaged flow kinematic quantities measured and computed at the stator and rotor outlet sections (cf. Table 4.3).
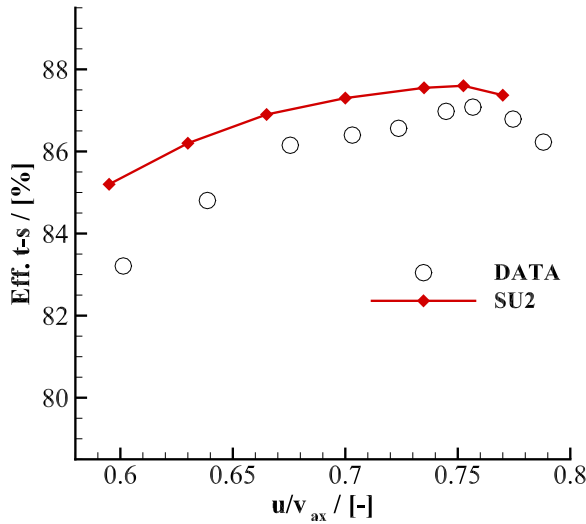

Figure 4.13: Comparison between numerical and experimental data of the total static efficiency of the machine for different rotational speeds.

Finally, Fig. 4.15 shows the comparison between the numerical and experimental values of the absolute flow angle along the span-wise direction at the inlet section of the diffuser. Overall, the CFD results are in accordance with the experimental trend with the exception of the tip region. In absence of additional information on measurements uncertainty, the results are deemed satisfactory for the purpose of this study.
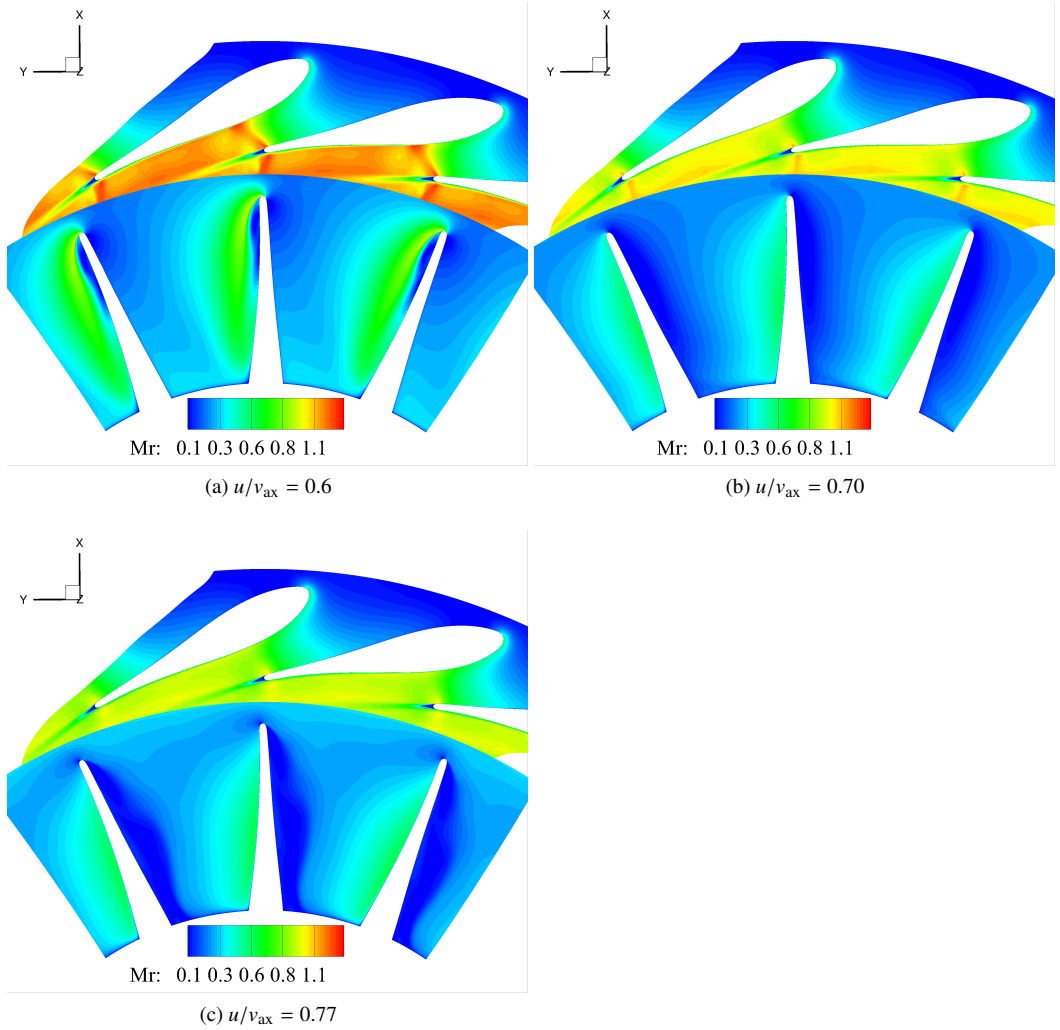
(a) $u/v_{ax} = 0.6$

(b) $u/v_{ax} = 0.70$

(c) $u/v_{ax} = 0.77$

Figure 4.14: Mach number contour at the stator-rotor interface of the APU turbine for different rotational.

	DATA	SU2	err. [%]
$\alpha_{\text{out,stator}}[°]$	77.7	77.9	0.02
$M_{\text{out,stator}}[-]$	0.985	0.982	0.3
$\beta_{\text{out,rotor}}[°]$	56.1	56.8	1.2
$Mr_{\text{out,rotor}}[-]$	0.71	0.72	1.4

Table 4.3: One-dimensional averaged kinematic quantities at the stator and rotor outlet sections.
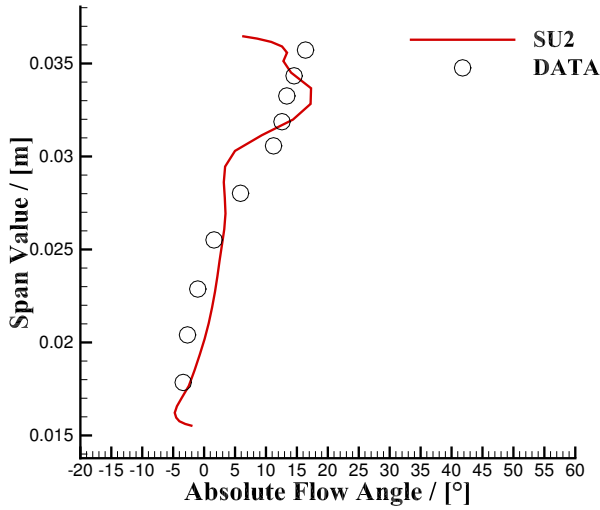

Figure 4.15: Comparison between numerical and experimental data of the absolute flow angle along the span-wise direction at the outlet section of the rotor.

4.4.3 Mini ORC Turbine

The geometry and experimental results of the Mini ORC Turbine test-case were provided to the Propulsion & Power group of Delft University of Technology by an industrial partner for the purpose of validating the SU2 flow solver in case of NICFD turbomachinery applications. The geometry together with the experimental results and boundary conditions of the turbine are confidential; thus, certain information in the description of this test case is omitted, and the results presented are all scaled by means of undisclosed factors.

The machine is a radial inflow ORC turbine operating with an organic compound as working fluid. The flow simulation encompasses three single-passage domains, namely a stator, a rotor and a rectilinear outlet region; the turbine was discretized using structured grids. The selected turbulence model was the k-ω SST,[42] and $y+ < 1.0$ was ensured at the wall boundaries. Given the highly supersonic flow regime on both the stator and the rotor blade and the severe flow separations on the rotor blade arguably due to sub-optimal impeller blade design, a fully converged steady-state solution was obtained by using first-order upwind generalized Roe for the convective terms (cf. Sec. 2.4) while second-order accuracy was maintained for the viscous terms. Mesh independence studies resulted in a grid composed by about 5 million elements (1.5 million for the stator, 3 million for the rotor, 500k for the outlet). Thermodynamic quantities are computed using the Peng-Robinson equation of state (cf. Sec. 2.8). A reduction of five orders of magnitude on both the flow and turbulent residuals was obtained in 5000 time-steps using an implicit Euler scheme with a CFL number of 10. To guarantee a smooth convergence, the rotational speed was linearly increased from zero to the final value during the first 1500 iterations.

Figure 4.16 shows the mach contours at different streamwise locations for the turbine working in nominal condition ($\Omega = 1$). As evident, a large region of flow separation occurs at the inlet of the rotor due to incidence effects. The misalignment between the flow angle and the blade inlet angle along with the blunt shape of the leading edge causes an expansion fan on the front suction side of the impeller followed by a shock wave.

Figure 4.17 shows the variation of the normalized efficiency with respect to the normalized rotational speed for a constant expansion ratio; reported values are calculated from simulations and from measurements for comparison. The Mach contours associated to the four validation points are shown in Fig. 4.18. The results show that SU2 is capable of reproducing the measured trend and of correctly predicting the point of maximum efficiency. However, a deviation of few percentage points is observed between the experimental and the CFD results. The deviation may be attributed to the use of the first order approximation for the discretization of the convective terms. In absence of additional information on measurements uncertainty, the results are deemed satisfactory and document, to the knowledge of the authors for the first time in the open-literature, that standard RANS CFD solvers equipped with specialized numerical schemes and sufficiently accurate fluid thermo-physical models can be used to predict the fluid-dynamic performance of mini-ORC turbines.
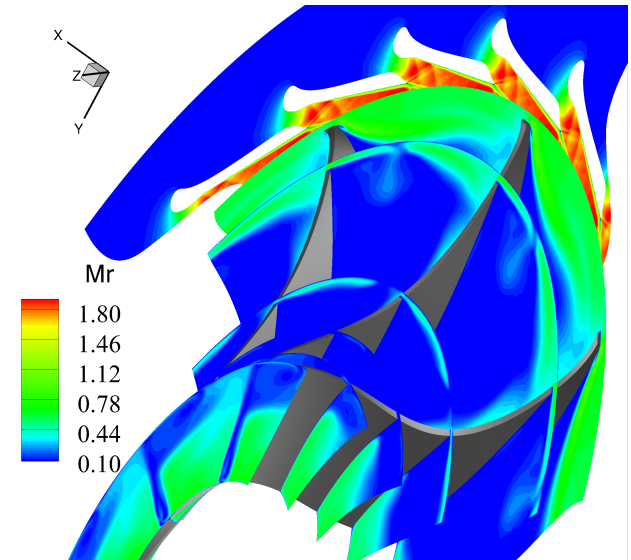
Figure 4.16: Mach contour of the Mini ORC turbine.
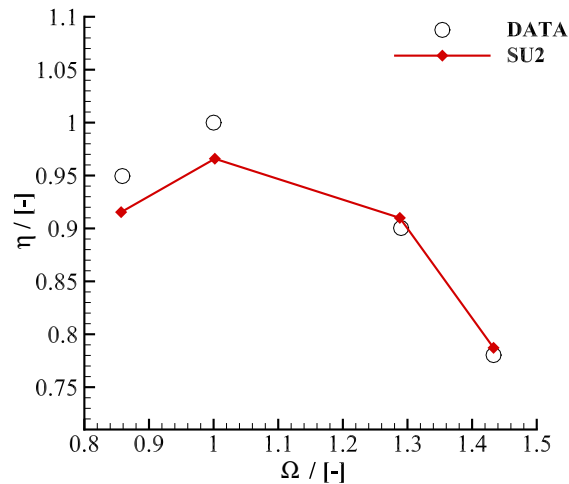

Figure 4.17: Comparison between numerical and experimental data of the efficiency of the machine for different rotational speeds.

(a) $\Omega = 0.86$

(b) $\Omega = 1.0$

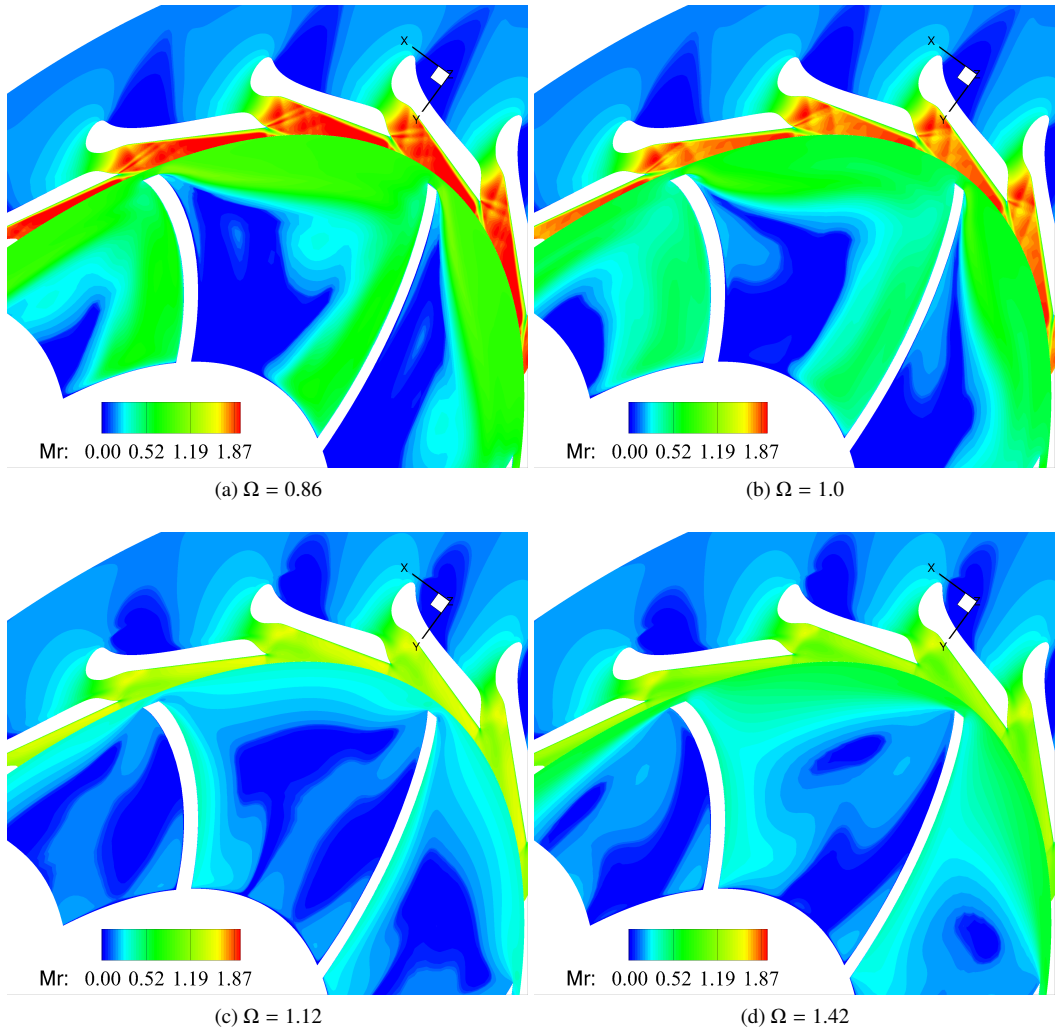(c) $\Omega = 1.12$

(d) $\Omega = 1.42$

Figure 4.18: Mach number contour at the stator-rotor interface of the Mini ORC Turbine for different rotational speeds.

4.5   Application of the RANS Adjoint solver

The capabilities of the multiple flow domains RANS adjoint solver described in Section 4.3 were preliminarily assessed by performing a paradigmatic exercise: the numerical optimization of the fluid dynamic performance of the Aachen turbine. First, the gradient validation is documented: the adjoint sensitivities of the objective function are compared with that calculated with finite differences (FD). The results of optimization are then presented. Finally, the impact of the Constant Eddy Viscosity (CEV) approximation on the accuracy of the gradient is reported and discussed.

4.5.1   Aachen Optimization

In order to improve the performance of the Aachen turbine, the entropy-generation, defined as

$$s_{\text{gen}} = \frac{T_{\text{tot,in}}}{v_{\text{spout}}^2} \sum_{k=1}^{3} (s_{\text{out}} - s_{\text{in}})_k \,, \tag{4.20}$$

was minimized under the constraint that the shaft power is kept constant, together with the outlet flow angle of the second stator. The constraint on the flow angle ensures that the optimizer does not converge on a solution in which the second stator is flattened.

Since the purpose of this study is just to prove the capability of the optimization framework, a coarser mesh was adopted in order to reduce the computational cost. The new mesh comprises 600k grid-points with no boundary-layer discretization at the shroud and the hub surfaces. Consequently, a free-slip boundary condition was applied to the end-walls. Except for this, the other boundary-conditions and all the other options were kept the same as for the validation of the RANS flow solver described in section 4.4.1.

The deformation of the blades was obtained using as a design variables the tangential displacement of the control-points of three cylindrical FFD boxes (one box per blade), as can be seen in Fig. 4.19. The FFD boxes used for the optimization are of degree 6 in both the tangential and axial direction and degree 3 in the radial direction. This results in a total amount of 588 design-variables (196 per each blade). To avoid unfeasible designs, the trailing-edges were excluded from the FFD boxes. Nonetheless, continuity up to the second-order derivative was guaranteed at the intersection between the blade and the boxes.

With regard to computational cost, it was found that the run-time per iteration of the adjoint solver is on average 30% higher than the one of the direct solver, and it required about four times more memory usage.

4.5.1.1   Gradient Validation

The validation of the gradient for all the 588 design variables is computationally prohibitive because it requires 589 solutions of the direct solver to compute the sensitivity using first-order finite-difference scheme. Therefore, the sensitivity is validated with respect to the control points of three FFD boxes of degree one in each direction. This
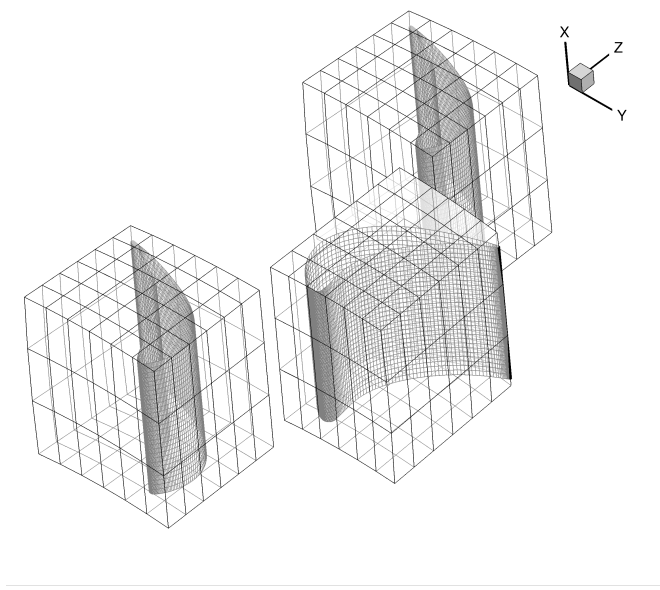
Figure 4.19: FFD boxes Aachen test case.

corresponds to 24 design variables in total (8 for each blade). Furthermore, since the discrete-adjoint algorithm is independent from the parameter with respect to which the sensitivity is computed (as described in section 4.3), the validation process is hereafter presented only for the entropy generation parameter. Finally, a step-size equal to 1E-05 was used for the finite difference algorithm.

Figure 4.20 shows the convergence history of the density adjoint residuals, $\mathbf{R}_{\rho,k}$, for each flow domain and the convergence of the overall geometrical sensitivity, computed as

$$\phi = \sum_{k=1}^{3} \left\| \bar{\mathbf{X}}_{k,\text{blade}} \right\|$$

(4.21)

where $\bar{\mathbf{X}}_{k,\text{blade}}$ is the mesh sensitivity projected over the blade surface of each row. The overall geometrical sensitivity, although the adjoint residuals only drops of about 3 orders of magnitude, converges rapidly to its final value. The calculation of ϕ at each iteration is computationally demanding, since it requires the evaluation of Eq. (4.18) at each time-step. Hence, ϕ is calculated only at certain time-steps (in this case every 200 iterations) only for the sake of monitoring the gradient convergence.

As depicted in Fig. 4.21, the gradient of the entropy generation provided by the discrete adjoint very accurately correlates with the one obtained with finite-differences. This confirms that all the components of the RANS flow solver and mesh deformation routines
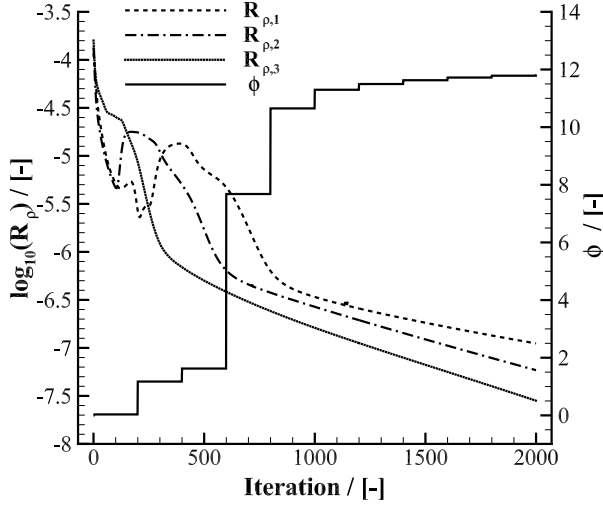
Figure 4.20: Convergence history RANS Adjoint Solver for the Aachen Turbine test-case.

(cf. Section 4.3) were correctly differentiated, including the turbulence model and the mixing-plane boundary conditions.

4.5.1.2 Optimization

The normalized optimization history in Fig. 4.22 shows that the SLSQP[50] algorithm converges in 10 iterations, achieving a total entropy generation reduction of 12%, while the total-to-total efficiency increases by as much as 3%. The equality constraints of power and outlet flow angle are satisfied with differences of 0.4% and 0.05% with respect to their prescribed values.

Figure 4.23 depicts the span-wise distribution of the entropy generation performance parameter for each row for both the baseline and the optimal geometry. The figure shows that the optimization algorithm enables to reduce the fluid-dynamic losses along the entire span of each blade. The span-wise flow deflections of the optimal and baseline blades are presented in Fig. 4.24; both the optimal and the baseline turbine configuration feature a monotonic decrease of the blade-loading along the span-direction. In spite of the increased blade loading, the optimal rotor and second-stator exhibit lower fluid-dynamic losses.

The two-dimensional sections of the blades at the hub, mid, and shroud for both the optimal (red) and the baseline (black) are presented in Fig. 4.25. In each of the rows, the optimal solution contains more slender blade profiles, which led to a reduction of profile losses. In addition, the optimal blades are more slender along the blade span. This trend is
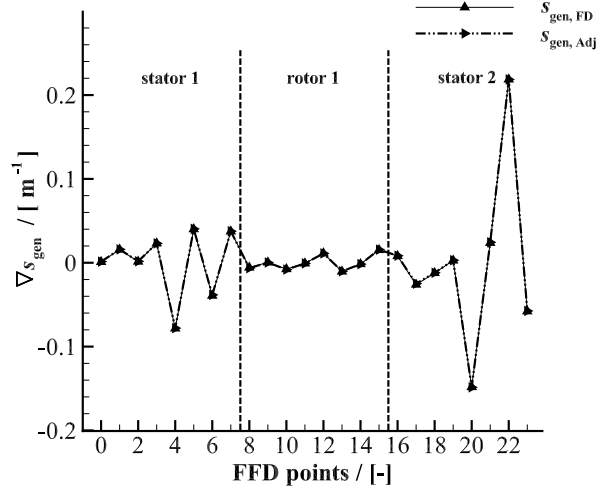
Figure 4.21: Validation of the entropy generation gradient obtained with the discrete adjoint against the one computed with the finite-difference scheme for the Aachen Turbine.
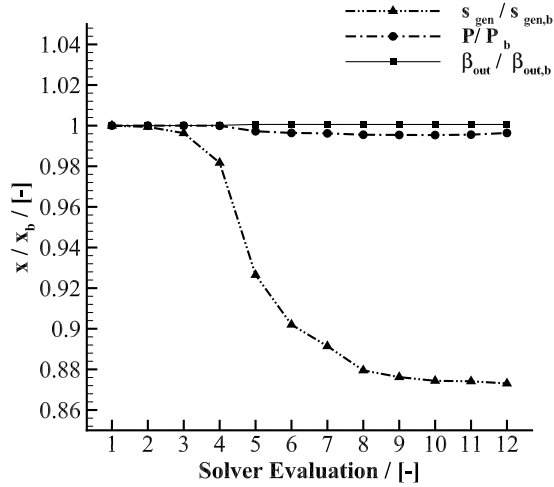

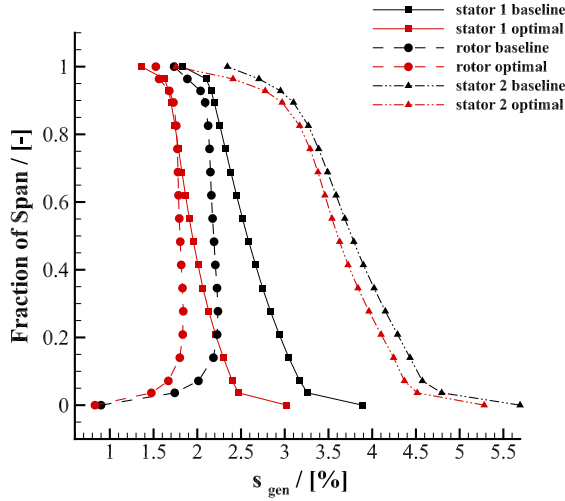Figure 4.22: Optimization history for the Aachen Turbine test-case.

Figure 4.23: Span-wise value of the entropy generation parameter computed for each row for both the optimal (red) and the baseline (black) geometries.
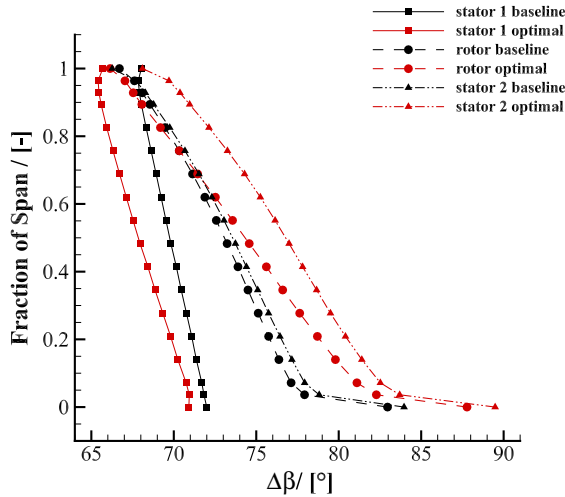
Figure 4.24: Span-wise value of the flow deflection of each blade-row for both the optimal (red) and the baseline (black) geometries.

more pronounced for the rotor and second stator blades as they present a larger difference in blade-loading along the span. Finally, the integral view of the 3D optimal and baseline blade shapes are shown in Fig. 4.26.

Figure 4.25: Comparison of the 2D sections at the hub, mid, and shroud span of the optimal blade shapes (red) with respect to the baseline geometries (black). The baseline is represented by one single continuous black line as the blades are prismatic.

Figure 4.26: Comparison between the optimal 3D blade shapes (red) and the baseline geometries (black).

4.5.2 Assessment of the Constant Eddy Viscosity approximation

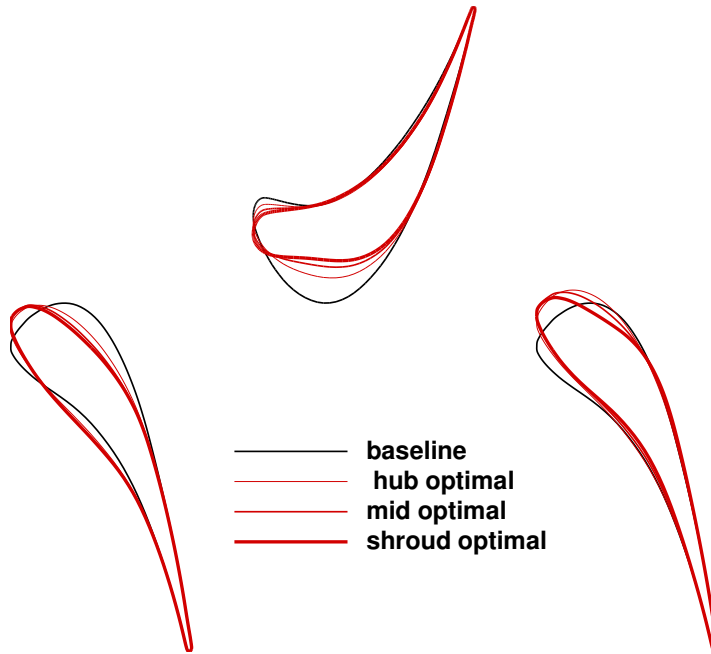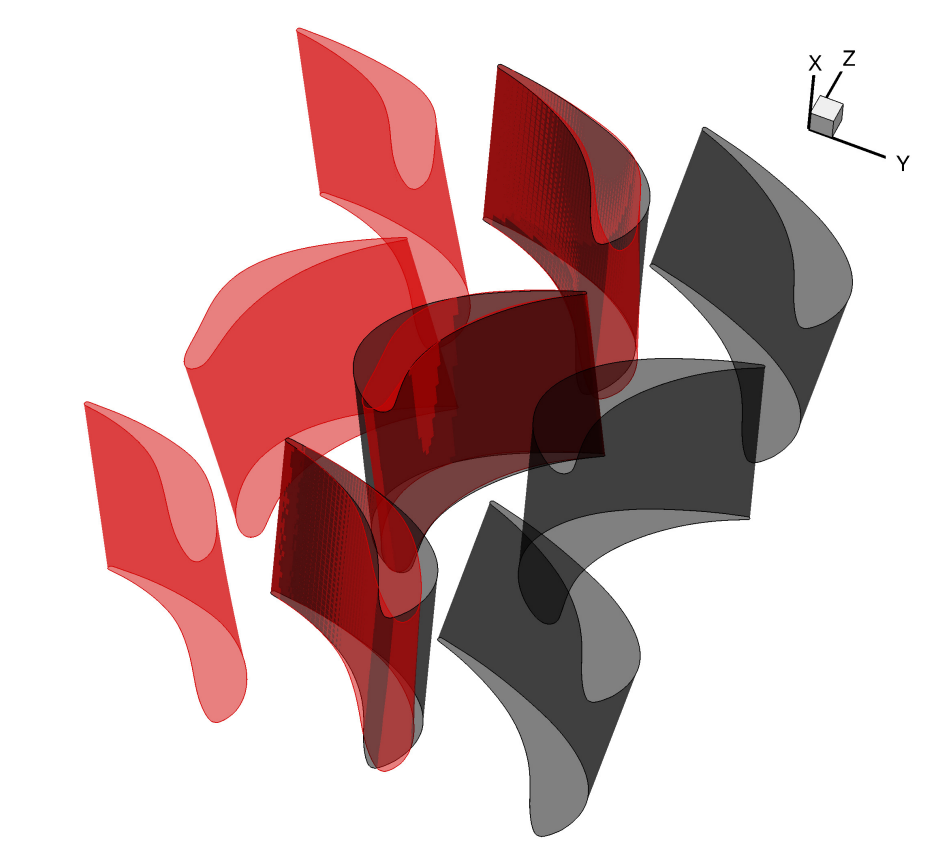As a wide body of works concerning adjoint methods reported in the literature is based on the so-called Constant Eddy Viscosity approximation,[24] it is of practical interest to evaluate when the adoption of such approximation may lead to satisfactory results. To this purpose, the adjoint solutions of the Aachen Turbine and the APU turbine computed with and without the CEV approximation are presented and discussed. The two test cases are simulated in the same conditions as those reported in Section 4.4; the sensitivity of the entropy generation performance parameter (Eq. (4.20)) is computed with respect to the tangential component of the FFD-Box points. Each blade was enclosed within a FFD-Box of degree one in each direction, namely 8 degrees of freedom per blade.

Figure 4.27 shows the comparison between the sensitivities computed with and without the CEV approximation for the Aachen test-case. The use of the CEV approximation leads to considerable accuracy errors for the stator 1 and rotor 1 sensitivities, while the error related to the second stator is lower. This deviations can be directly connected to the flow regime in which the blades operate. As illustrated in Fig. 4.28, the first two blades operate always in highly subsonic conditions (Mach number below 0.5), while larger values of Mach number are calculated for the last blade. The same behavior is observed for the APU turbine. In this case, the CEV approximation has a lower impact on the accuracy of the computed sensitivity (cf. Fig. 4.29) as the entire turbine operates mainly in transonic conditions (cf. Fig. 4.30).

To demonstrate the dependency of the accuracy of the CEV approximation on the flow regime, a 2D cascade is simulated for different expansion ratios (from subsonic to transonic conditions). For each condition, the average error of the computed sensitivity is calculated using the CEV approximation with respect to the case in which the Spalart-Allmaras[51] (SA) and k-ω SST[42] turbulence model are included in the derivation of the adjoint equations. Figure 4.31 shows the Mach contours of the simulated cascade and the estimated error for the use of the CEV approximation at the various pressure ratios. As anticipated, larger errors are encountered at low Mach numbers and the error monotonically decreases with the increasing Mach number. Unsurprisingly, as the SST turbulence model is a more complex model than the SA one, the use of the CEV approximation leads to higher errors for the case in which the turbulence phenomena are described with the SST model as also shown in Fig. 4.31b.

From these findings, it can be inferred that the CEV approximation, adopted for example in recent works,[16,23] can provide accurate results for transonic or supersonic turbomachinery applications, while it is debatable whether it allows to achieve sufficient accuracy in case of cascades operating with low Mach number flows. However, it remains an open question whether the CEV approximation is acceptable in multi-row unsteady optimization in which the wake-rotor interaction plays an important role.

Figure 4.27: Comparison between the sensitivities computed with and without the CEV approximation for the Aachen test-case.

Figure 4.28: Blade to blade Mach contour of the Aachen Turbine.
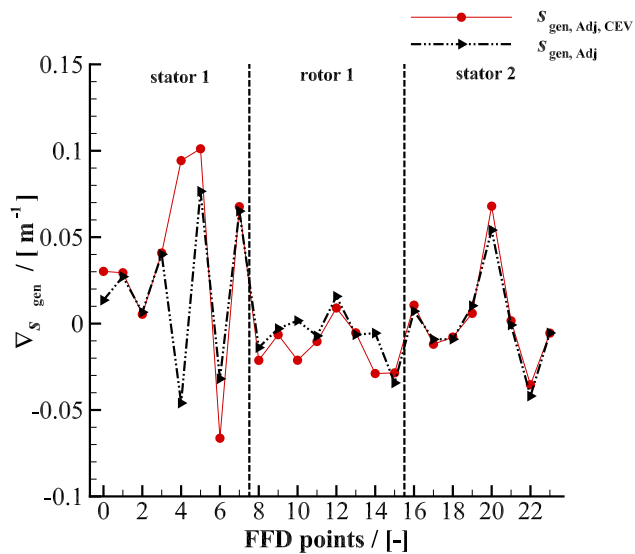
Figure 4.29: Comparison between the sensitivities computed with and without the CEV approximation for the APU test-case.

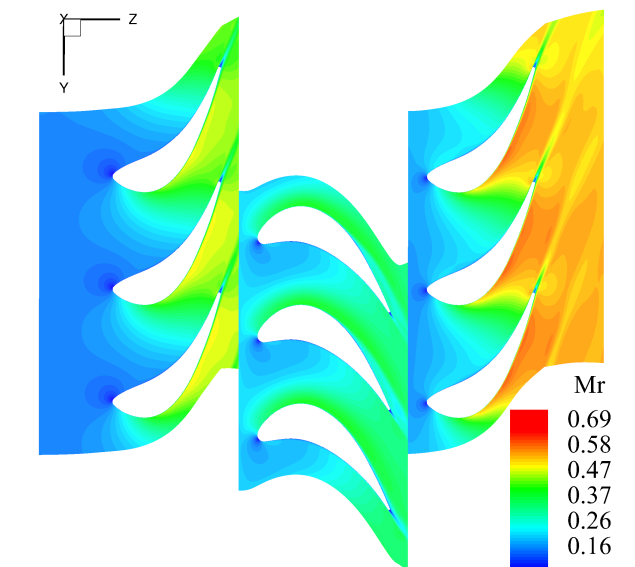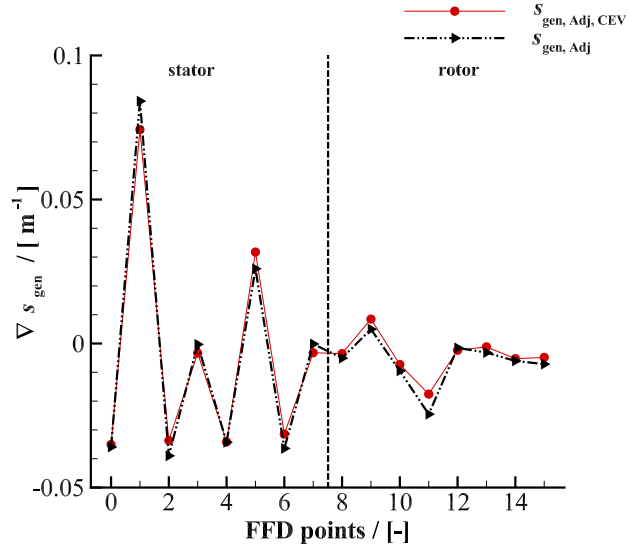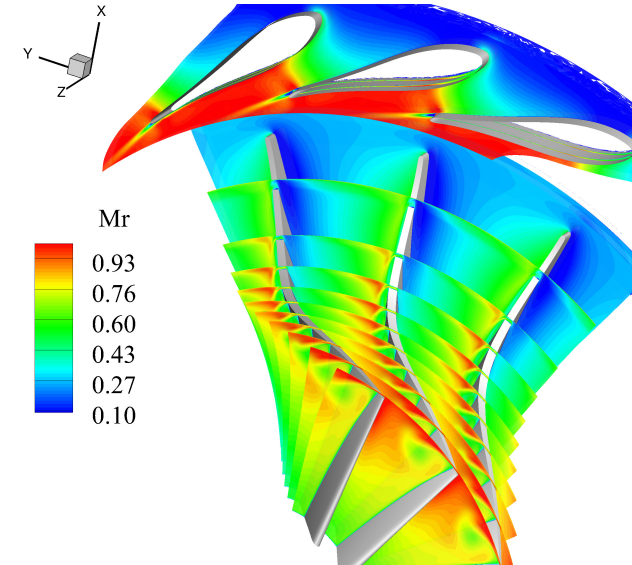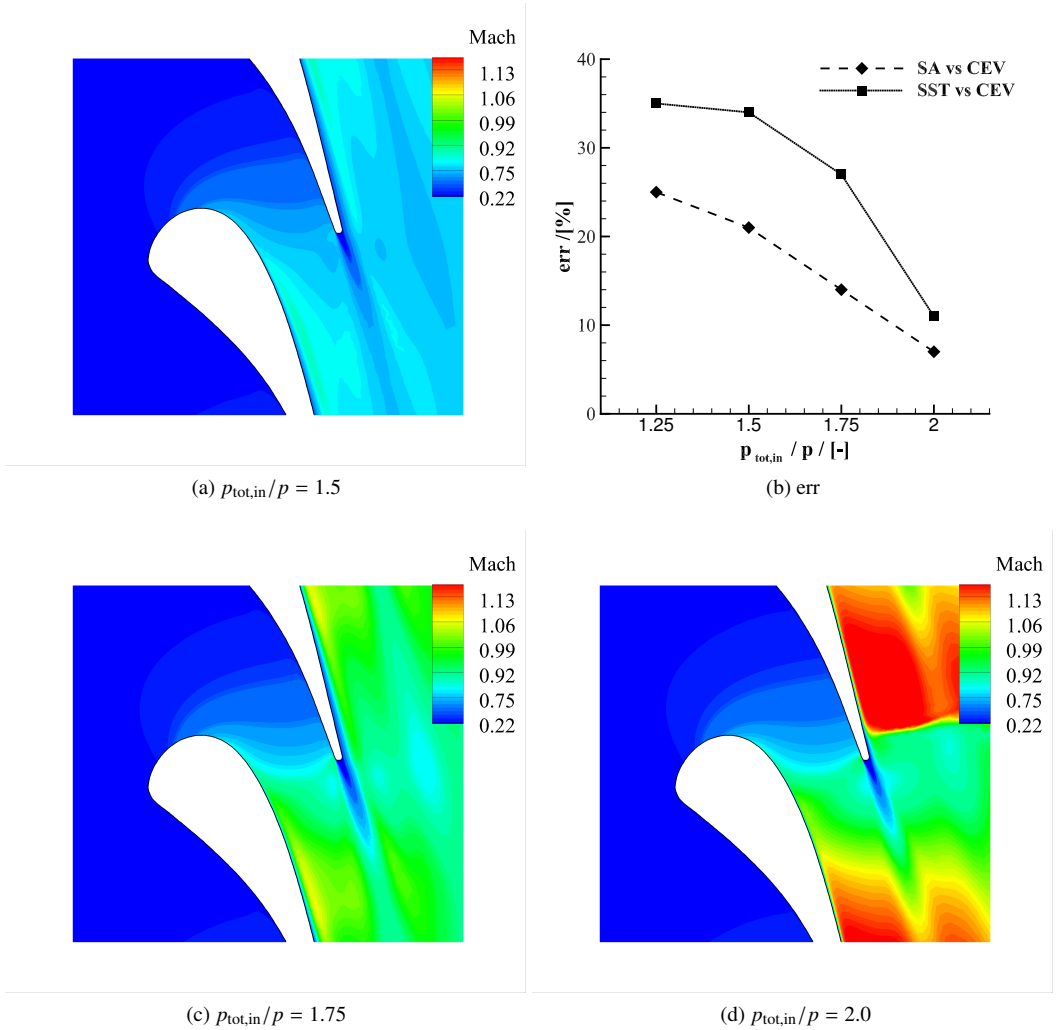Figure 4.30: Mach contour of the APU Turbine.

(a) $p_{tot,in}/p = 1.5$

(b) err

(c) $p_{tot,in}/p = 1.75$

(d) $p_{tot,in}/p = 2.0$

Figure 4.31: Mach number contour at the stator-rotor interface of the Mini ORC Turbine for different rotational speeds.

4.6   Conclusions

This chapter documents the extension and validation of the RANS flow and adjoint solver of the open-source CFD platform SU2 to the simulation and automated fluid dynamic optimization of 3D multi-row tubomachinery. The flow solver was enriched with a conservative and non-reflecting mixing-plane interface, and the discrete adjoint solver was obtained by resorting to automatic differentiation.

The accuracy of the flow solver was assessed by comparison with measurements related to two standard gas turbines and and to a mini-ORC turbine operating with highly supersonic stator in the NICFD regime. The effectiveness of the gradient computation via the discrete adjoint solver was tested by performing the fluid dynamic optimization of a 3D multi-row turbine.

The outcome of this study can be summarized as follows.

- The new data structure of the inflow and outflow boundary nodes enables the access of flow information in a span- and pitch-wise ordered manner facilitating the specification of the a non-reflecting and mixing-plane boundary condition. Furthermore, it allows the simulation of any kind of turbo-machinery configuration by encapsulating all the different coordinate transformations within the boundary nodes.

- The SU2 RANS flow solver was able to accurately simulate the flow of two standard turbine test-cases which are representative of industrial practice. Results showed that the tool is capable of predicting flow quantities with the same level of accuracy of other RANS solver already reported in the literature.

- The SU2 RANS flow solver was also able to accurately simulate the flow of a high-speed ORC turbine operating partly in the NICFD regime. To the authors' knowledge, this is the first contribution to the open-literature in which a CFD solver is validated against measurements performed on a ORC turbine.

- A multiple flow-domains and fully-turbulent discrete adjoint solver was obtained by resorting to an operator-overloading AD tool, called CoDiPack. The validation highlighted that the gradient provided by the discrete adjoint very accurately correlates with the one obtained with finite-differences.

- The capability of the new design tool was demonstrated for the first time by performing a paradigmatic exercise: the fluid dynamic optimization of the 3D Aachen turbine using almost six-hundred design variables. The optimization substantially improved the simulated turbine performance, while satisfying the imposed constraints. This also demonstrates the effectiveness and robustness of adjoint methods for fluid-dynamic design problems in which a large number of design variables are involved.

- The use of the Constant Eddy Viscosity approximation in deriving the adjoint equations may lead to considerable inaccuracy of the computed gradient if the geometry

to optimize operates at low Mach number, while it is satisfactory in case of transonic and supersonic blades.

- Due to the general implementation of the RANS equations for arbitrary thermophysical models, this design framework can also be applied to the design of 3D multi-stage turbomachinery working in the NICFD regime, which was the ultimate goal of this PhD research project.

References

[1] Pierret, S., Coelho, R., and Kato, H., 2007. "Multidisciplinary and multiple operating points shape optimization of three-dimensional compressor blades". *Struct. Multidisc. Optim.,* **33**, pp. 61–70.

[2] Lian, Y., and Liou, M., 2005. "Multi-objective optimization of transonic compressor blade using evolutionary algorithm". *Journal of Propulsion and Power,* **21**(6), pp. 979–987.

[3] Li, Z., and Zheng, X., 2017. "Review of design optimization methods for turbomachinery aerodynamics". *Progress in Aerospace Sciences,* **93**, pp. 1–23.

[4] Jameson, A., 1988. "Aerodynamic design via control theory". *Journal of scientific computing,* **3**(3), pp. 233–260.

[5] Jameson, A., and Reuther, J., 1994. "Control theory based airfoil design using the euler equations". *5th AIAA/USAF/NASA Symposium on Multidisciplinary Analysis and Optimization.*

[6] Jameson, A., 1995. "Optimum aerodynamic design using cfd and control theory". In 12th Computational Fluid Dynamics Conference, p. 1729.

[7] Giles, M. B., and Pierce, N. A., 2000. "An introduction to the adjoint approach to design". *Flow, turbulence and combustion,* **65**(3-4), pp. 393–415.

[8] Kim, S., Alonso, J. J., and Jameson, A., 2004. "Multi-element high-lift configuration design optimization using viscous continuous adjoint method". *Journal of Aircraft,* **41**(5), pp. 1082–1097.

[9] Nadarajah, S. K., and Jameson, A., 2007. "Optimum shape design for unsteady flows with time-accurate continuous and discrete adjoint method". *AIAA journal,* **45**(7), pp. 1478–1491.

[10] Nadarajah, S., and Jameson, A., 2007. "Optimum shape design for unsteady three-dimensional viscous flows using a nonlinear frequency-domain method". *Journal of Aircraft,* **44**(5), pp. 1513–1527.

[11] Papadimitriou, D., and Giannakoglou, K., 2006. "A continuous adjoint method for the minimization of losses in cascade viscous flows". In 44th AIAA Aerospace Sciences Meeting and Exhibit, p. 49.

[12] Papadimitriou, D., and Giannakoglou, K., 2007. "Total pressure loss minimization in turbomachinery cascades using a new continuous adjoint formulation". *Proceedings of the Institution of Mechanical Engineers, Part A: Journal of Power and Energy,* **221**(6), pp. 865–872.

[13] Corral, R., and Gisbert, F., 2008. "Profiled end wall design using an adjoint navier–stokes solver". *Journal of Turbomachinery,* **130**(2), p. 021011.

[14] Luo, J., Xiong, J., Liu, F., and McBean, I., 2011. "Three-dimensional aerodynamic design optimization of a turbine blade by using an adjoint method". *Journal of Turbomachinery,* **133**(1), p. 011026.

[15] Luo, J., Zhou, C., and Liu, F., 2014. "Multipoint design optimization of a transonic compressor blade by using an adjoint method". *Journal of Turbomachinery,* **136**(5), p. 051005.

[16] Mueller, L., and Verstraete, T., 2017. "Cad integrated multipoint adjoint-based optimization of a turbocharger radial turbine". *International Journal of Turbomachinery, Propulsion and Power,* **2**(3), p. 14.

[17] Mousavi, A., and Nadarajah, S., 2010. "Heat transfer optimization of gas turbine blades using an adjoint approach". In 13th AIAA/ISSMO Multidisciplinary Analysis Optimization Conference, p. 9048.

[18] Mousavi, A., and Nadarajah, S., 2011. "Adjoint-based multidisciplinary design optimization of cooled gas turbine blades". In 49th AIAA Aerospace Sciences Meeting including the New Horizons Forum and Aerospace Exposition, p. 1131.

[19] Verstraete, T., Müller, L., and Müller, J.-D., 2017. "Cad-based adjoint optimization of the stresses in a radial turbine". In ASME Turbo Expo 2017: Turbomachinery Technical Conference and Exposition, American Society of Mechanical Engineers, pp. V02CT47A025–V02CT47A025.

[20] Wang, D., and He, L., 2010. "Adjoint aerodynamic design optimization for blades in multistage turbomachinespart i: Methodology and verification". *Journal of Turbomachinery,* **132**(2), p. 021011.

[21] Wang, D., He, L., Li, Y., and Wells, R., 2010. "Adjoint aerodynamic design optimization for blades in multistage turbomachinespart ii: Validation and application". *Journal of Turbomachinery,* **132**(2), p. 021012.

[22] Walther, B., and Nadarajah, S., 2015. "Adjoint-based constrained aerodynamic shape optimization for multistage turbomachines". *Journal of Propulsion and Power,* **31**(5).

[23] Walther, B., and Nadarajah, S., 2015. "Optimum shape design for multirow turbomachinery configurations using a discrete adjoint approach and an efficient radial basis function deformation scheme for complex multiblock grids". *Journal of Turbomachinery,* **137**(8), p. 081006.

[24] Marta, A. C., and Shankaran, S., 2013. "On the handling of turbulence equations in rans adjoint solvers". *Computers & Fluids,* **74**, pp. 102–113.

[25] Economon, D. T., Palacios, F., Copeland, S. R., Lukaczyk, T. W., and Alonso, J. J., 2015. "Su2: An open-source suite for multiphysics simulation and design". *AIAA Journal,* **54**(3), pp. 828–846.

[26] Albring, T. A., Sagebaum, M., and Gauger, N. R., 2016. "Efficient aerodynamic design using the discrete adjoint method in su2". *17th AIAA/ISSMO Multidisciplinary Analysis and Optimization Conference*.

[27] Sagebaum, M., Albring, T., and Gauger, N. R., 2017. Codipack code differentiation package — scientific computing.

[28] Zhou, B., Albring, T., Gauger, N., Economon, N., Palacios, F., and Alonso, J. J., 2015. "A discrete adjoint framework for unsteady aerodynamic and aeroacoustic optimization". *AIAA 2015-3355*.

[29] Zhou, B. Y., Albring, T., Gauger, T., Ilario, T., Economon, T. D., and Alonso, J. J., 2017. "Reduction of airframe noise components using a discrete adjoint approach". *AIAA 2017-3658*.

[30] Sanchez, R., Palacios, R., Economon, T. D., Alonso, J. J., Albring, J. J., and Gauger, J. J., 2017. "Optimal actuation of dielectric membrane wings using high-fidelity fluid-structure modelling". *AIAA 2017-0857*.

[31] Vitale, S., Albring, T. A., Pini, M., Gauger, N. R., and Colonna, P., 2017. "Fully turbulent discrete adjoint solver for non-ideal compressible flow applications". *Journal of the Global Power and Propulsion Society,* **1**, pp. 252 – 270.

[32] Rubino, A., Pini, M., Colonna, P., Albring, T., Nimmagadda, S., Economon, T., and Alonso, J., 2018. "Adjoint-based fluid dynamic design optimization in quasi-periodic unsteady flow problems using a harmonic balance method". *Journal of Computational Physics*.

[33] Saxer, A. P., and Giles, M. B., 1993. "Quasi-three-dimensional nonreflecting boundary conditions for euler equations calculations". *Journal of Propulsion and Power,* **9**(2), pp. 263–271.

[34] Stephan, B., Gallus, H., and Niehuis, R., 2000. "Experimental investigations of tip clearance flow and its influence on secondary flows in a 1-1/2 stage axial turbine". In ASME Turbo Expo 2000: Power for Land, Sea, and Air, American Society of Mechanical Engineers, pp. V001T03A099–V001T03A099.

[35] Jones, A. C., 1996. "Design and test of a small, high pressure ratio radial turbine". *Journal of Turbomachinery,* **118**(2), pp. 362–370.

[36] Denton, J. D., 1993. "Loss mechanisms in turbomachines". In ASME 1993 International Gas Turbine and Aeroengine Congress and Exposition, American Society of Mechanical Engineers, pp. V002T14A001–V002T14A001.

[37] Saxer, A. P., 1992. A numerical analysis of 3-d inviscid stator/rotor interactions using non-reflecting boundary conditions. Tech. rep., Cambridge, Mass.: Gas Turbine Laboratory, Massachusetts Institute of Technology,[1992].

[38] Dwight, R. P., 2009. "Robust mesh deformation using the linear elasticity equations". *Computational Fluid Dynamics 2006*, pp. 401–406.

[39] Sederberg, T. W., and Parry, S. R., 1986. "Free-form deformation of solid geometric models". *ACM SIGGRAPH computer graphics,* **20**(4), pp. 151–160.

[40] Bahamonde, S., Pini, M., De Servi, C., Rubino, A., and Colonna, P., 2017. "Method for the preliminary fluid dynamic design of high-temperature mini-organic rankine cycle turbines". *Journal of Engineering for Gas Turbines and Power,* **139**, pp. 082606–1.

[41] NUMECA International, 2010. *AutoGrid5: Automated Grid Generator for Turbomachinery.* Brussels, Belgium.

[42] Menter, F. R., 1993. "Zonal two equation k-ω turbulence models for aerodynamic flows". *24th AIAA Fluid Dynamics Conference.*

[43] Roe, P. L., 1981. "Approximate riemann solvers, parameter vectors, and difference schemes". *Journal of Computational Physics,* **43**(2), pp. 357–372.

[44] Blazek, J., 2005. *Computational Fluid Dynamics: Principles and Applications.* Elsevier Science.

[45] Yao, J., Jameson, A., Alonso, J. J., and Liu, F., 2001. "Development and validation of a massively parallel flow solver for turbomachinery flows". *Journal of Propulsion and Power,* **17**(3), pp. 659–668.

[46] Sauret, E., 2012. "Open design of high pressure ratio radial-inflow turbine for academic validation". In ASME 2012 International Mechanical Engineering Congress and Exposition, American Society of Mechanical Engineers, pp. 3183–3197.

[47] Verstraete, T., 2010. "Cado: a computer aided design and optimization tool for turbomachinery applications". In 2nd Int. Conf. on Engineering Optimization, Lisbon, Portugal, September, pp. 6–9.

[48] Van Albada, G., Van Leer, B., and Roberts, W., 1997. "A comparative study of computational methods in cosmic gas dynamics". In *Upwind and High-Resolution Schemes*. Springer, pp. 95–103.

[49] Rubechini, F., Marconcini, M., Giovannini, M., Bellucci, J., and Arnone, A., 2015. "Accounting for unsteady interaction in transonic stages". *Journal of Engineering for Gas Turbines and Power,* **137**(5), p. 052602.

[50] Kraft, D., 1988. "A software package for sequential quadratic programming". *Forschungsbericht- Deutsche Forschungs- und Versuchsanstalt fur Luft- und Raumfahrt*.

[51] SPALART, P., and ALLMARAS, S., 1992. *A one-equation turbulence model for aerodynamic flows*. American Institute of Aeronautics and Astronautics.

5

Conclusions and Perspective

The technical and economic viability of energy conversion technologies, such as Organic Rankine Cycle power systems, often depend on the performance of their turbomachinery components, operating partly in the so-called non-ideal compressible fluid dynamic regime. Due to the limited design experience and to the scarce experimental information on NICFD flows, the design of these components greatly benefits from automated fluid dynamic shape optimization techniques. Since the achievement of turbomachinery performance with disruptive designs dictates the use of a large number of design variables, adjoint-based fluid-dynamic shape optimization is the only viable technique. A fully-turbulent adjoint method for the design of multi-stage turbomachinery operating in the NICFD regime was, therefore, developed within this PhD project, and the development is documented in this manuscript.

Based on the results of this work, the following main conclusions can be drawn.

1. The newly developed RANS solver for the simulations of flows in conventional and unconventional turbomachinery was successfully validated by comparison with experimental data related to several relevant and different test cases. Results showed that the tool is capable of predicting flow quantities with the same level of accuracy of state-of-art RANS solvers.

2. Despite the additional complexity due to the need of incorporating accurate fluid thermodynamic models, it was possible to devise an exact fully-turbulent adjoint solver applicable to shape-optimization design problems in which the flow expands/compresses in the NICFD regime.

3. The capability of the new tool was demonstrated by optimizing the blade shapes of two typical 2D ORC turbine cascades, in which the non-ideal fluid properties are calculated with an appropriate fluid model. In both cases, the optimization performed with the RANS flow and adjoint solver substantially improved the performance calculated from the simulated test cases, while satisfying the imposed constraints. The optimization process was also repeated assuming inviscid flows. The results emphasize the importance of incorporating the viscous gradient contributions, especially for the design of transonic ORC cascades.

4. The potential of the non-ideal compressible RANS adjoint solver was also shown by comparison with a more conventional ideal gas adjoint method, using the same test cases. The results demonstrate that the simplified approach provides physically inaccurate gradient information leading to sub-optimal cascade configurations, if NICFD effects are moderate. In case of strong NICFD effects, the fluid dynamic performance of the optimal solution, obtained with the ideal gas based adjoint method, can be even worse than that calculated for the starting geometry.

5. The capability of the new design tool was also demonstrated by optimizing a 3D multi-stage turbine using almost six-hundred design variables. The optimization substantially improved the simulated turbine performance, while satisfying the imposed constraints. This also shows the effectiveness and robustness of adjoint meth-

ods for fluid-dynamic design problems in which a great number of design variables are involved.

6. The use of the Constant Eddy Viscosity approximation in deriving the adjoint equations may lead to considerable accuracy error of the computed gradient if the geometry to optimize operates at low Mach number, while it is satisfactory for transonic and supersonic blades.

7. The use of advanced automatic differentiation techniques based upon the operator-overloading method allow to derive an efficient, robust, and accurate turbomachinery adjoint solver which requires, on average, only 30% more run-time than the direct flow solver.

8. The participation in the SU2 open-source project facilitated the development of the turbomachinery design framework documented in this PhD thesis, and it will guarantee its maintainability, extendibility and usability in future research and industrial projects.

9. With the contribution documented in this PhD thesis, SU2 becomes the first ever open-source CFD suite capable of handling multi-stage turbomachinery shape-optimization via adjoint methods. All the newly developed tools can be freely downloaded and used by anybody who is interested in turbomachinery fluid-dynamic design from the GitHub repository: github.com/su2code.

To increase the level of confidence in the RANS turbomachinery solver, a more extensive validation campaign with both standard and NICFD turbomachinery test-cases should be performed. Given the lack of documentation related to detailed turbomachinery fluid-dynamic experiments in the open-literature (especially for NICFD applications), it is envisaged that conventional and ORC turbomachinery manufacturers might be attracted by the newly developed capabilities of SU2 and might join the SU2 project providing additional validation test-cases.

To improve computational efficiency, the design framework should be enriched with a CAD-based parameterization method. Differently from the FFD approach, the CAD-base method allows to specify geometrical constraints by directly bounding the design variables. This results in optimization problems in which less adjoint solutions must be computed.

Last but not least, the method documented in this PhD thesis should be extended to multi-disciplinary design problems. Only by concurrently taken into account fluid-dynamic, structural, thermal and costs aspects, designers can succeed in contributing to rapid market introduction of cost-effective turbomachinery for the more efficient and less polluting power systems and aero-engine of the future.

List of publications

Journal papers

Vitale, S., Pini, M.,and Colonna, P., 2018. "SU2: the Open-Source CFD code for turbo-machinery analysis and design". *J. Turbomach.*, Ready for submission.

Vitale, S., Albring, T., Pini, M., Gauger, N.R., and Colona, P., 2017. "Fully turbulent discrete adjoint solver for non-ideal compressible flow applications". *J. Glob. Power Propuls. Soc.*, **1** pp. 252-270.

Pini M., Vitale, S., Colonna, P., Gori, G., Guardone, A., Economon, T., Alonso, J.J., and Palacios, F., 2017. "Su2: the open-source software for non-ideal compressible flows". *Journal of Physics.*, **821**(1) pp. 012013.

Rubino, A. ,Vitale, S., Pini, M., and Colonna, P., 2018 "Fully-turbulent adjoint method for the unsteady shape optimization of multi-stage turbomachinery". *J. Turbomach.*, Ready for submission.

Anand, N. ,Vitale, S., Pini, M., Otero-Rodrguez, G.J., and Pecnik, R., 2018 "Design methodology for supersonic radial vanes operating in non-ideal flow conditions". *J. Glob. Power Propuls. Soc.*, Accepted for publication.

Pini, M., Azzini, L., Vitale, S., and Colonna, P., 2018. "A two-phase discrete adjoint method applied to the shape optimization of steam turbine cascades". J. Turbomach., Submitted.

Rubino, A., Pini, M., Kosec, M., Vitale, S., and Colonna, P., 2018 "A look-up table method based on unstructured grids and its application to non-ideal compressible fluid dynamic simulations". *J. Comp. Sci.*, **28** pp. 70-77

Casati, E., Vitale, S., Pini, M., Persico, G. and Colonna, P., 2014. "Centrifugal turbines for mini-organic Rankine cycle power systems". *J. Eng. Gas Turb. Power*, **136**(12), pp. 122607.

Conference proceedings

Vitale, S., Gori, G., Pini, M., Guardone, A., Economon, T., Palacios, F., Alonso, J.J., and Colonna, P. 2015. "Extension of the su2 open source cfd code to the simulation of turbu-

lent flows of fuids modelled with complex thermophysical laws". *Proceedings of the 22nd AIAA Computational Fluid Dynamics Conference.*, Dallas - USA.

Vitale, S., Pini, M., Ghidoni, A., and Colonna, P., 2015. "Fluid dynamic design and analysis of a highly loaded Centrifugal rotor for mini orc power systems". *Proceedings of the 3rd International Seminar on ORC Power Systems – ASME ORC-2015*, Bruxelles - Belgium.

Anand, N., Vitale, S., Pini, M., and Colonna, P., 2018 "Assessment of fully-turbulent steady and unsteady adjoint sensitivities for stator-rotor interaction in turbomachinery". *Proceedings of the Global Power and Propulsion Forum*, Montreal - Canada.

Rubino, A., Vitale, S., Pini, M., and Colonna, P., 2018 "Assessment of fully-turbulent steady and unsteady adjoint sensitivities for stator-rotor interaction in turbomachinery". *Proceedings of the Global Power and Propulsion Forum*, Montreal - Canada.

Keep, J.A., Vitale, S., Pini, M., and Burigana, M., 2017. "Preliminary verification of the open-source CFD solver SU2 for radial-inflow turbine applications". *Proceedings of the 4th International Seminar on ORC Power Systems*, Milan - Italy.

Pini, M., De Servi, C., Burigana, M., Bahamonde, S., Rubino, A., Vitale, S., and Colonna, P., 2017. "Fluid-dynamic design and characterization of a mini-ORC turbine for laboratory experiments". *Proceedings of the 4th International Seminar on ORC Power Systems*, Milan - Italy.

Gori, G., Guardone, A. , Vitale, S., Head, A., Pini, M., and Colonna, P., 2015. "Non-ideal compressible-fluid dynamics simulation with su2: Numerical assessment of nozzle and blade flows for organic rankine cycle applications". *Proceedings of the 3rd International Seminar on ORC Power Systems – ASME ORC-2015*, Bruxelles - Belgium.

Conference presentations

Vitale, S., Albring, T., Gauger, N.R., Colonna, P., and Pini, M., 2016. "Adjoint-based optimization framework for non-ideal compressible fluid flows applied to Organic Rankine Cycle turbines". *ECCOMAS 2016*, Crete Island - Greece.

About the author

Salvatore Vitale was born in Patti, Italy, on March, 2nd 1988. In 2007, he received his high school diploma from the Liceo Scientifico Enrico Fermi of Sant'Agata di Militello (Sicily). After that, he decided to enroll for the Bachelor in Energy Engineering at Politecnico di Milano. In 2010, he obtained his BSc, and he decided to continue his studies at Politecnico enrolling for the Master in Energy Engineering with majoring in power-generation. In April 2013, he received his MSc degree cum laude after carrying out his final thesis project at the Delft University of Technology under the supervision of Prof. Piero Colonna. During the years of the master, he discovered his passion for the field of turbomachinery and computational fluid-dynamics so he decided to pursuit a PhD degree in these topics. In November 2013, he was successfully appointed as PhD student at the Aerospace faculty of the Delft University of Technology, where, under the main supervision of Dr. Matteo Pini and Prof. Piero Colonna, he investigated and developed advanced computational fluid-dynamic methods for the design of NICFD turbomachinery. In February 2018, Salvatore joined Shell where he has been working since then as scientific software engineer in the team of Dr. Sander Belien.